1981

Simulation of lava flow with small scale models

Seung O. Park
Iowa State University

Park, Seung O.

SIMULATION OF LAVA FLOW WITH SMALL SCALE MODELS

Iowa State University PH.D. 1981

PLEASE NOTE:

In all cases this material has been filmed in the best possible way from the available copy. Problems encountered with this document have been identified here with a check mark ✓.

1. Glossy photographs or pages _____
2. Colored illustrations, paper or print _____
3. Photographs with dark background ✓
4. Illustrations are poor copy _____
5. Pages with black marks, not original copy _____
6. Print shows through as there is text on both sides of page _____
7. Indistinct, broken or small print on several pages ✓
8. Print exceeds margin requirements _____
9. Tightly bound copy with print lost in spine _____
10. Computer printout pages with indistinct print _____
11. Page(s) _____ lacking when material received, and not available from school or author.
12. Page(s) _____ seem to be missing in numbering only as text follows.
13. Two pages numbered _____. Text follows.
14. Curling and wrinkled pages _____
15. Other _____

Simulation of lava flow with small scale models

by

Seung O. Park

A Dissertation Submitted to the
Graduate Faculty in Partial Fulfillment of the
Requirements for the Degree of

DOCTOR OF PHILOSOPHY

Major: Aerospace Engineering

Approved:

Signature was redacted for privacy.

In Charge of Major Work

Signature was redacted for privacy.

For the Major Department

Signature was redacted for privacy.

For the Graduate College

Iowa State University
Ames, Iowa

1981

TABLE OF CONTENTS

I. INTRODUCTION

The abundance and complexity of flow phenomena observed in nature are, in a word, overwhelming. Among such natural flow phenomena are lava flows associated with volcanism.

Lava may be loosely defined as magma (molten rock) which pours out on the surface of the earth or rock solidified from such magma. This molten rock has almost every fluid dynamic attribute - sometimes it flows as a Newtonian fluid, and sometimes as non-Newtonian. The lava cools as it flows, some of it solidifying, thereby developing a solid skin or slabs of solidified magma floating along the surface. If the solidified magma becomes welded to the sides of a channel, then a lava tunnel or tube develops which results in a fully or partially filled "pipe flow" situation.

The cooling process involves all modes of heat transfer, that is, conduction, radiation, and convection.

As the lava cools, crystals start to form and grow. In terms of the analysis of lava flow, this poses rather delicate rheological problems.

Lava is generally classified by its chemical composition. The three principal types, differentiated by their proportions of silica, are acid, intermediate, and basic lavas. The acid lavas, such as rhyolite, have 70% or more of silica; intermediate lavas, 50 to 70% (andesites, dacites); and basic lavas less than 50% (basalts) (1). In general, the higher the silica content, the more viscous the lava.

On the basis of surface texture, lava flows may be divided into four groups; they are pahoehoe, aa, block, and pillow lava.

Pahoehoe flows are the most liquid type of lava with little froth,

Volcanicity and Forms of Extrusive Bodies

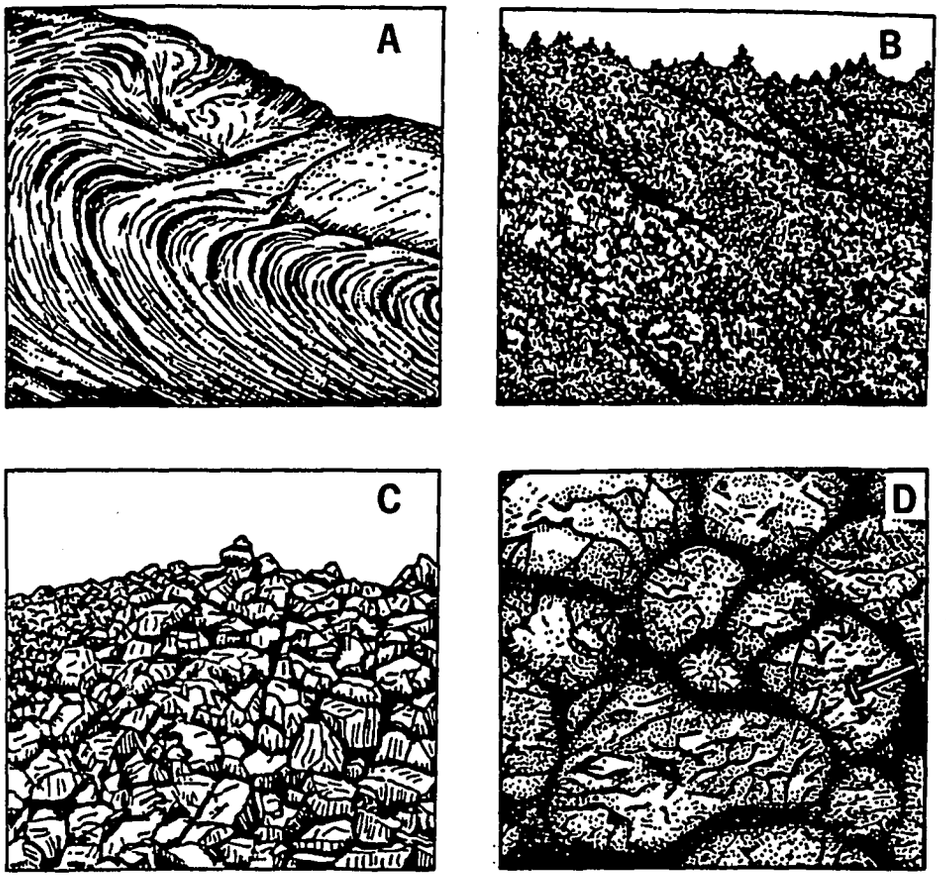

A. Pahoehoe Lava

B. Aa Lava

C. Block Lava

D. Pillow Lava

Fig. 1.1 Types of lava flows (Ref. 2:7)

They develop a smooth, billowing, ropy or entrail-like crust. Surface characteristics of this type are usually seen in flows of basaltic composition.

Aa lava is blocky, spiny and slow moving. The crusts of aa flows are jumbles of rough, clinkery and spiny fragments, ranging from small chips to blocks measuring meters on a side, under which lies the massive core of pasty lava.

Pillow lavas are the most abundant volcanic rocks on earth. Most pillow lavas are basalts that erupted under water or ice. Pillows form when hot, fluid lava comes into contact with water or fine-grained, water soaked sediments. The lava chills rapidly to form a glassy but plastic skin around still liquid lava and rolls along in the manner of plastic bags full of liquid. The round or sausage-shaped bags are known as "pillows", and are usually heaped one on another. They have rounded tops, but their bases fit into the shape of the underlying surface.

Block lava flows are made up largely of detached, polyhedral blocks with plane or slightly curved faces and conspicuous dihedral angles. Acid lavas usually exhibit this type of surface.

The above mentioned four flow types are sketched in Fig. 1.1.

More detailed and rigorous descriptions and characteristics of these flow types are found in Williams and McBirney (3) and Ollier (4).

As has been briefly mentioned earlier, the lava flow process is so complex and diversified, that unless it is dramatically simplified, only two avenues are available for studying the flow phenomena: experimental and numerical simulation procedures. Even in these cases, the amount of work is so tremendous that many simplifying assumptions have to be brought

in to make the work tractable.

This study is mainly focused on experimental simulation. The simulation approach attempted here is far from being complete, rather it is a suggestion of a more complete method or approach that can be used to tackle this problem.

In chapter II, some important properties of lava are summarized as well as typical flow dimensions.

In chapter III, some analytical solutions to the simple cases are reviewed and developed and attempts are made to get an insight to the flow mechanism, and thereby to develop a shortcut to the simulation.

In chapter IV, principles of dimensional analysis and modeling are reviewed, and the dimensionless π terms necessary to establish similarity for this specific problem are discussed. Also, new π - terms are derived from the analytical solutions discussed in chapter III.

In chapter V, experimental procedures and results are discussed to confirm the ideas developed in chapters III and IV.

II. SOME RHEOLOGICAL PROPERTIES AND FLOW FEATURES OF LAVA

In this chapter, more detailed fluid and flow properties and features of lava flows will be examined to help develop the general idea of lava flow rheology.

A. Rheological Properties

1. Viscosity

The viscosity of the lavas of basaltic volcanoes is of the order of 10^3 to 10^5 poise at the time of eruption and that of acidic lava exceeds 10^6 poise. The lavas which form domes or spines must be more viscous than 10^{10} poise at the time of extrusion (5). (See Table 2.1)

The viscosity of silicate melts varies with temperature, approximately following the Arrhenius relation, that is

$$\mu = \mu_0 \exp (W/RT)$$

where W and R are constants, μ is viscosity and T is temperature.

However, once crystallization starts, the increase in viscosity is very rapid, and hence the above equation is no longer valid. Some laboratory measurements of viscosity of different lavas are shown in Fig. 2.1.

2. Yield strength

From in situ rheological measurements of a lava lake in Hawaii, Shaw et al. (6) showed that lava behaves approximately as a Bingham plastic material, which opened a new facet of the study of lava flow.

The constitutive equation for Bingham plastic material is, in the simplest case,

$$\begin{aligned} \tau &= \tau_y + \mu\dot{\gamma} & \tau &\geq \tau_y \\ \mu &= \infty & \tau &< \tau_y \end{aligned} \qquad \ldots (2.1)$$

Table 2.1 Viscosity of lavas, with simultaneous temperature measurements, and the observed maximum temperature (Tm) (Ref. 5:987)

Volcano	Year	Viscosity (poise)	Temperature (°C)	Tm (°C)	Author
Kilauea	1912	-	-	1185	Day and Shepherd
	1952	$2\text{-}4 \times 10^4$	1100 - 1050	1155	McDonald
Mauna Loa	1919	4×10^4	1200 - 1150	-	Nichols
	1950	4×10^3	1070	1120	McDonald
Paricutin	-	$10^5 - 10^6$	1070	-	Krauskopf
	1944	-	-	1200	Zies
Nyamuragira	1938	-	-	1145 - 1160	Verhoogen
O-shima	1937	5×10^4	1060	1060	Nagata
	1950	2×10^5	1050	1050	Murauchi
	1951	6×10^3	1125	1125	Minakami
		2×10^4	1108	1125	Minakami
		7×10^4	1083	1125	Minakami
		2×10^5	1038	1125	Minakami
Vesuvius	1904	-	-	1100	Brun
	1913	-	-	1200	Perret
	1944	9×10^4	-	-	Imbò
Stromboli	1901	-	-	1150	Brun
Etna	1951	-	-	1110 - 1120	Tazieff
Miyakejima	1940	7×10^5	1000	965	Hagiwara and Nagata
Asama	1936	-	-	1050	Minakami
Sakurajima	1946	$3\text{-}6 \times 10^6$	1000	-	Hagiwara
		$10^9 \times 10^{10}$	900	-	Nagata
Usu	1947	-	-	980	Nakamura

where $\dot{\gamma}$ denotes rate of strain, τ is shear stress, τ_y is yield strength which is a material property.

Thus, a Bingham plastic material behaves as a liquid (or fluid) when the applied shear stress is greater than the yield strength, otherwise it behaves as a solid. (See Fig. 2.2)

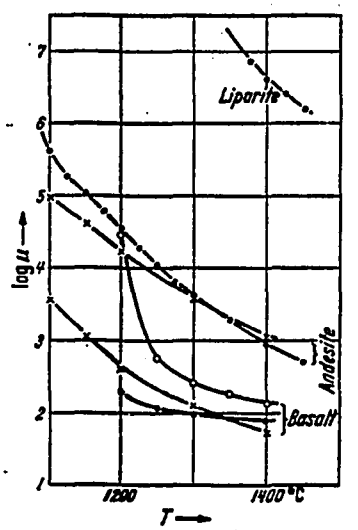

Fig. 2.1 Viscosity of dry melts from volcanic rocks (Ref. 5:987)

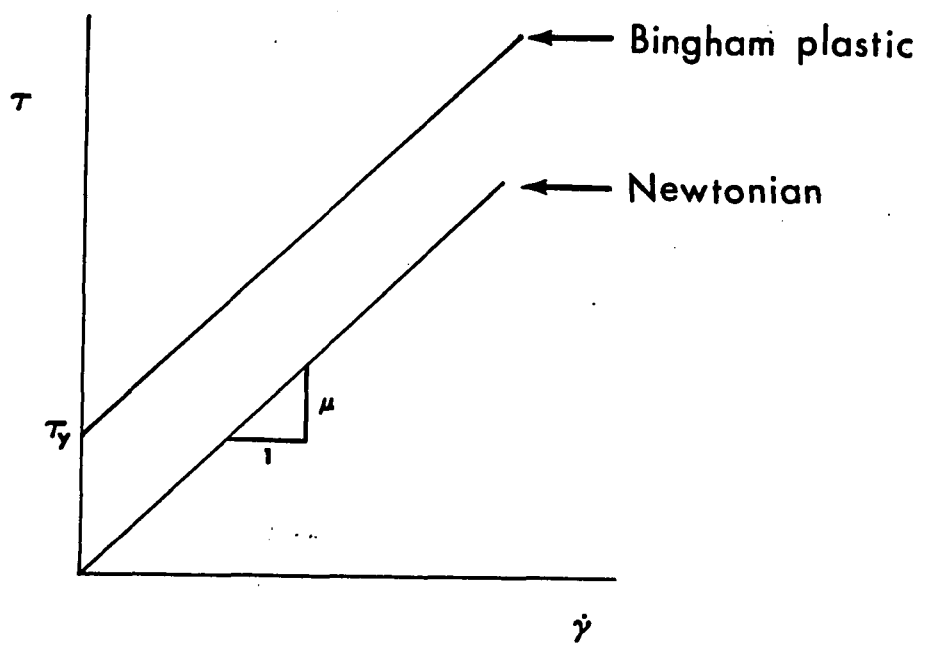

Fig. 2.2 Stress-strain rate relationship for Bingham plastic and Newtonian fluid

Yield strengths of basalt and andesite are strongly dependent on temperature as are the viscosities, and increase with cooling as shown in Fig. 2.3.

Note that the yield strength of igneous rocks ranges from $.2 \sim 7.0 \times 10^4$ dyne/cm^2.

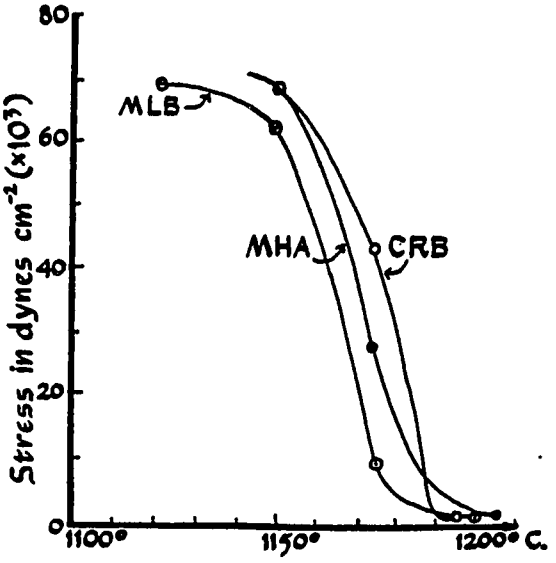

MLB; Basalt from Makaopuhi lava lake, Kilauea

CRB; Columbia River Basalt

MHA; Andesite from Mount Hood, Oregon

Fig. 2.3 Yield strengths of basalt and andesite in their melting ranges (Ref. 3:24)

3. Temperature

The temperature of lavas from measurements varies according to the type of rock and phase of activity, but in general it ranges from 900°C to 1200°C. (See Table 2.1) Basaltic lavas erupt in the temperature range 1,200 to 1,100°C, andesite lavas extrude between 1000 and 1,100°C, and dacitic or rhyolitic lavas come to the surface at temperatures below 1000°C (5). Table 2.2 shows the compiled data of extrusion temperatures of various lava types.

Table 2.2 Estimates of extrusion temperature for various lava types (Ref. 3:28)

Kilauea, Hawaii	Tholeiitic basalt	1,150-1,225°C
Paricutin, Mexico	Basaltic andesite	1,020-1,110°C
Nyiragongo, Congo	Nephelinite	980°C
Nyamuragira, Congo	Leucite basalt	1,095°C
Taupo, New Zealand	Pyroxene rhyolite: pumice flows	860 - 890°C
	Amphibole rhyolites: lavas, ignimbrites, pumice flows	735 - 780°C
Mono Craters, California	Rhyolite lavas	790 - 820°C
Iceland	Rhyodacite obsidians	900 - 925°C
New Britain, Southwest Pacific	Dacite Lava, pumice	925°C
	Rhyodacite pumice	880°C

4. Surface tension

Surface tension plays an important role in determining the shape and the motions of liquids that have open surfaces. It is partly responsible for the various forms of pyroclastic ejecta, such as ribbon bombs, Pele's tears and Pele's hair. Measurements of surface tension for various lavas

are shown in Fig. 2.4. For comparison, surface tension of mercury is 480 dynes/cm, and that of water is 73 dynes/cm.

For a discussion of the boundary conditions associated with a free surface including surface tension, see Wehausen and Laitone (7).

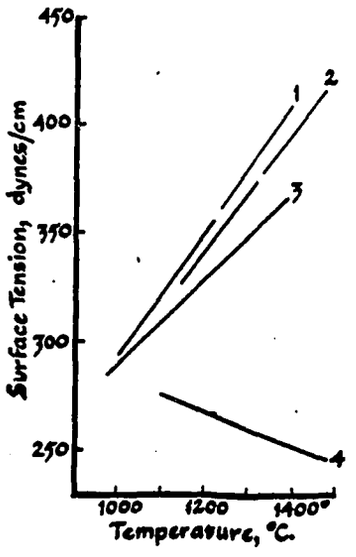

1. Columbia River basalt
2. Mount Hood andesite
3. Rhyolite from Newberry Volcano
4. Pure silica glass

Fig. 2.4 Surface tension of igneous rocks in their melting range (Ref. 3:82)

5. Density, thermal properties

Other important variables not listed so far include specific heat, thermal conductivity, density, and heat of fusion. A typical value of specific heat at constant pressure, Cp, is approximately 0.2 ∿ 0.3 cal/gm°C, and that of heat of fusion, Q_F is 65 ∿ 100 cal/gm at atmospheric pressure (3).

Temperature variation of thermal conductivity and density are shown in Fig. 2.5 and 2.6 respectively.

Thermal conductivity of basalt is about the same as that of concrete made out of sand and gravel aggregate.

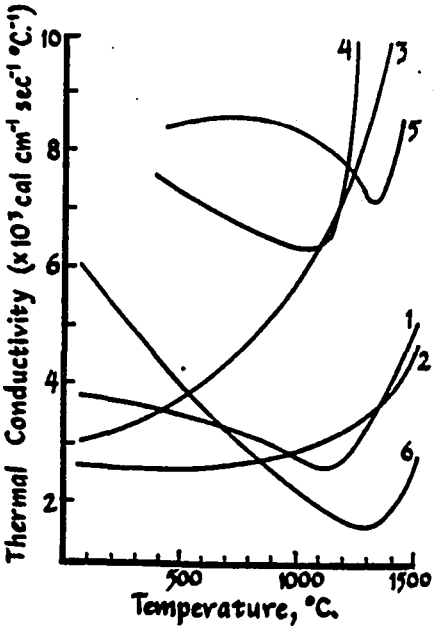

1. Basalt; 2. Andesite; 3. Rhyolite; 4. Dunite; 5. Peridotite; 6. Lunar basalt

Fig. 2.5 Thermal conductivity of various igneous rocks (Ref. 3:29)

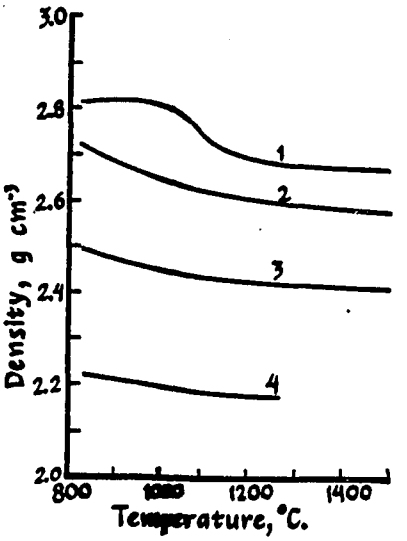

1. Alkali basalt
2. Tholeiitic basalt
3. Andesite
4. Rhyolite

Fig. 2.6 Densities of igneous rocks in the molten state (Ref. 3:29)

B. Flow Features

1. Extrusion rate and volume

Extrusion rate is one of the most important flow characteristics which is directly related to velocity, depth, etc.

It has been found that the rate of extrusion significantly contributes to the length of lava flows (8).

Extrusion rate largely depends on the fluidity of magma and on the size and dimensions of the eruptive conduits. In almost all eruptions, the rates are highest during initial stages of activity.

In Table 2.3, volume flow rates of various eruptions are listed. (Ref. 3:101)

Table 2.3 Extrusion rates of different volcanoes

Extrusion Rate (m^3 / sec)	Period	
1,000 100	1st day 2nd day	Hekla, 1947
1,390	1st 17 hrs	Mauna Loa, 1887 (Pulsatory extrusion)
2. ∿ 6.	Oct. 1945 ∿ Mar. 1946	Paricutin, Mexico

Extrusion rates are also partly responsible for the form of lava domes. For example, the andesitic and dacitic lavas that extrude to form steep-sided domes of Peléan type issue very slowly.

The volumes of most historic lava flows are on the order of a few cubic kilometers. Generally, basaltic flows are larger in volume than andesite. Siliceous lavas are generally much less voluminous. Lengths of lava flows also depend strongly on volume, although under a given set of conditions, we expect a certain critical length to exist (mainly due to cooling). We would expect longer flows from larger volumes. Correlation of length and volume for Hawaiian flows has been found by Malin (9).

2. Large scale flow profiles and dimensions

Lavas flow naturally to lower levels. Flow itself is generally unsteady (strictly speaking), due to the variations of eruption rate, cooling processes, topography, etc.

To illustrate the general development of flow geometry, it will be instructive to consider one specific flow history.

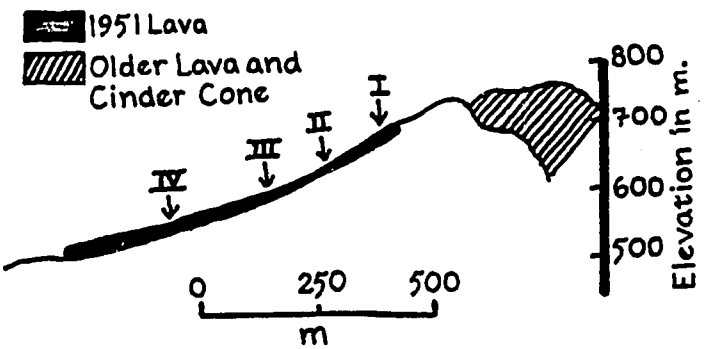

Fig. 2.7 Positions at which data in Table 2.4 were collected (Ref. 10)

Table 2.4 Measurements of the March, 1951, lava of Mihira Volcano, O-shima, Japan

Position	Thickness cm	Width cm	Slope	Maximum velocity cm sec^{-1}	Temperature	Viscosity poises
I	31	110	35°	102 ± 8	1125°	5.6×10^3
II	50	160	27°	35 ± 3	1108°	1.8×10^4
III	77	210	16°	15 ± 3	1083°	7.1×10^4
IV	130	250	11°	8 ± 2	1038°	2.3×10^5

Minakami (10) recorded the temperatures, velocities, dimensions and viscosities at four positions along the course of a lava flow of the 1950-1951 eruptions of Mihira volcano on the island of O-shima, Japan. Locations of measurements and measured data are in Fig. 2.7 and Table 2.4 respectively.

When the lava reached lower and gentler slopes, it thickened and widened, and its velocity decreased sharply. These changes were accompanied by a drop in temperature.

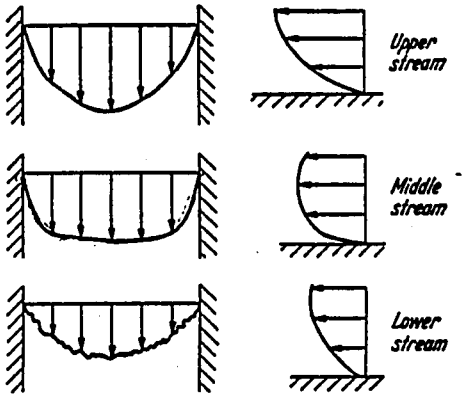

Fig. 2.8 Distribution of the flow velocity within a lava stream in the 1951 eruption of O-shima in Japan (Ref. 5:986)

In Fig. 2.8, velocity profiles at different locations of a lava stream are sketched.

In the upper stream where the temperature is very high, the lava behaves as Newtonian fluid, developing a parabolic flow profile. In the middle stream, the lava becomes thicker and attains a yield strength, mainly due to cooling which causes crystallization (or solidification). As a result, the so called plug-flow profile develops. Further downstream, cooling effects are much more severe, resulting in a profile like that shown in the sketch, which may be associated with a fairly thick skin.

Geometric dimensions of lava vary widely depending upon various flow properties, extrusion rates and types, topography, etc. Generally basaltic flows are widespread and long, whereas most siliceous lavas are short and

thick.

Table 2.5a and b show the thicknesses and lengths of some flows (edited from Ref. 3).

Table 2.5a Thickness of various lava flows

Volcanic Activity	Thickness	Avg. Thickness	
Columbia River Basalt	10 ∿ 65 m	25 m	Fissure Eruption
Iceland (Tertiary)			
-Alkali Olivin Basalts		7 m	Fissure Eruption
-Tholeiitic Basalts		11 m	Fissure Eruption
-Icelandites		13 m	Fissure Eruption
-Siliceous		30 m	Fissure Eruption
Hawaii	few centimeters ∿ 15 m		Flank Flows

Table 2.5b Lengths of various lava flows

Volcanic Activity	Lengths	
Laki, Iceland	> 88 km	
Mauna Loa, 1859	50 km	Entered the sea
Mauna Loa	25 km, avg.	Averaged since 1843
Kilauea	< 11 km	

3. Cooling and lava tube

As has been mentioned frequently, cooling plays a large role in lava flow morphology.

Even though all three types of heat transfer mechanism (conduction, convection, radiation) are present in the cooling process, it has been shown that the most important of these is radiation (11). For example, at a surface temperature of 1373°K and an air temperature of 300°K, the ratio of radiative heat loss to convective heat loss (at the surface) is 9.5. In addition, the radiative heat transfer slightly dominates the conductive heat loss at the bottom surface (11).

Dramatic evidence of the cooling process is found in the formation of lava tubes. Lava tubes are best developed in basaltic pahoehoe flows, and are rare in more siliceous flows. They are especially rare in aa lavas (3).

One mechanism of lava tube formation is sketched in Fig. 2.9 a and b. As a pahoehoe flow moves downstream, a crust develops and is carried downstream by the underlying stream as discrete, closely spaced plates. Further downstream, these plates jam together and fuse to the sides of the channel, forming a stable roof. If the supply of fresh lava is subsequently cut off at the source, lava drains away to leave an empty tube.

The dimensions of lava tubes range from a few centimeters to 30 meters or more in diameter, and from a few meters to several kilometers in length (3). A lava tube located in Surtesy, Iceland is shown in Fig. 2.10.

The crusts and roofs of tubes act as heat shields, preventing heat loss by radiation, allowing the lava to flow greater distances.

Fig. 2.11 shows a collapsed lava tube in Idaho.

More detailed discussion, such as different types of lava tube forma-

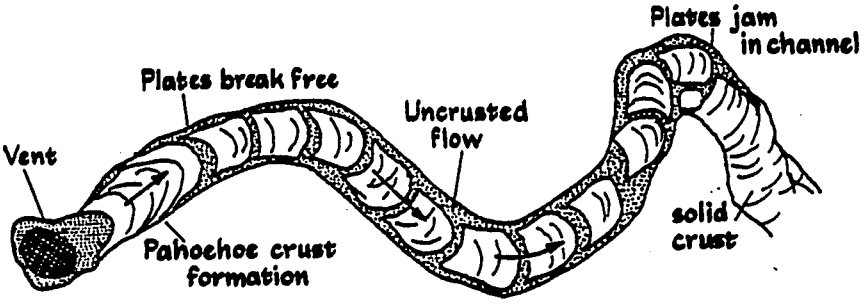

a

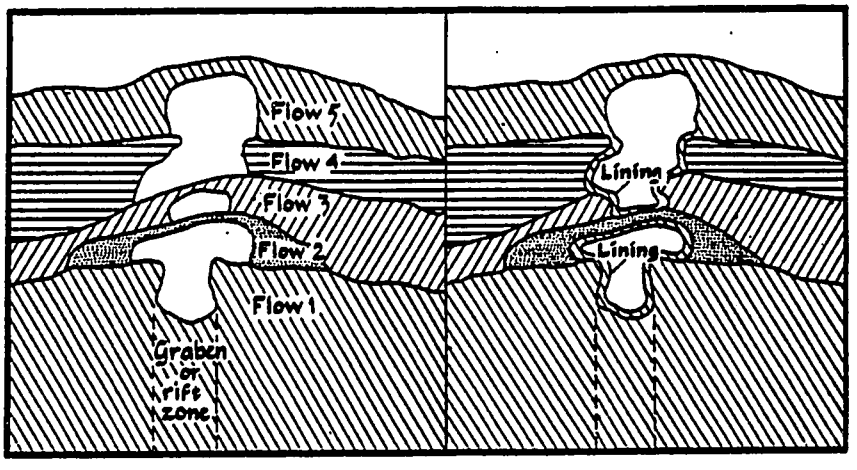

b

Fig. 2.9a Stages in the formation of a lava tube

Fig. 2.9b Hypothetical diagram illustrating possible formation and modification of lava structures as a result of subsequent lava flows (Ref. 12: 217, 219)

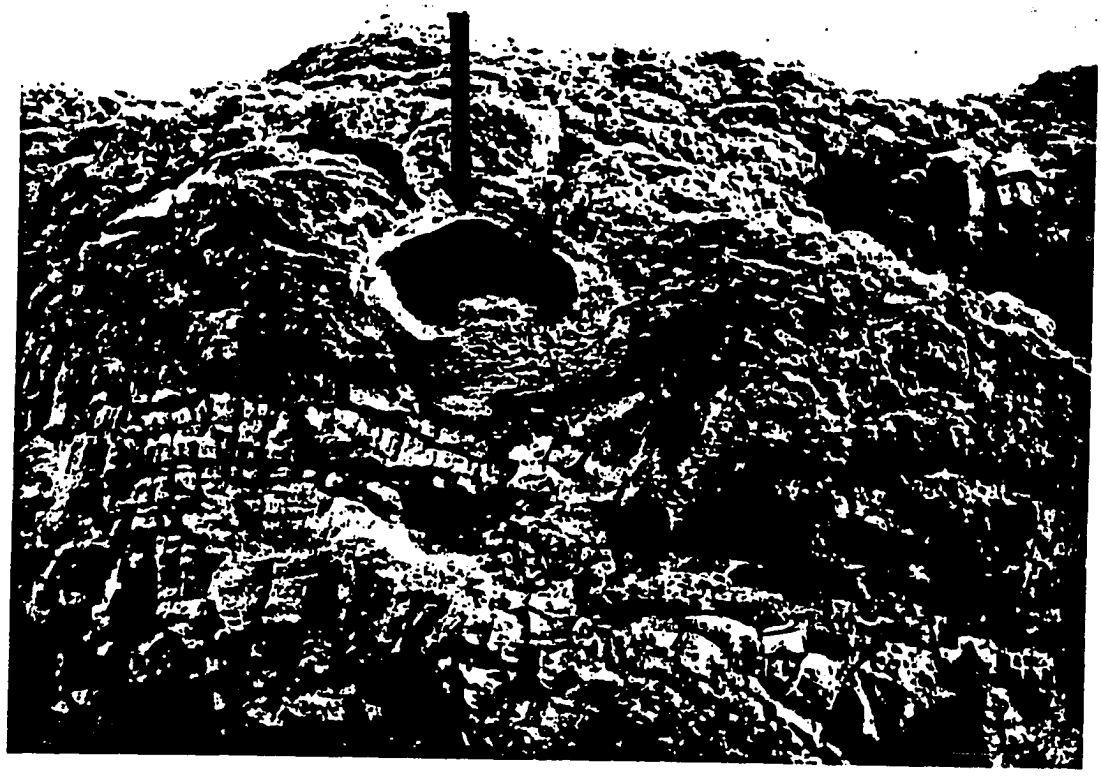

Fig. 2.10 Truncated lava flow, south side of Surtsey, Iceland, showing a lava tube (marked by arrow) (Ref. 2: plate 115A)

Fig. 2.11 Collapsed lava tube near Butte Crater, Idaho. The channel extends for over 5 kilometers. Over most of its length, the channel is from 5 to 10 meters deep and 20-30 meters wide. (Ref. 2: plate 117B)

tion and mechanism can be found in Greeley (12) and Peterson and Swanson (13).

Another notable feature associated with cooling is the development of ropy structures on the surface of pahoehoe basalt flows. These features have been explained to be folds which form owing to the compression of a fluid whose viscosity decreases with depth, which in turn is a consequence of cooling (14).

Besides the structures discussed above, there exist many additional interesting features, such as stalactites, lava tree molds, lava coils, blisters, etc. Discussions of these features can be found in Ref. 3 and Ref. 15.

Figure 2.12 summarizes the possible textural variation associated with eruption from a single basaltic vent.

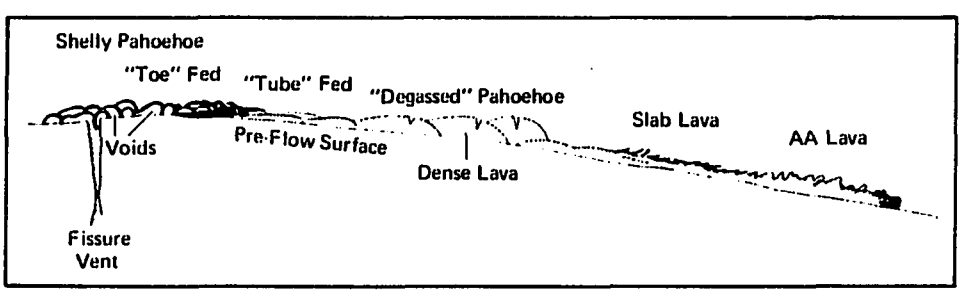

Fig. 2.12 Diagram showing some types of basaltic lava flows related to an eruptive vent (Ref. 16:130)

III. SOME SIMPLE ANALYTIC SOLUTIONS

In this chapter, mathematical formulations and solutions are discussed that are pertinent to the study of lava flow.

A. Governing Equations

The following important governing equations can be written for a continuum in tensor notation (17).

conservation of mass:

$$\partial_o \rho + \partial_j (\rho v_j) = 0 \tag{3.1}$$

conservation of momentum:

$$\rho (\partial_o v_k + v_j \partial_j v_k) = \rho F_k + \partial_j \tau_{jk} \tag{3.2}$$

conservation of energy:

$$\rho (\partial_o e + v_j \partial_j e) = \tau_{jk} V_{jk} - \partial_j q_j \tag{3.3}$$

where

v_i = velocity vector

F_k = body force per unit mass

τ_{jk} = stress tensor

V_{jk} = rate of deformation tensor, $\frac{1}{2} (\partial_j v_k + \partial_k v_j)$

q_j = heat flux vector

e = internal energy

ρ = density

and subscript o denotes time.

The set of three equations written above comes from the basic conservation principles of mechanics, namely, mass, momentum, and energy conservation. Though the set of governing equations appears to be simple, its in-

herent non-linearity, not to mention non-linear boundary conditions, is well known to fluid mechanicians.

The relation between stress tensor τ_{jk} and rate of deformation tensor V_{jk} forms so called "constitutive equations", that of a Newtonian fluid (probably the simplest) being

$$\tau_{ij} = -p\,\delta_{ij} + \lambda V_{kk}\,\delta_{ij} + 2\mu V_{ij} \tag{3.4}$$

When the relation Eq.(3.4) is substituted to the momentum equation Eq.(3.2), the well known "Navier-Stokes" equation is obtained, discussions of which can be found in most standard fluid mechanics books (for example, Batchelor (18)).

The constitutive equation for the Bingham material (visco-plastic) is (19),

$$2\mu V_{ij} = \begin{cases} 0 & , F < 0 \\ F\tau'_{ij} & , F \geq 0 \end{cases} \tag{3.5}$$

with

$$F = 1 - \frac{\tau_y}{\sqrt{J_2}} \tag{3.6}$$

where τ'_{ij} = stress deviator tensor defined by $\tau'_{ij} = \tau_{ij} - 1/3\,\tau_{\alpha\alpha}\,\delta_{ij}$

τ_y = yield stress

J_2 = second invariant of the stress deviator, i.e.,

$$1/6[(\tau_{11}-\tau_{22})^2 + (\tau_{22}-\tau_{33})^2 + (\tau_{33}-\tau_{11})^2\ ] + \tau_{12}^2 + \tau_{23}^2 + \tau_{31}^2$$

The function F written as Eq. (3.6) is called a yield function.

When the yield function F is negative, the material behaves in a rigid manner; positive values of the yield function imply finite rates of deformation. The state of stress for which F = 0 forms the yield limit at which viscoplastic flow sets in or ceases, depending on the direction from which the yield limit is crossed.

The second equation of Eq.(3.5) can be solved with respect to the stress deviator to give (17),

$$\tau'_{ij} = \left(2\mu + \frac{\tau_y}{\sqrt{v_{(2)}}}\right) V_{ij} \tag{3.7}$$

where $v_{(2)}$ is the second invariant of the strain tensor defined by

$$v_{(2)} = \tfrac{1}{2}\left(V_{ij}V_{ji} - V_{ii}V_{jj}\right)$$

For the simplest case (one velocity component in simple shear), Eq. (3.7) reduces to

$$\tau_{xy} = \tau_y + \mu \frac{du}{dy} \text{ , when } \tau_{xy} > \tau_y$$

which has been given as Eq.(2.1).

Since it is so difficult a task to solve the set of equations (3.1), (3.2) and (3.3) with the constitutive equation (3.5) and with suitable boundary conditions for any fairly general case, only simple problems will be considered where analytical solutions are readily available. These solutions will hopefully lead us to some physical insights relevant to simulation problems.

B. Simple Solutions

1. Flow down an inclined plane

First we will consider the fully developed, steady, two dimensional (of infinite width), constant density and temperature flow flowing down an inclined plane which makes an angle θ with the horizontal. See Fig. 3.1 for a coordinate system.

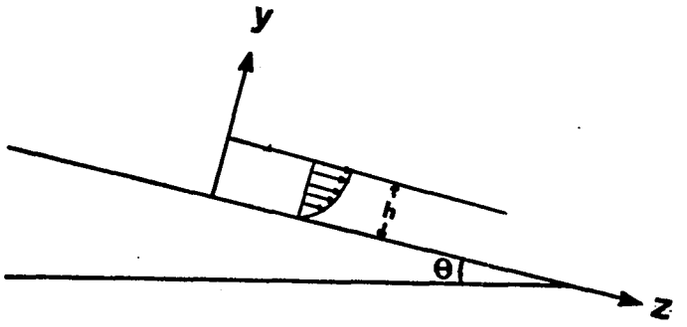

Fig. 3.1 Coordinate system for 2-d flow down an inclined plane

a. Newtonian fluid case In this case, the equation of motion is simply

$$0 = \frac{d\tau}{dy} + \rho g \sin\theta \tag{3.8}$$

Note that the continuity equation requires $u_x = 0$ if we assume $v = 0$. Therefore, $u = u(y)$.

Without considering surface tension, the boundary conditions to be satisfied are

$$\left.\begin{aligned} \tau &= 0 , \quad y = h \\ u &= 0, \quad y = 0 \end{aligned}\right\} \tag{3.9}$$

Using the constitutive equation

$$\tau = \mu \frac{du}{dy} ,$$

Eq.(3.7) can be easily integrated with Eq.(3.9) to give,

$$u(y) = \frac{\rho g \sin\theta}{\mu} (hy - \tfrac{1}{2} y^2) \tag{3.10}$$

Hence the velocity profile is parabolic.

Volume flow rate per unit width, Q/W, is calculated as,

$$Q/W = \int_o^h u dy = \frac{\rho g \sin\theta h^3}{3\mu} \tag{3.11}$$

or

$$\frac{Q\mu}{\rho g \sin\theta w h^3} = 1/3 \tag{3.12}$$

Average velocity U_{av} is defined as,

$$U_{av} = \frac{1}{h} \int_o^h u dy = \frac{Q}{wh} = \frac{\rho g \sin\theta h^2}{3\mu} \tag{3.13}$$

Noting that,

$$u_{(h)} = \frac{\rho g \sin\theta h^2}{2\mu} ,$$

$$U_{av} = \frac{2}{3} U(h)$$

From Eq.(3.13)

$$\mu = \frac{\rho g \sin\theta h^2}{3U_{av}} \tag{3.14}$$

Eq.(3.14) has been used frequently for estimating the viscosity of flowing lava. (For example, see Refs. 3, 5.)

From Eq. (3.10), it is seen that the depth of the flow is determined by Q/W, μ, $\rho g \sin\theta$, via

$$h = \left(\frac{3\mu (Q/W)}{\rho g \sin\theta} \right) 1/3 \tag{3.15}$$

If the rate of extrusion is changed suddenly by a small amount $\delta(Q/W)$, the transition region from one thickness to another advances down the plane (see Fig. 3.2) at a speed V which is given by (18),

$$V\,\delta h = \delta(Q/W)$$

that is,

$$V = \frac{d(Q/W)}{dh} = \left(\frac{9(Q/W)^2 \rho\, g \sin\theta}{\mu}\right)^{1/3} \tag{3.16}$$

Thus, the speed of transition region would be very small if the fluid is very viscous (high viscosity).

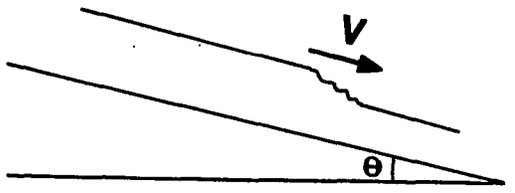

Fig. 3.2 Illustration of the speed of the transition region

b. Bingham plastic case Eq.(3.8), with the condition of no shear at y = h, is integrated to give,

$$\tau = \rho\, g \sin\theta\ (h-y) \tag{3.17}$$

The constitutive equations for Bingham plastic are

$$u = \text{constant (or } \mu = \infty), \qquad \tau \leq \tau_y \tag{3.18a}$$

$$\tau - \tau_y = \mu \frac{du}{dy} \qquad \tau > \tau_y \tag{3.18b}$$

Let h_s be defined as

$$\rho g \sin\theta \, (h - h_s) = \tau_y \tag{3.19}$$

or

$$h_s = h - \frac{\tau_y}{\rho g \sin\theta}$$

Thus,

$$y \leq h_s \Leftrightarrow \tau \geq \tau_y$$

$$y > h_s \Leftrightarrow \tau < \tau_y$$

Eq.(3.19) and Eq.(3.17) are substituted into Eq.(3.18b) to give

$$\rho g \sin\theta \, (h_s - y) = \mu \frac{du}{dy}$$

This is readily integrated using a no slip condition at y = 0 to give the velocity profile:

$$\left.\begin{aligned} u &= \frac{\rho g \sin\theta}{\mu} \left(h_s y - \frac{y^2}{2}\right), \quad y \leq h_s \\ u &= \frac{\rho g \sin\theta \, h_s^2}{2\mu} = \text{constant}, \quad h_s \leq y \leq h \end{aligned}\right\} \tag{3.20}$$

The velocity profiles for a Newtonian fluid and a Bingham plastic are shown schematically in Fig. 3.3.

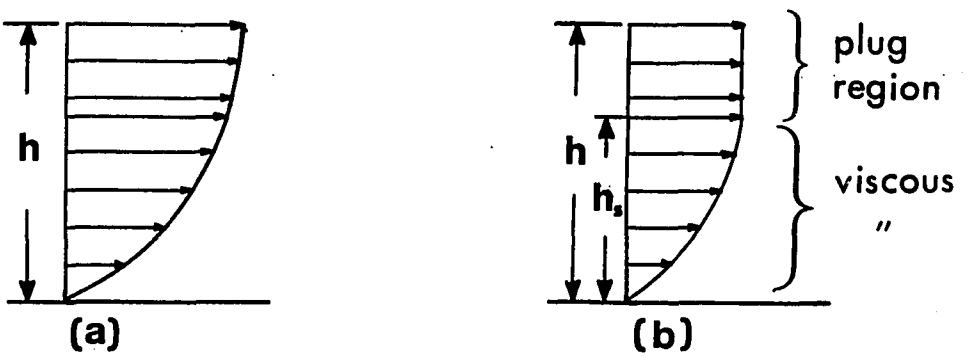

Fig. 3.3 Velocity profiles of Newtonian fluid (a) and Bingham plastic (b)

From the velocity profile of Eq.(3.20), we get

$$\frac{Q/W \cdot \mu}{\rho g \sin\theta h^3} = 1/3 \left(1 - \frac{3}{2} \frac{\tau_y}{\rho g \sin\theta h} + \frac{1}{2} \left(\frac{\tau_y}{\rho g \sin\theta h} \right)^3 \right)$$

Since the wall shear stress, τ_w, is

$$\tau_w = \rho g \sin\theta h \tag{3.21}$$

the above equation can be written as

$$\frac{Q/W \cdot \mu}{\rho g \sin\theta h^3} = \frac{1}{3} \left[1 - \frac{3}{2} \left(\frac{\tau_y}{\tau_w} \right) + \frac{1}{2} \left(\frac{\tau_y}{\tau_w} \right) \right] \tag{3.22a}$$

or

$$\frac{Q/W \cdot \mu}{\rho g \sin\theta \cdot h^3} = \frac{1}{3} \left[1 - \frac{3}{2} \left(\frac{h_f}{h} \right) + \frac{1}{2} \left(\frac{h_f}{h} \right)^3 \right] \tag{3.22b}$$

by defining h_f as

$$h_f = h - h_s = \frac{\tau_y}{\rho g \sin\theta}$$

Both of these expressions can be found easily in standard textbooks of Rheology.

Note that if $\tau_y = 0$, Eq.(3.22a) reduces to the equation for the Newtonian fluid, and if $\tau_y = \tau_w$, $Q = 0$, i.e. no flow occurs.

2. Channel flow down an inclined plane

The two dimensional equations discussed in the previous section (Eq. (3.10), (3.22)) are commonly used in interpreting the morphology of lava flows (Refs. (3), (20), (21)). However, it is first necessary to check the validity of those equations in terms of aspect ratio (ratio of width to

depth of the flow. Aspect ratio will be denoted as λ throughout the text.)

This is done by studying the isothermal rectilinear flow in a rectangular channel with velocity components (o, o, u).

The coordinate system is given in Fig. 3.4.

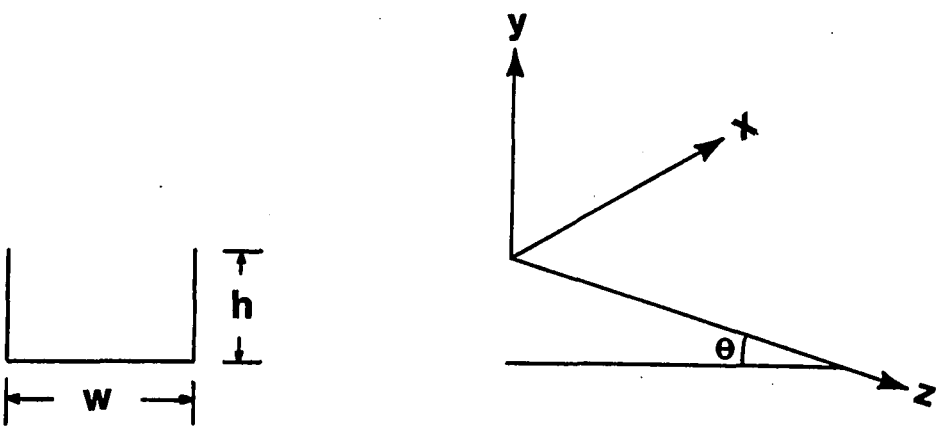

Fig. 3.4 Coordinate system for rectangular channel flow

a. Newtonian case Consider a fully developed flow of a Newtonian fluid. Since only the z-component of velocity is non-zero, continuity equation requires that $u_z = 0$, thus $u = u(x,y)$.

The momentum equation can then be written as

$$\mu (u_{xx} + u_{yy}) = -\rho g \sin\theta \qquad (3.23)$$

i.e., the gravity force is balanced by the viscous force. The velocity field, in this case, can be readily determined by using the technique of separation of variables for the Poisson equation (3.23) with homogeneous boundary conditions. The analytical solution is available for flow in a

rectangular duct of half width, a, and half height, b (22).

In this case

$$Q' = \frac{ab^3}{4\mu} (\rho g \sin\theta) f\left(\frac{a}{b}\right)$$

where

$$f\left(\frac{a}{b}\right) = \frac{16}{3} - \frac{1024}{\pi^3} \frac{b}{a} \sum_{n=0}^{\infty} \frac{\tanh\left(\frac{(2n+1)\pi a}{2b}\right)}{(2n+1)^5}$$

The above expressions can be written in our case as

$$\frac{Q\mu}{\rho g \sin\theta h^3 W} = \frac{1}{16} f\left(\frac{W}{h}\right) \tag{3.24}$$

where

$$f\left(\frac{W}{h}\right) = \frac{16}{3} - \frac{2048}{\pi^3} \frac{h}{W} \sum_{n=0}^{\infty} \frac{\tanh\left(\frac{(2n+1)\pi W}{4h}\right)}{(2n+1)^5} \tag{3.25}$$

For the case when $W \geq 6h$, Eq.(3.24) can be approximated as (22),

$$\frac{Q\mu}{\rho g \sin\theta h^3 W} = \frac{1}{3} \left(1 - 0.418 \frac{h}{W}\right) \tag{3.26}$$

Results of Eq.(3.24) are plotted in Fig. 3:5, for various aspect ratios. As can be seen from the figure, the effect of side wall diminishes as aspect ratio increases, and becomes negligible for aspect ratios greater than 10. As h/W (1/λ) tends to zero, the value $\frac{Q\mu}{\rho g \sin\theta h^3 W}$ tends to 1/3 which is the two-dimensional flow value (Eq.(3.12)).

b. Bingham plastic case In this case, solution procedure for the flow field is more difficult than for Newtonian fluids.

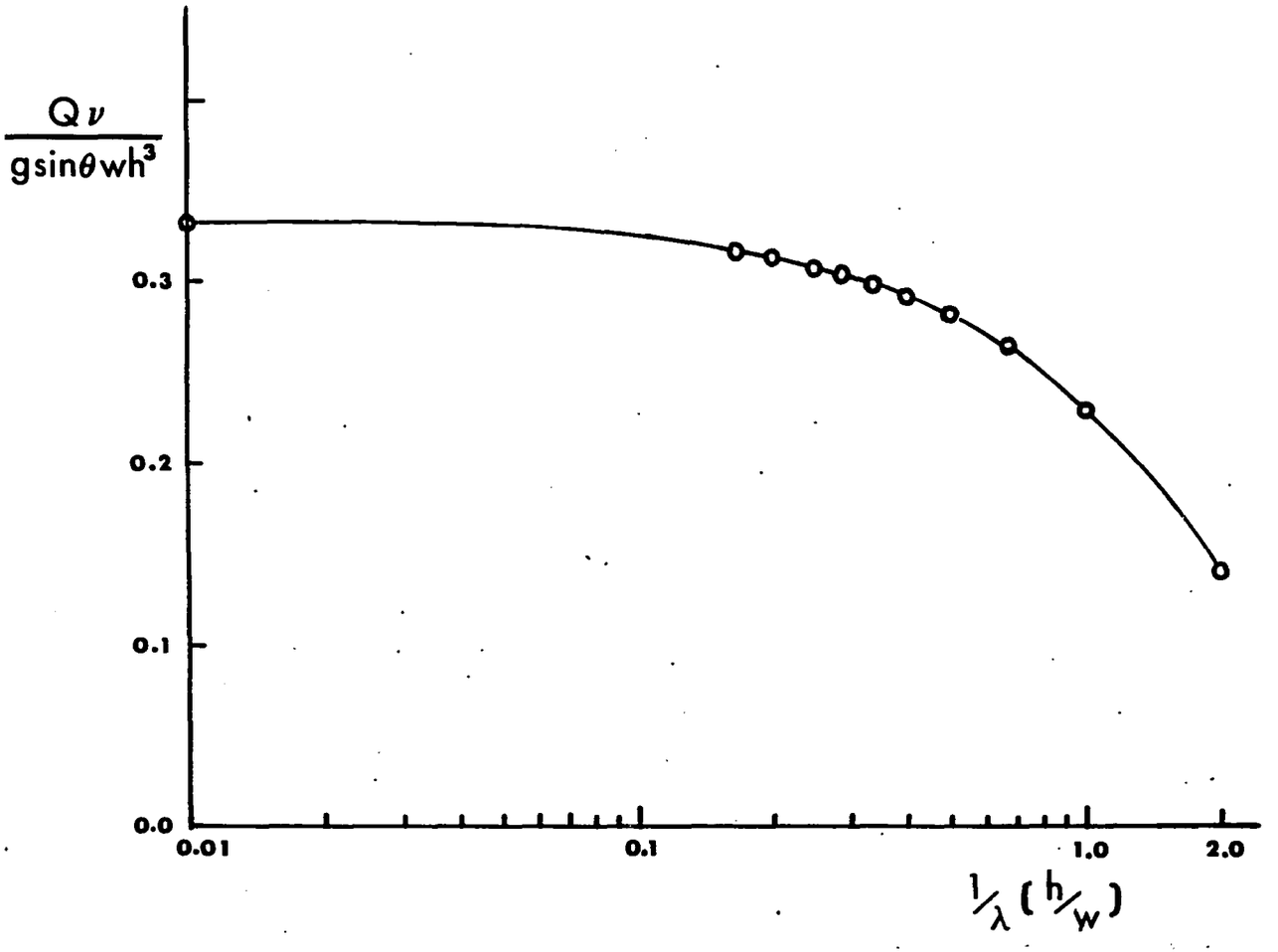

Fig. 3.5 $\frac{Q\mu}{\rho g \sin\theta h^3 W}$ vs. h/W for channel flow of Newtonian fluid

The equation for the velocity field is no longer linear and also the yield surface is not known, a priori. (Unsteady flow problems of this nature are often referred to as Stefan problems (23), which arise in melting or solidification where moving boundary of separation between the two phases exists.)

First, we consider an approximate solution suggested by Kozicki and Tiu (24). Starting from the Rabinowitsch-Mooney equation (25,26), the following approximate equation for the bulk velocity is developed, with no slip condition:

$$\frac{2U}{r_H} = \frac{\tau_o}{\mu}\left[\frac{1}{a+b} - \frac{1}{b}\left(\frac{\tau_y}{\tau_o}\right) + \frac{a}{b(a+b)}\left(\frac{\tau_y}{\tau_o}\right)^{\frac{b}{a}+1}\right] \tag{3.27}$$

where r_H = cross-sectional area/perimeter

$$\tau_o = \frac{1}{p}\int_p \tau \, ds, \quad p = \text{perimeter}.$$

R_H and τ_o are called hydraulic radius and average wall shear stress, respectively.

The coefficients a and b in Eq.(3.27) are geometric coefficients determined with reference to the analytic solution for Newtonian fluid (see Eq. (3.24)), and vary with aspect ratio $\lambda = W/h$.

The values of a and b are tabulated in Table 3.1.

Table 3.1 Geometric coefficients for rectangular open channel (Ref. 24:131)

$\lambda = W/h$	a	b
2.0	0.2123	0.6759
4.0	0.2439	0.7276
6.0	0.2867	0.7817
8.0	0.3212	0.8182
10.0	0.3472	0.8446
12.0	0.3673	0.8639
14.0	0.3828	0.8767
16.0	0.3951	0.8911
18.0	0.4050	0.9010
20.0	0.4132	0.9097
100.0	0.4806	0.9795
∞	0.5000	1.0000

Note that when $\frac{\tau_y}{\tau_o} = 1$, $u = 0$.

Physically this means that the average wall shear (τ_o) just balances the yield strength (τ_y) which must be surpassed for flow to occur; thus, no flow occurs when $\tau_y = \tau_o$.

Now consider the case when $\lambda \to \infty$. Then $\tau_o \to \tau_W = \rho g \sin\theta h$, $r_H \to h$. Hence, Eq.(3.27) reduces to

$$U = \frac{\rho g \sin\theta h^2}{3\mu}\left[1 - \frac{3}{2}\left(\frac{\tau_y}{\tau_W}\right) + \frac{1}{2}\left(\frac{\tau_y}{\tau_W}\right)\right]$$

which is the same as Eq.(3.22a).

Clearly, Eq.(3.27) can be put into the form

$$\frac{Q\mu}{\rho g \sin\theta\, h^3 W} = f\left(\frac{\tau_y}{\tau_W},\ \lambda\right) \tag{3.28}$$

τ_W in the above equation is the 2-dimensional wall shear stress, that is $\tau_W = \rho g \sin\theta\, h$. Of course a more natural choice of wall shear stress would be τ_o as in the original paper. However, for the purpose of comparison with 2-dimensional equation (Eq.3.22a), τ_W will be used throughout the discussion.

For a rectangular channel, hydraulic radius r_H is given as,

$$r_H = \frac{\lambda}{\lambda+2}\, h \tag{3.29}$$

And τ_o can be written in terms of τ_W as follows.

$$\tau_o = \frac{1}{p}\int_p \tau\, ds = \frac{1}{p}\left\{(\text{Area}) \cdot \rho g \sin\theta\right\} = r_H \rho g \sin\theta$$

Therefore, upon substitution of Eq.(3.29) into the above equation,

$$\tau_o = \frac{\lambda}{\lambda+2}\,\tau_W \tag{3.30}$$

Hence, Eq.(3.28) can be calculated easily with the aid of Table 3.1. The results are plotted in Fig. 3.6. Again we see that the value $\frac{Q\mu}{\rho g \sin\theta\, h^3 W}$ tends to that of 2-dimensional case as λ increases. But, different from the Newtonian case, the ratio of 2-dimensional value to 3-dimensional value increases as $\frac{\tau_y}{\tau_W}$.

A more rigorous approach to this problem has been achieved by Johnson and Hampton (27).

The momentum equation, in the velocity formulation, can be written as

$$0 = \rho g \sin\theta + \nabla \cdot (\mu_a \nabla u) \tag{3.31a}$$

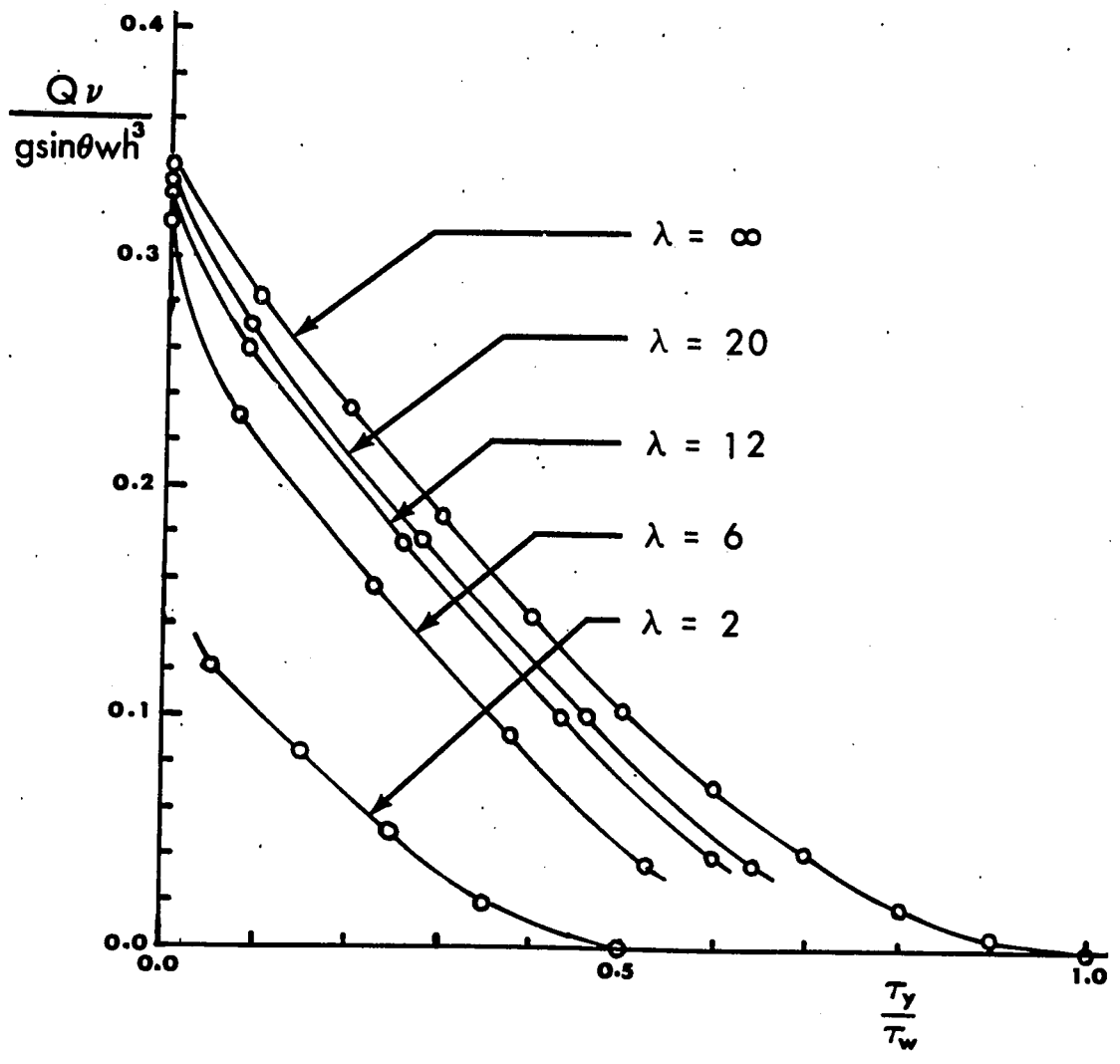

Fig. 3.6 $\frac{Q\nu}{g \sin\theta\, h^3\, W}$ vs. τ_y/τ_w for various λ's

where

$$\mu_a = \mu + \frac{\tau_y}{|\nabla u|}$$

for the viscous region, and

$$\nabla u = 0,\ u = \text{continuous on the yield surface} \qquad (3.31b)$$

for the plug flow region.

As has been stated earlier, due to the presence of the yield surface, calculation of the velocity field is somewhat difficult.

Johnson approached this problem by first solving for the stress field, which is briefly reviewed below.

The momentum equation, in the stress formulation can be written as

$$\frac{\partial \tau_{xz}}{\partial x} + \frac{\partial \tau_{xz}}{\partial y} = -\rho g \sin\theta \qquad (3.32)$$

Introduce a function Γ such that

$$\frac{\partial \Gamma}{\partial x} = \tau_{xz}\ ,\ \frac{\partial \Gamma}{\partial y} = \tau_{yz}\ .$$

Upon substitution of Γ into Eq.(3.32), there is obtained

$$\Gamma_{xx} + \Gamma_{yy} = -\rho g \sin\theta \qquad (3.33)$$

The boundary condition for Γ can be set as

$$\Gamma = 0 \quad \text{on the boundary} \qquad (3.34)$$

Detailed derivation of Eq.(3.34) can be found in Johnson. Note that Γ is a velocity like quantity.

The stress field becomes known by solving for Γ. The coordinate system appropriate to the problem is sketched in Fig. 3.7.

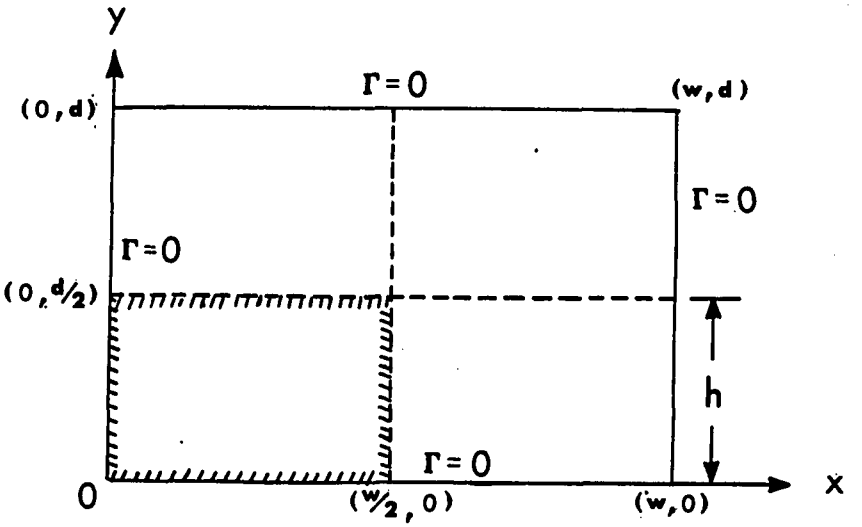

Fig. 3.7 Coordinate system for calculation of stress and velocity field

The solution procedure to Eq.(3.33) with boundary condition Eq.(3.34) is straight forward. (See standard books on partial differential equations, section for Poisson equation.)

Γ can be obtained as

$$\Gamma = \frac{\gamma}{2}(wx - x^2) - \frac{4\gamma}{\pi^3}\sum_{n=1}^{\infty}\left(\frac{\sin h\,(2n-1)\frac{\pi(d-y)}{w} + \sin h\,(2n-1)\frac{\pi y}{w}}{\sin h\,(2n-1)\frac{\pi d}{w}}\right)\frac{\sin\,(2n-1)\frac{\pi x}{w}}{(2n-1)^3} \tag{3.35}$$

where $\gamma = \rho g \sin\theta$

Since

$$\tau_{xz} = \frac{\partial \Gamma}{\partial x}, \text{ and } \tau_{yz} = \frac{\partial \Gamma}{\partial y},$$

we have

$$\tau_{xz} = \frac{\gamma}{2}(w-2x) - \frac{4w\gamma}{\pi^2}\sum_{n=1}^{\infty}\left(\frac{\sin h\,(2n-1)\frac{\pi(d-y)}{w} + \sin h\,(2n-1)\frac{\pi y}{w}}{\sin h\,(2n-1)\frac{\pi h}{w}}\right)\frac{\cos(2n-1)\,\pi x}{(2n-1)^2} \tag{3.36a}$$

$$\tau_{yz} = -\frac{4w\gamma}{\pi^2}\sum_{n=1}^{\infty}\frac{\sin h\,(2n-1)\frac{\pi x}{w}\left(\cosh(2n-1)\frac{\pi y}{w} - \cosh\frac{\pi(d-y)}{w}\right)}{(2n-1)^2 \sin h\,(2n-1)\frac{\pi h}{w}} \tag{3.36b}$$

The constitutive equations are

$$\tau_{xz} = \left(\mu + \frac{\tau_y}{\sqrt{\left(\frac{\partial u}{\partial x}\right)^2 + \left(\frac{\partial u}{\partial y}\right)^2}}\right)\frac{\partial u}{\partial x}$$

$$\tau_{yz} = \left(\mu + \frac{\tau_y}{\sqrt{\left(\frac{\partial u}{\partial x}\right)^2 + \left(\frac{\partial u}{\partial y}\right)^2}}\right)\frac{\partial u}{\partial y}$$

If these equations are substituted into Eq.(3.22), Eq.(3.31a) is obtained.

Along the line $y = \frac{d}{2}$, $\frac{\partial u}{\partial y} = 0$, thus $\tau_{yz} = 0$.

Along the line $x = \frac{w}{2}$, $\frac{\partial u}{\partial x} = 0$, thus $\tau_{xz} = 0$.

Therefore, velocity profiles along mid-planes (x = w/2, and y = d/2) can be calculated by using the relation,

$$\tau_{xz} = \mu\frac{du}{dx} + \tau_y \quad \text{along } y = \frac{d}{2}$$

$$\tau_{yz} = \mu\frac{du}{dy} + \tau_y \quad \text{along } x = \frac{w}{2}$$

Upon integration of the above equations with no slip condition, we get

$$u\left(x,\frac{d}{2}\right) = \frac{1}{\mu}\left[\frac{\gamma}{2}(wx-x^2) - \tau_{yx} - \frac{4\gamma w^2}{\pi^3}\sum_{n=1}^{\infty}\frac{\sin(2n-1)\frac{\pi x}{w}}{(2n-1)^3}\left(\frac{1.}{\cosh(2n-1)\frac{\pi d}{2w}}\right)\right] \quad (3.37a)$$

$$u\left(\frac{w}{2},y\right) = \frac{1}{\mu}\left[\frac{4\gamma w^2}{\pi^3}\sum_{n=1}^{\infty}\frac{(-1)^{n+1}}{(2n-1)^3}\left(1-\frac{\sinh(2n-1)\frac{\pi d-y}{w} + \sinh(2n-1)\frac{\pi y}{w}}{\sinh(2n-1)\frac{\pi d}{w}}\right) - \tau_y\, y\right] \quad (3.37b)$$

Note that if $d \to \infty$,

$u(x,\frac{d}{2}) \cong \frac{1}{\mu}\left[\frac{\gamma}{2}(wx-x^2) - \tau_y x\right]$, which is a familiar two dimensional velocity profile.

Velocity profiles of Eq.(3.37a) and Eq.(3.37b) are valid only in the viscous region.

With the knowledge of the stress field and velocity profiles along midplanes, the velocity profile can be calculated by simple iteration procedure, since the Eq.(3.31a) is elliptic. See the sketch of Fig. 3.8. Necessary calculation steps are:

i) Calculate stress field for given geometry

ii) Find yield surface for given yield strength by comparing the magnitude of stresses, $\tau_{mag} = \sqrt{(\tau_{xz})^2 + (\tau_{yz})^2}$ with yield strength

iii) Calculate velocity profiles along mid-planes for given yield strength and geometry

iv) Calculate velocity field by iteration

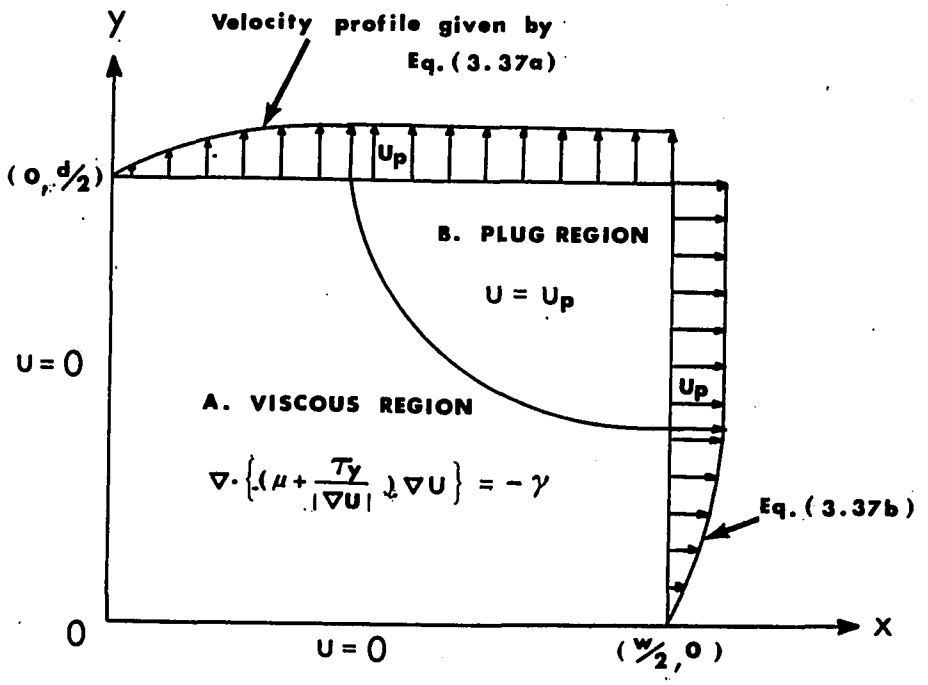

Fig. 3.8 Illustration of velocity field

A calculation procedure (different from the present one) using a known stress field can be found in Johnson and Hampton (27).

Calculation has been made with a (11 x 11) grid system with the following discretization schemes.

Eq.(3.31a) is non-dimensionalized with the following change of variables.

$$u^* = \frac{\mu u}{\gamma_W 2}$$

$$x^* = \frac{x}{W}$$

$$y^* = \frac{y}{d}$$

$$\frac{\tau_y}{\gamma d} = Bm \quad \text{(Bm stands for Bingham Number)}$$

$$\frac{d}{W} = \lambda_i \quad (\text{Note } \lambda_i = \frac{1}{\lambda})$$

The non-dimensionalized equation can be written explicitly as (*'s are omitted for convenience),

$$u_{xx} + \frac{1}{4\lambda_i^2} u_{yy} + Bm \cdot \frac{1}{2\lambda_i} \cdot \frac{u_{yy} u_y^2 - 2u_x u_y u_{xy} + u_x^2 u_{yy}}{\left(u_x^2 + \frac{1}{4\lambda_i^2} u_y^2 \right)^{3/2}} + 1 = 0 \qquad (3.38)$$

By rearranging, we obtain

$$Au_{xx} + Bu_{xy} + Cu_{yy} + 1 = 0$$

where

$$A = 1 + \frac{Bm}{2\lambda_i} \frac{u_y^2}{\left(u_x^2 + \frac{1}{4\lambda_i^2} u_y^2 \right)^{1.5}}$$

$$B = -\frac{Bm}{\lambda_i} \frac{u_x u_y}{\left(u_x^2 + \frac{1}{4\lambda_i^2} u_y^2 \right)^{1.5}}$$

$$C = \frac{1}{4\lambda_i^2} + \frac{Bm}{2\lambda_i} \frac{u_x^2}{\left(u_x^2 + \frac{1}{4\lambda_i^2} u_y^2 \right)^{1.5}}$$

By denoting the step size as Δh, the derivatives are discretized as follows.

$$u_{xx} \cong \frac{u_{i+1,j} - 2u_{i,j} + u_{i-1,j}}{(\Delta h)^2}$$

$$u_{yy} \cong \frac{u_{i,j+1} - 2u_{i,j} + u_{i,j-1}}{(\Delta h)^2}$$

$$u_{xy} \cong \frac{1}{2}\left(- \frac{u_{i-1,j+1} + u_{i+1,j-1} - 2u_{i,j}}{(\Delta h)^2} + u_{xx} + u_{yy} \right)$$

$$u_x \cong \frac{u_{i+1,j} - u_{i-1,j}}{2(\Delta h)}$$

$$u_y \cong \frac{u_{i,j+1} - u_{k,j-1}}{(2\Delta h)}$$

The coefficients A, B, and C were calculated from the velocity field of the previous iteration step, so that the Eq.(3.38) can be linearized.

The results of this calculation are plotted in Fig. 3.9.

For more thorough calculation, the step-size must be decreased as aspect ratio and Bingham number increase, in order to obtain reasonably accurate yield surface contours. No such attempts have been made here, since the purpose of the present calculation is to provide comparison with Kozicki's approximation theory. By comparing Fig. 3.9 with Fig. 3.6, we can see that Eq. (3.27) is a reasonable estimate.

Another method for solving the velocity field of a Bingham material for general geometry was suggested by Cea and Glowinski (28), who use an

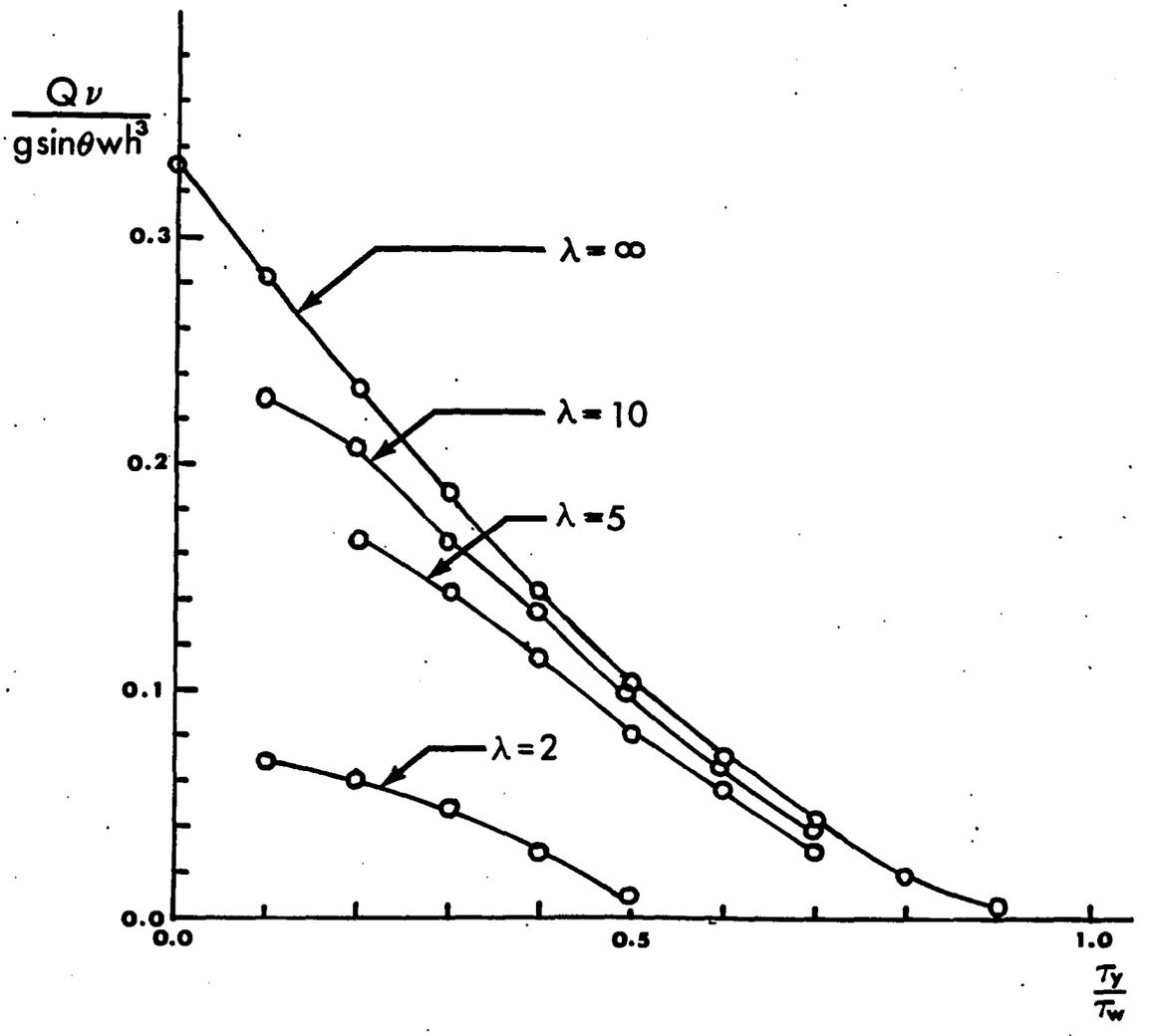

Fig. 3.9 Numerical results with (11x11) grid system

optimization technique.

3. Estimation of yield strength

There have been some efforts to estimate the yield strengths of flows by looking at the final flow dimensions (21, 29) using the model of Hulme (20). These attempts are based on the assumption that the final shapes of the flow depend strongly on the yield strength of the flowing material.

In this regard, equations discussed in previous sections may be useful in estimating the yield strengths for lava flows (or mud flows) which do occur commonly in channel configurations.

Let the estimated yield strength be τ_y determined from the final thickness of flow h_f.

In the two dimensional case (of infinite width), τ_y can be expressed as

$$\tau_y = \rho g \sin\theta h_f \tag{3.39}$$

But in the channel flow case, we have from Eq.(3.30),

$$\tau_y = \frac{\lambda}{\lambda+2} h_f(\rho g \sin\theta) \tag{3.40}$$

Clearly, as $\lambda \to \infty$, Eq.(3.40) tends to Eq.(3.39).

Eq.(3.40) is plotted in Fig. 3.10 for various values of $\lambda = \frac{W}{h_f}$.

Since the stress field is known, we are able to determine how much of the geometry will have stresses less than that predicted by Eq.(3.40). This is shown in Fig. 3.11.

It can be observed that estimates based on Eq.(3.40) are slightly higher than the yield strength. One reason for this might be the fact that the effective perimeter is longer than the geometric perimeter. See Fig. 3.12.

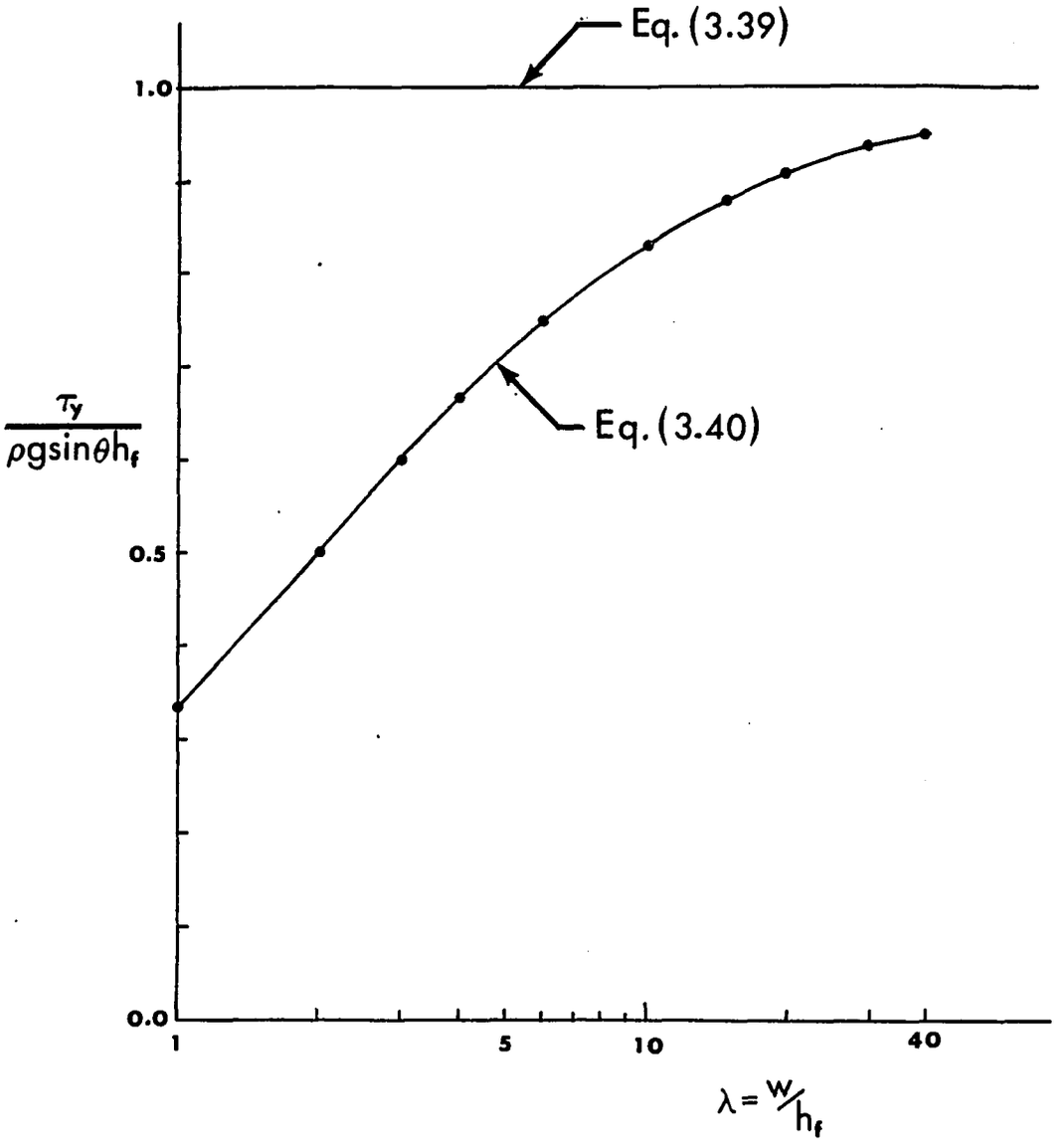

Fig. 3.10 Yield strength estimates for various aspect ratios

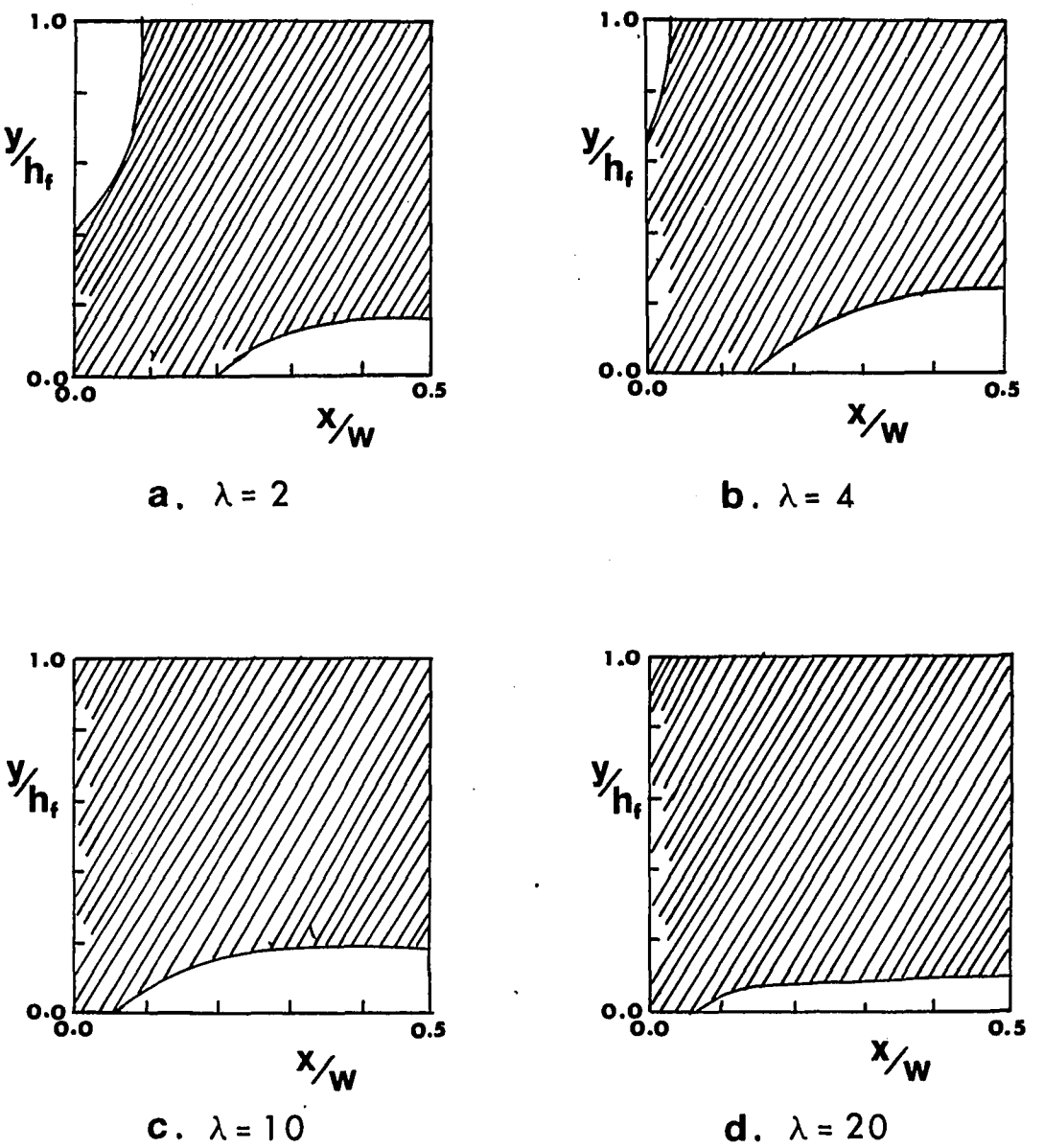

Fig. 3.11 Regions of smaller stresses (shaded area) than that predicted by Eq.(3.40)

(This is due to the low-stress zone around the corners. Johnson names these regions "dead regions".)

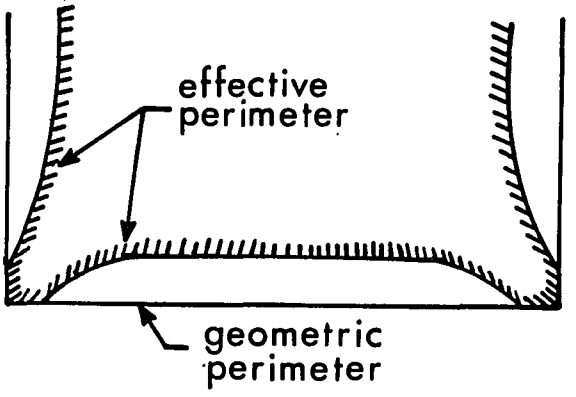

Fig. 3.12 Geometric perimeter and effective perimeter (approximate contour)

Iso-stress lines are shown in Fig. 3.13 a, b, c, d, for several aspect ratios, which were calculated from Eq.(3.36a) and (3.36b) for reference purposes.

4. Rivulet flow

a. Rivulet flow of Newtonian fluid In this section, we will briefly review the work done by Towell and Rothfeld (30).

Consider a Newtonian fluid flowing down an inclined plane with no walls (rivulet flow or sheet flow).

Coordinate system is shown in Fig. 3.14.

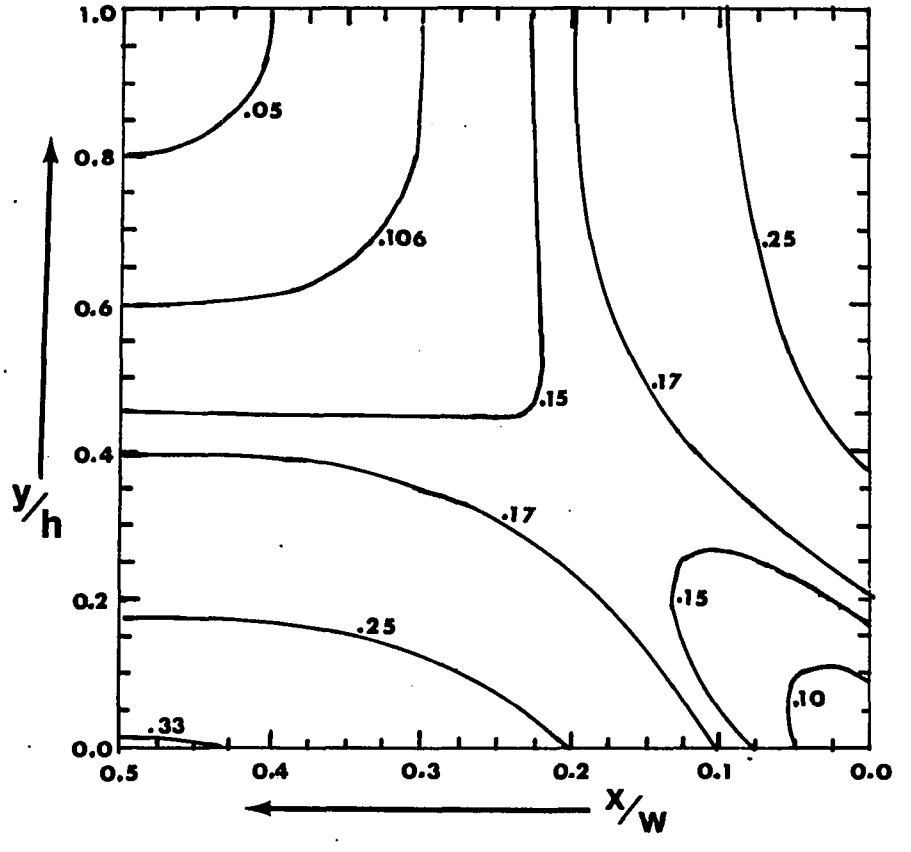

Fig. 3.13a Stress field for $\lambda = 2.0$ (numbers denote the values of $\sigma^* = \frac{\sigma}{\rho g \sin\theta W}$)

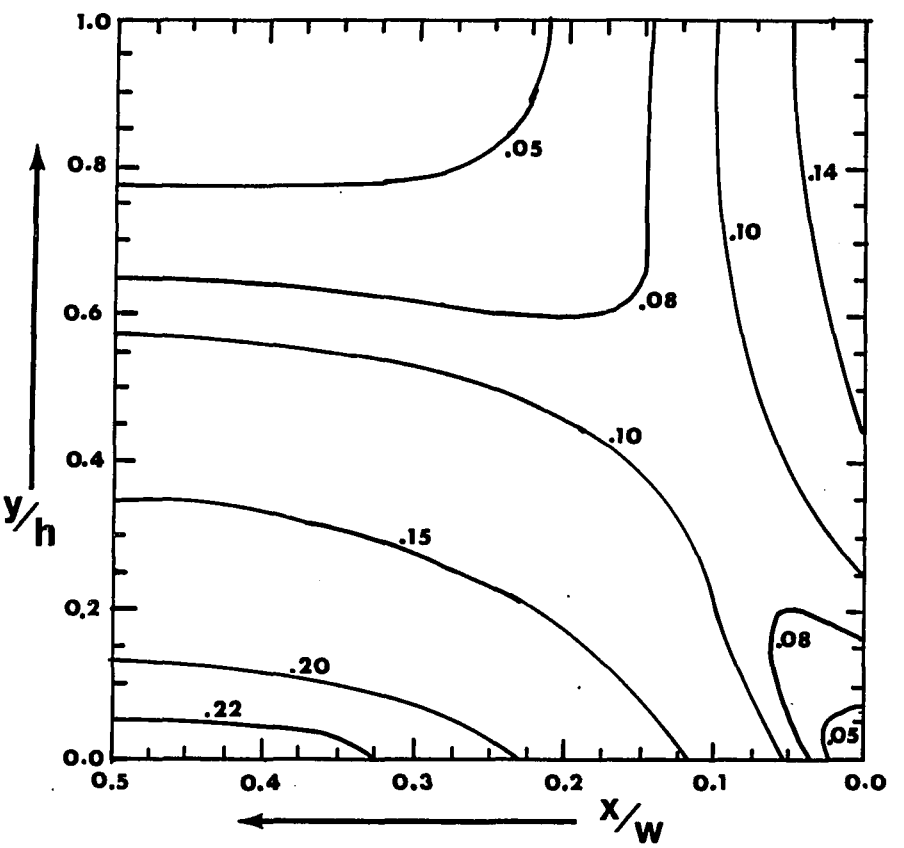

Fig. 3.13b Stress field for $\lambda = 4.0$

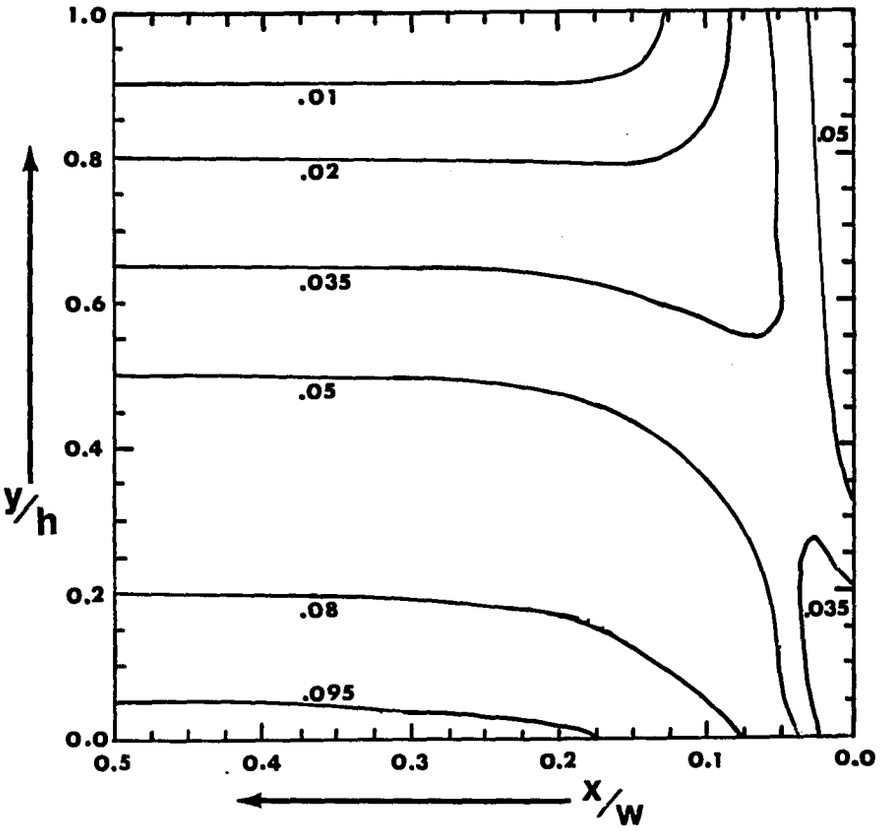

Fig. 3.13c Stress field for $\lambda = 10.0$

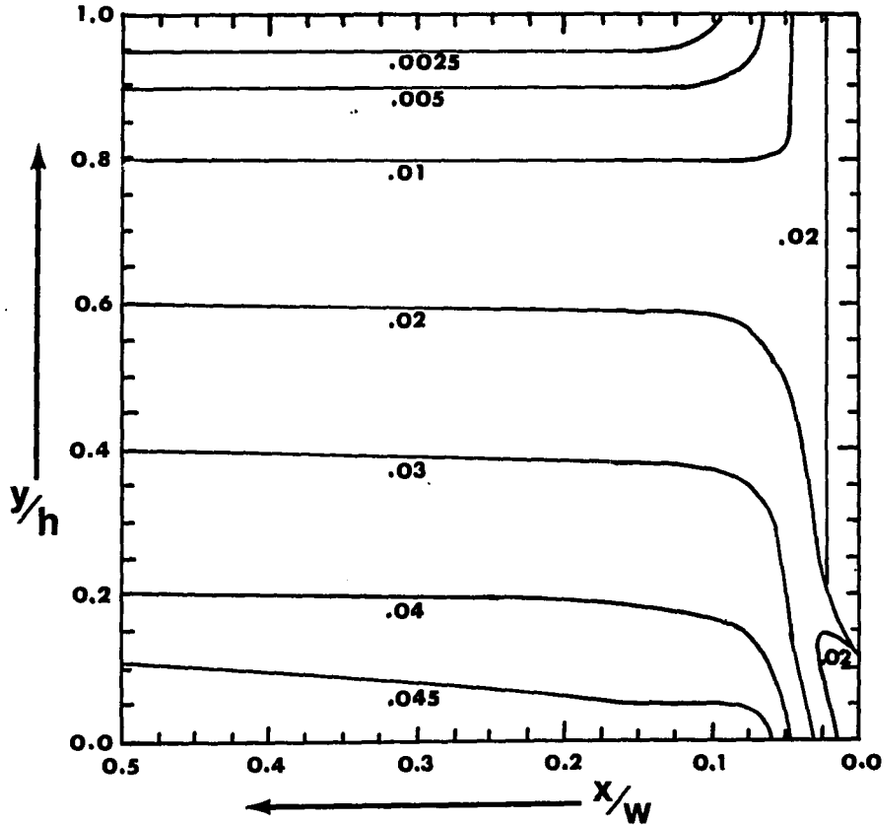

Fig. 3.13d Stress field for $\lambda = 20.0$

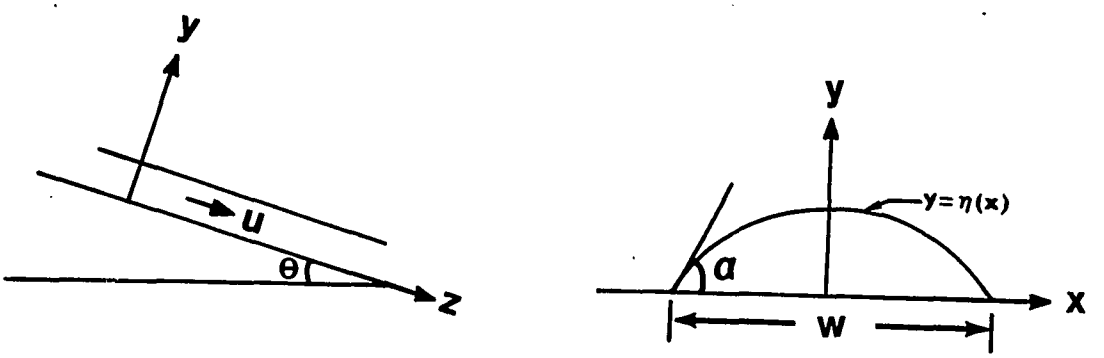

Fig. 3.14 Coordinate system for rivulet flow

We assume the following:

i) Unidirectional flow parallel to z axis (x and y components of velocity vanish)

ii) Fully developed flow, u = u(x, y)

iii) Steady state

iv) No shear at the gas-liquid interface

Then the Navier-Stokes equations with constant properties are:

$$\frac{\partial p}{\partial x} = 0 \tag{3.41}$$

$$\frac{\partial p}{\partial y} = -\rho g \cos\theta \tag{3.42}$$

$$\frac{\partial^2 u}{\partial x^2} + \frac{\partial^2 u}{\partial y^2} = -\frac{\rho g \sin\theta}{\mu} \tag{3.43}$$

Two boundary conditions can be derived from no-slip and symmetry property. They are,

$$u = 0 \quad \text{at} \quad y = 0 \tag{3.44}$$

$$u_x = 0 \quad \text{at} \quad x = 0 \tag{3.45}$$

At the gas liquid interface given by $y = \eta(x)$, the z component of shear stresses must vanish. This results in

$$|\eta'| \frac{\partial u}{\partial x} + \frac{\partial u}{\partial y} = 0 \quad \text{at } y = \eta \tag{3.46}$$

To solve Eq.(3.43) subject to the conditions Eq.(3.44) to (3.46), the equation for the interface $\eta(x)$ must be known.

This can be achieved for a given contact angle α and stream width W, by using the well-known relation

$$p(\eta) = p_g - \frac{\sigma \eta''}{(1+\eta')^{3/2}} \tag{3.47}$$

where $p(\eta) = \lim_{y \to \eta -}(p)$, and σ is surface tension.

Eq.(3.47) can be written as, (by using Eq.3.42))

$$\frac{Y''}{(1+Y'^2)^{3/2}} = \frac{a}{b} + Y \tag{3.48}$$

where $Y = (\eta_o - \eta)/a$, and the prime denote differentiation with respect to $X = x/a$, and $a = \sqrt{\sigma / \rho g \cos\theta}$, the capillary length.

The constant b is derived from other constants and is seen to be the radius of curvature at $Y = 0$.

Eq.(3.48) generates a family of curves Y vs. X with a/b as parameter which can be determined from the choice of stream width and contact angle.

Rather than discussing the general solution procedures, two simple cases will be discussed.

An analytical solution of Eq.(3.43) with the given interface shape (Eq.3.48)) is mathematically intractable.

An approximate solution can be easily obtained by assuming that

$$\frac{\partial^2 u}{\partial x^2} << \frac{\partial^2 u}{\partial y^2}$$

which is reasonable except for the region around the edge of the rivulet.

For very small rivulets, where the radius of curvature is very small, $a/b >> Y$ and Eq.(3.48) describes a circle. Therefore, the cross section of the stream is a sector of a circle with its chord length equal to the width.

After carrying suitable integrations, we can arrive at

$$\frac{Q\,\mu}{\rho\, w^4\, g \sin\theta} = \frac{f(\alpha)}{192} \tag{3.49}$$

where

$$f(\alpha) = \frac{12\,\alpha\cos^2\alpha + 3\,\alpha - 2\cos^3\alpha\sin\alpha - 13\cos\alpha\sin\alpha}{\sin^4\alpha}$$

In this case, we can see that the stream width is extremely sensitive to the contact angle, and for a given contact angle, the stream width is proportional to the one quarter power of the product of flow rate and kinematic viscosity. As the flow rate increases, the rivulet widens and deepens. As the rivulet widens and deepens the shape, which is mainly governed by surface tension for small rivulets, is affected by both surface tension and gravity.

If the stream becomes wide and flat enough, so that

$$a/b << Y,$$

then, according to Rayleigh's solution (31), the maximum depth is

$$Y_o = 2\sin(\alpha/2).$$

As the flow rate increases, the stream widens but no longer deepens. In

this case, the flow rate may be calculated by assuming that the cross-section is rectangular with depth $2 \sin(\alpha/2)$.

Hence,

$$\frac{Q\mu \cot\theta}{W\sigma}\sqrt{\frac{\rho g \cos\theta}{\sigma}} = \frac{8}{3}\sin^3(\alpha/2) \qquad (3.50)$$

Again the rivulet width is seen to be sensitive to contact angle, is a strong function of surface tension ($\alpha\sigma^{-1.5}$) and is proportional to the flow rate and viscosity.

If the Rayleigh relation

$$h = \sqrt{\frac{\sigma}{\rho g \cos\theta}} \cdot 2\sin(\alpha/2)$$

is substituted in Eq.(3.50), we get

$$\frac{Q\mu}{\rho g \sin\theta W h^3} = \frac{1}{3}$$

which is the equation developed earlier (Eq.(3.12)). This shows that, even though the depth is determined from surface tension and contact angle, if we take depth h as dominant variable, then for a fairly wide flat rivulet, contact angle and surface tension do not necessarily have to come in to the discussion.

b. Rivulet flow of Bingham plastic-model of Hulme Consider a Bingham plastic fluid flowing down a slope, as in Fig. 3.14. Hulme (20) assumed that the cross-sectional shape is governed by the yield strength of the flowing material.

Based upon balance of forces, lateral movement will cease if

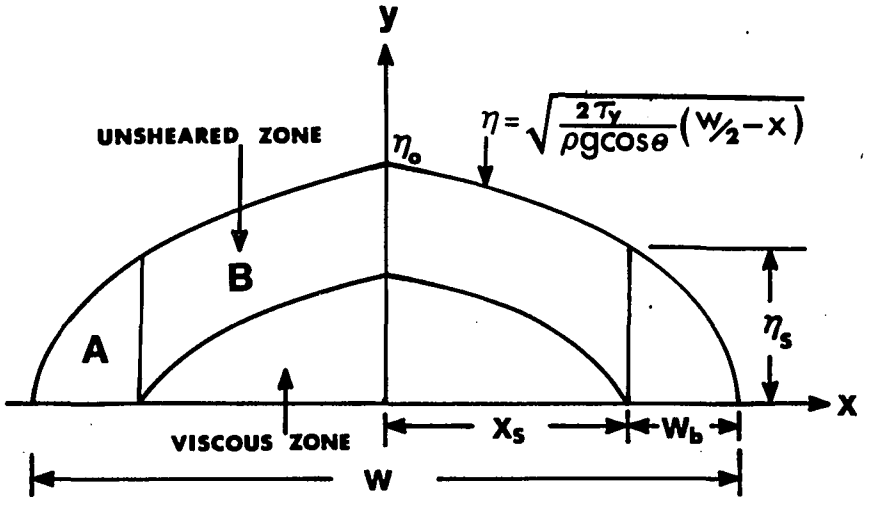

Fig. 3.15a Schematic diagram illustrating Hulme's idea

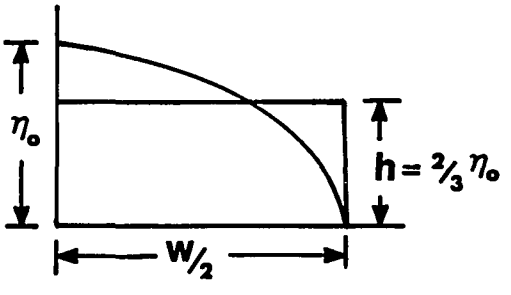

Fig. 3.15b Rectangle giving same area as parabola

$$\tau_y = -\rho g \cos\theta \eta \frac{d\eta}{dx} \tag{3.51}$$[1]

This equation can be easily integrated to give

$$\eta^2 = \frac{2\tau_y}{\rho g \cos\theta}\left(\frac{W}{2} - x\right) \tag{3.52}$$

Hence, the flow depth at the centerline is

$$\eta_o^2 = \frac{\tau_y W}{\rho g \cos\theta} \tag{3.53}$$

Further, down hill movement will cease, if

$$\tau_y = \rho g \sin\theta \eta_s \tag{3.54}$$

Following these ideas, the rivulet flow model suggested by Hulme is shown schematically in Fig. 3.15a.

From Eq.(3.53) and (3.54), we get

$$\eta_o^2 = W \eta_s \tan\theta$$

To calculate volume flow rate, the 2-dimensional velocity profile of Eq.(3.20) is integrated over the dimensions shown in Fig. 3.15. That is,

$$Q = 2\left\{\int_o^{x_s}\left[\int_o^{\eta-\eta_s} \frac{\rho g \sin\theta}{\mu}\left(h_s y - \frac{y^2}{2}\right)dy + \int_{\eta-\eta_s}^{\eta} \frac{\rho g \sin\theta}{2\mu} h_s^2 \, dy\right] dx\right\}$$

where $h_s = \eta - \eta_s$.

The integration is easily carried out to give, after some algebraic manipu-

---

[1]Originally, Hulme used $\rho g \eta \frac{d\eta}{dx}$, but it seems more proper to replace g by $g \cos\theta$.

lations:

$$Q = \frac{\rho g \cos\theta \eta_s^4}{\mu} \left[\frac{2}{15}\left(\frac{\eta_o}{\eta_s}\right)^5 - \frac{1}{4}\left(\frac{\eta_o}{\eta_s}\right)^4 + \frac{1}{6}\left(\frac{\eta_o}{\eta_s}\right)^2 - \frac{1}{20}\right] \tag{3.55}$$

By considering W_b to be the levee width observed in natural flows, Eq.(3.55) can be evaluated without knowing the cross-sectional configuration, since

$$\frac{\eta_o}{\eta_s} = \sqrt{\frac{W}{W_b}} \tag{3.56}$$

However, some points in this model need discussion.

Regardless of the validity of the assumptions that lead to Eq.(3.51), it is seen that the equation doesn't satisfy the condition of symmetry, i.e.

$$\frac{d\eta}{dx}\Big)_{x=0} = 0 \ .$$

as Hulme pointed out. Therefore, the shape develops a cusp at x=0. Hulme's measurements of center depth η_o were about 3/4 of those predicted by the equation (see Fig. 10 of Ref. 20). Noting that the height (or depth) of a rectangle of the same width as the parabola that will give the same area as the parabola is 2/3 η_o (see Fig. 3.15b), the flow cross-section of a wide flow might be viewed as a rectangle rather than as a parabola as in the case of a wide flat rivulet flow of Newtonian fluid. Careful examination of Hulme's data shows that measured central depths are in the range of $\frac{3}{5} \sim \frac{5}{6}$ of predicted depths.

According to the model, Region A of Fig. 3.15a can hardly be interpreted as levees. (See Fig. 3.16 for actual levee geometry,) The region where $\eta > \eta_s$ will flow only until the surface height reaches η_s, so that

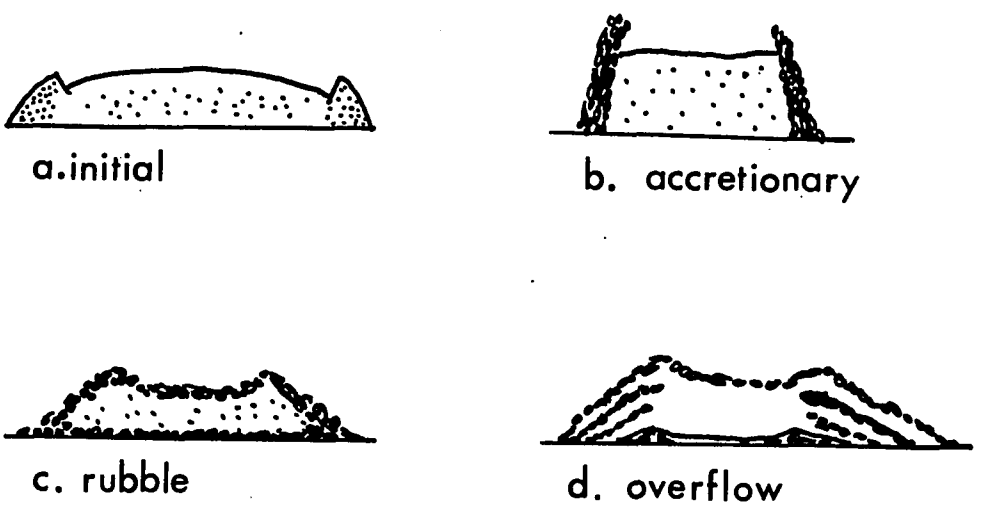

Fig. 3.16 Cross-sections through the four different types of lava levees observed on Mt. Etna. Stippled parts of diagram indicate massive lava; the sparsely stippled areas represent flowing lava (Ref. 32:270)

after flow ceases, there would be no distinction in height between region B and A.

In this respect, Iversen's model (33) seems more appropriate, where the yield strength is a function of width and assumes a maximum value at the edge and minimum at the center.

However, in this study the levee will not be given a special consideration, rather it will be viewed as an indication of flowing thickness (or depth).

5. Motion of free surface

This section is not directly related to the discussion of simulation or the modeling process, but by looking at the equation of surface motion, we can get some intuitive ideas of associated length and time scales. Sometimes, lava flows are accompanied by wave motion. See Fig. 3.17.

The coordinate system relevant to the problem is shown in Fig. 3.18.

Without considering surface tension, the following set of equations can be written.

$$u_x + v_y = 0 \tag{3.57a}$$

$$p = \rho g \cos\theta \, (\eta - y) \tag{3.57b}$$

$$\nu \nabla^2 u = \frac{1}{\rho} p_x - g \sin\theta \tag{3.57c}$$

$$\eta_t + u \eta_x = v \text{ at } y = \eta \tag{3.57d}$$

Eq.(3.57b) assumes static pressure relation along y, which is derived from the y-momentum equation by neglecting the viscous force term due to the y component of velocity.

Eq.(3.57b) is a kinematic condition which has to be satisfied at the surface.

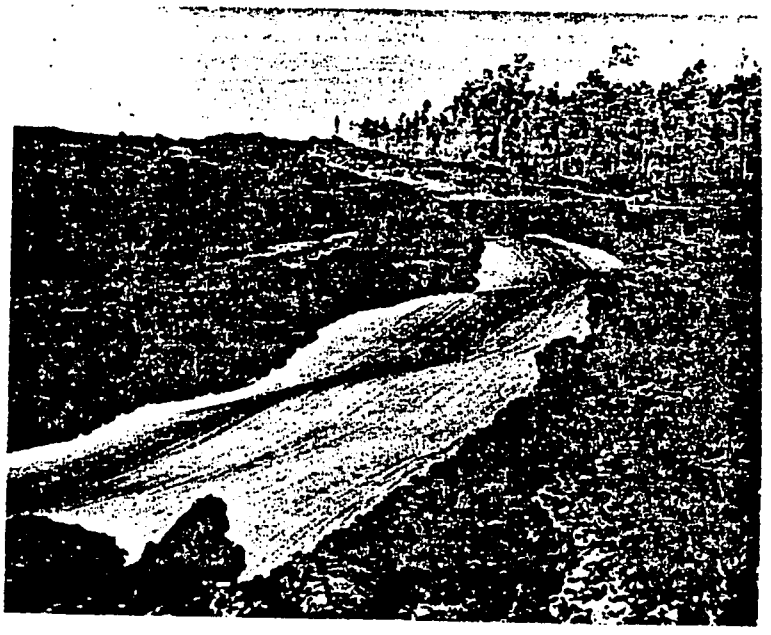

Fig. 3.17 Feeding river of the lava flow of Mauna Loa, October 6, 1919. The surface of the river has not yet formed a crust. Note the standing waves in the river (Ref. 15:83)

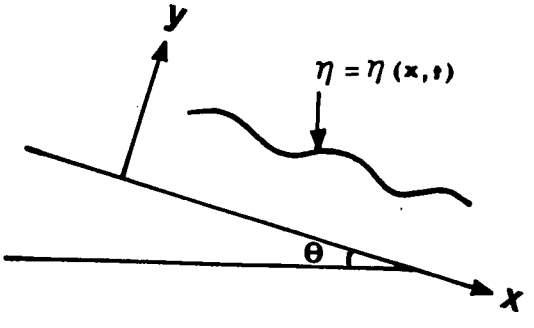

Fig. 3.18 Coordinate system for the surface motion

Eq.(3.57a) and (3.57c) are the continuity equation and x-momentum equation respectively.

By assuming

$$u_{xx} \ll u_{yy}$$

the above equations can be easily integrated to give:

$$\eta_t + \frac{g \sin\theta}{\nu} \eta_x \eta^2 = \frac{g \cos\theta}{3\nu} \left(\eta_x \eta^3\right)_x \tag{3.58}$$

This is a non-linear wave equation with diffusion. More rigorous derivation of the above equation can be found in Mei (34) who used perturbation analysis. Eq.(3.58) can be non-dimensionalized by introducing

$$\bar{\eta} = \frac{\eta}{(\nu^2/g)^{1/3}}, \quad \tau = \frac{t}{(\nu/g^2)^{1/3}}, \quad \bar{x} = \frac{x}{(\nu^2/g)^{1/3}} \tag{3.59}$$

to yield

$$\bar{\eta}_\tau + \bar{\eta}^2 \sin\theta \, \bar{\eta}_{\bar{x}} = \frac{\cos\theta}{3} \left(\bar{\eta}^3 \bar{\eta}_{\bar{x}}\right)_{\bar{x}} \tag{3.60}$$

Note that if $\theta = 0$, Eq.(3.60) becomes a diffusion type, so that no wave features are expected. Thus, if θ is very small, distinct wave motion can hardly be expected. The reference length scale $(\nu^2/g)^{1/3}$ and time scale $(\nu/g^2)^{1/3}$ are both very small and pertinent to vertical motion.

6. 1-dimensional, unsteady heat conduction with radiative boundary condition

So far we have considered isothermal flows only. In this section, we will take a look at a very simple heat transfer problem. Consider a heat conduction problem shown in Fig. 3.19.

Assuming constant thermal properties (ρ, Cp, k), the heat equation becomes,

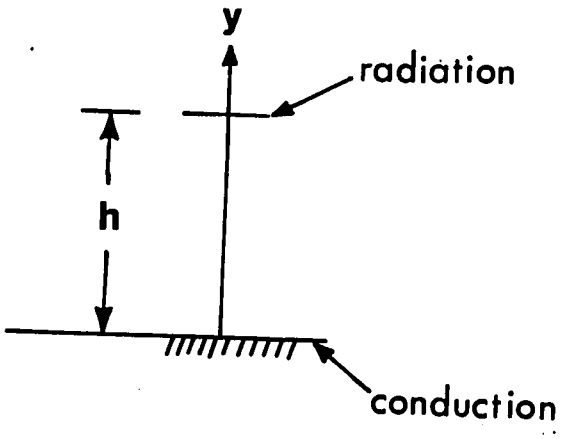

Fig. 3.19 Coordinate system for 1-dimensional heat conduction problem

$$\frac{\partial T}{\partial t} = \alpha \frac{\partial^2 T}{\partial y^2} \tag{3.61}$$

with boundary conditions

$$T = T_c \ , \ y = 0 \tag{3.62a}$$

$$-k \frac{\partial T}{\partial y} = \varepsilon \sigma T_h^4 \ , \ y = h \tag{3.62b}$$

where

$\alpha = \frac{\kappa}{\rho Cp}$ = thermal diffusivity

κ = conductivity

Cp = specific heat at constant pressure

ε = emissivity

σ = Stefan Boltzman constant

T_c = contact temperature

T_h = temperature of the surface (y = h)

One reason for choosing Eq.(3.61) is that it can be interpreted as a quasi-steady flow temperature profile, via the transformation

$$t = \frac{x}{U_{av}}$$

To meet this need, the contact temperature is chosen somewhat differently from the usual wall temperature condition.

If the magma is extruded at temperature T_o and makes contact with country rock, the temperature of contact, T_c, assumes the value (35),

$$T_c = \frac{T_o}{2} (1-p^2) \sum_{n=1}^{\infty} (-p)^{n-1} \left\{ I\left(\frac{nh}{2\sqrt{\alpha_1 t}} \right) \right\} \tag{3.63}$$

where

$$I = \frac{2}{\sqrt{\pi}} \int_0^x e^{-u^2} du$$

$$p = \frac{\alpha_1^2 k_2 - \alpha_2^2 k_1}{\alpha_1^2 k_2 + \alpha_2^2 k_1}$$

The constants α_1, k_1, and α_2, k_2 are diffusivities and conductivities of magma and country rock respectively.

If $\frac{nh}{2\sqrt{\alpha_1 t}} > 3.0$,

$$T_c \cong \frac{T_o}{2} (1-p) \tag{3.64}$$

Therefore, if we assume

$$\alpha_1 \cong \alpha_2 \quad , \quad k_1 \cong k_2 \ ,$$

$$T_c = \frac{T_o}{2} \tag{3.65}$$

Thus we see that the initial contact temperature is about half of the temperature of the hot body if thermal properties are similar to those of the cold body. The initial contact temperature given in Jaeger (36) gives the same result.

The boundary condition Eq.(3.62b) comes from the radiation at the surface. For the relatively simple radiation case, where in the area A_1 with temperature T_1 has an entirely convex surface and is completely surrounded by a surface A_2 at temperature T_2, then the radiative heat flux is

$$q_r = \frac{\sigma \left(T_1^4 - T_2^4 \right)}{\left[\frac{1}{\varepsilon_1} + \frac{A_1}{A_2} \left(\frac{1}{\varepsilon_2} - 1 \right) \right]} \tag{3.66}$$

If $T_2 << T_1$, and $A_1 << A_2$, then

$$q_r \approx \varepsilon_1 \sigma T_1^4 \tag{3.67}$$

which gives the boundary condition Eq.(3.62b).

Introducing

$$\tau = \frac{\alpha t}{h^2} \; ; \quad \bar{y} = \frac{y}{h} \; ; \quad \theta = \frac{T}{T_o}$$

the equations (3.61) to (3.62b) reduce to

$$\frac{\partial \theta}{\partial \tau} = \frac{\partial^2 \theta}{\partial \bar{y}^2} \tag{3.68a}$$

$$\theta = 0.5, \quad \bar{y} = 0 \tag{3.68b}$$

$$-\frac{\partial \theta}{\partial \bar{y}} = \frac{h \varepsilon \sigma T_o^3}{k} \theta_1^4 \; , \quad \bar{y} = 1 \tag{3.68c}$$

The above set of equations has been solved numerically for a specific case by using the alternating direction explicit scheme (A.D.E.) suggested by Larkin (37), incorporated with a Newton-Raphson solver for non-linear equation that arises from Eq.(3.68c).

The finite difference approximations are

$$\frac{p_{i,n+1} - \theta_{i,n}}{\Delta \tau} = \frac{p_{i-1,n+1} - p_{i,n+1} - \theta_{i,n} + \theta_{i+1,n}}{(\Delta y)^2} \tag{3.69a}$$

$$\frac{q_{i,n+1} - \theta_{i,n}}{\Delta \tau} = \frac{\theta_{i-1,n} - \theta_{i,n} - q_{i,n+1} + q_{i+1,n+1}}{(\Delta y)^2} \tag{3.69b}$$

followed by

$$\theta_{i,n+1} = \frac{1}{2} \left(p_{i,n+1} + q_{i,n+1} \right) \tag{3.69c}$$

subscripts i and n are for space and time respectively.

Eq.(3.69a) is for marching in the positive (y+) direction and Eq.(3.69b) is for the negative (y-) direction.

Eq.(3.68c) is discretized as

$$\frac{4\theta_{k-1,n} - 3\theta_{k,n+1} - \theta_{k-2,n}}{2\Delta y} = S_f \cdot \theta^4_{k,n+1}$$

where S_f stands for Stefan No., $\frac{h\varepsilon\sigma T_o^3}{k}$. (Subscript i runs from 1 to k.)

Hence, the above discretization results in a non-linear algebraic equation of type

$$X^4 + bx + d = 0 ,$$

which can be solved by the Newton-Raphson method as has been mentioned.

The results of this calculation (for basalt flow of 3m thickness) are shown in Fig. 3.20. We can see that the radiative heat transfer is very effective, so that the crust may solidify in less than an hour after extrusion. (If it solidifies at 1100°C, $T/T_o \approx 0.93$ in the example case.)

7. Simple dynamic lava flow model considering heat exchange

In this section Harrison and Rooth's model (11) will be briefly reviewed and extended to the Bingham plastic case.

Consider a quasi-stationary regime where the flow is laminar, and constant flow rate is maintained. Assume that heat is mainly lost by radiation, and that the gradient generated by variation of thickness of the flow is much smaller than the topographic gradient. Assume further that the temperature T and viscosity μ are locally averaged (across the thickness) and density ρ and specific heat C_p are constants.

Considering a heat balance as in Fig. 3.21, we have

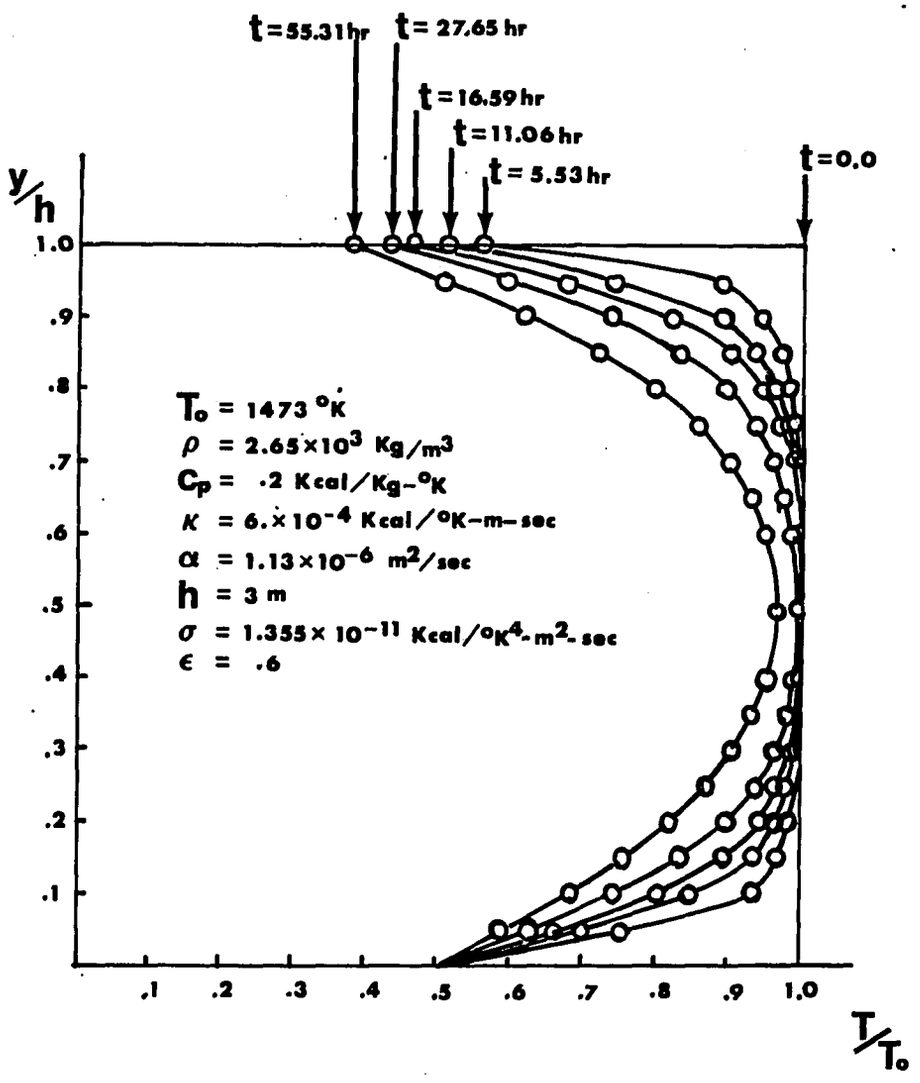

Fig. 3.20 Temperature profile of basalt of 3m thickness

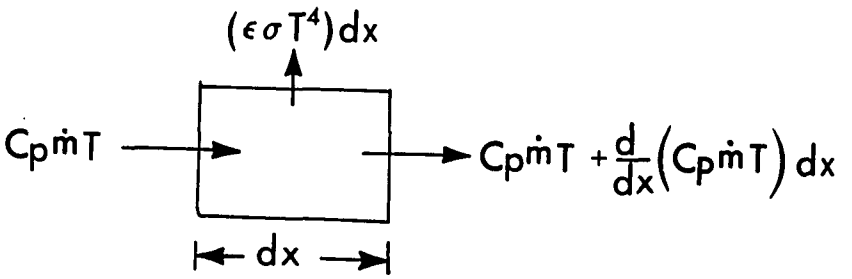

Fig. 3.21 Diagram illustrating heat exchange

$$\frac{d}{dx}\,(C_p \dot{m} T) + \varepsilon \sigma T^4 = 0 \tag{3.70}$$

where ε = emissivity

σ = Stefan-Boltzman constant

$\dot{m}$ = mass flow rate per unit width

Eq.(3.70) is easily integrated to give

$$\frac{1}{T^3} - \frac{1}{T_o^3} = \frac{3\,\varepsilon\sigma\,x}{C_p \dot{m}} \tag{3.71}$$

Thus, in this heat exchange model, variation of temperature with distance is independent of the mechanics of the flow.

One sample calculation of the results of Eq.(3.71) is shown in Fig. 3.22.

Now the mass flow rate can be written as (see Eq.(3.11))

$$\dot{m} = \frac{\rho^2 g \sin\theta\, h^3}{3\,\mu} \tag{3.72}$$

And viscosity varies with temperature as

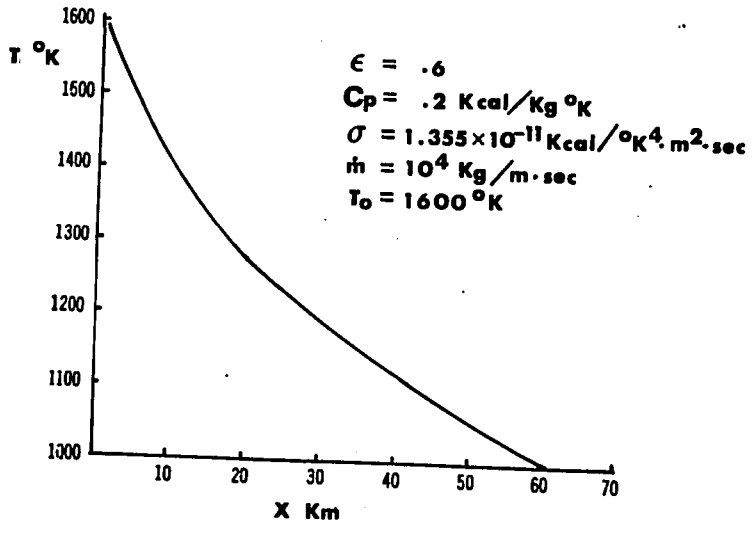

Fig. 3.22 Temperature of lava and distance traveled (Ref. 11:106)

$$\mu = \mu_o (b/T) \tag{3.73}$$

The time taken for a flow to proceed can be calculated in the following manner.

$$u = \frac{\dot{m}}{\rho h} = \frac{dx}{dt}$$

$$\frac{dx}{dt} = - \frac{C_p \dot{m}}{\varepsilon \sigma T^4} \frac{dT}{dt}$$

Therefore,

$$\frac{dT}{dt} = - \frac{\varepsilon \sigma T^4}{C_p} \left(\frac{g \sin \theta}{3 \rho \mu_o \exp (b/T) \cdot \dot{m}} \right)^{1/3}$$

or

$$\int_{T_o}^{T_1} - \frac{\exp(b/3T)}{T^4} dT = \frac{\varepsilon \sigma}{C_p} \left(\frac{g \sin \theta}{\rho \mu_o \dot{m}} \right)^{1/3} \cdot t$$

This can be integrated to give

$$t = - \frac{C_p}{\varepsilon \sigma} \left(\frac{3 \rho \mu_o \dot{m}}{g \sin \theta} \right)^{1/3} \cdot \left[\exp(b/3T) \cdot \left(\frac{18}{b^2 T} - \frac{54}{b^3} - \frac{3}{bT^2} \right) \right]_{T_o}^{T_1} \tag{3.74}$$

It is seen that the time (t) taken for the lava to cool from T_o to T_1 varies as $(\dot{m} / \sin \theta)^{1/3}$ or as the one third power of (initial) thickness.

Several example calculations of Eq.(3.74) are shown in Fig. 3.23.

Danes (38) has used a similar approach to calculate lava flow thicknesses that will be able to travel certain (given) distances.

The model discussed above can be easily extended to Bingham plastics. Instead of using Eq.(3.72) we take

$$\dot{m} = \frac{\rho^2 g \sin \theta h^3}{3 \mu} \left[1 - \frac{3}{2} \left(\frac{\tau_y}{\tau_W} \right) + \frac{1}{2} \left(\frac{\tau_y}{\tau_W} \right)^3 \right] \tag{3.75}$$

which is the flow rate equation for Bingham plastic (see Eq.(3.22a)).

We consider that for a given slope and $\dot{m}$, thickness h changes according to Eq.(3.75) as τ_y / τ_w and μ vary (thickness adjusts itself to property variations).

Since μ and τ_y vary strongly with temperature, it would be interesting to see how $\frac{\tau_y}{\tau_w}$ and h vary with length.

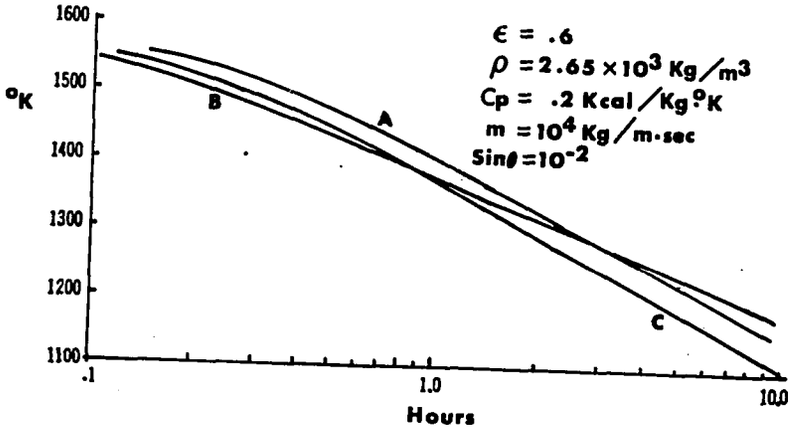

A; $b = 2.917 \times 10^4$ °K
$\mu_o = 1.877 \times 10^{-7}$ kg/m-sec
(from Murase & McBirney (39))

B; $b = 4.657 \times 10^4$ °K
$\mu_o = 5.888 \times 10^{-13}$ kg/m-sec
(from Shaw & Swanson (40), retarded crystallization)

C; $b = 2.668 \times 10^4$ °K
$\mu_o = 4.315 \times 10^{-7}$ kg/m-sec
(from Shaw & Swanson (40), curve above liquidus)

Fig. 3.23 Time taken for a flow to cool down from 1600°K for various viscosity variations (Ref. 11:107)

This can be done as follows. Eq.(3.75) is differentiated with respect to x, to give

$$\frac{3\dot{m}}{\rho^2 g \sin\theta}\frac{d\mu}{dx} = 3h^2\frac{dh}{dx}\left[1-\frac{3}{2}\left(\frac{\tau_y}{\tau_W}\right)+\frac{1}{2}\left(\frac{\tau_y}{\tau_W}\right)^3\right]$$

$$+ h^3\left(\frac{\frac{d\tau_y}{dx}\tau_W - \tau_y \rho g \sin\theta \frac{dh}{dx}}{\tau_W^2}\right)\left[-\frac{3}{2}+\frac{3}{2}\left(\frac{\tau_y}{\tau_W}\right)^2\right]$$

Rearranging the above equation yields,

$$\frac{dh}{dx} = \frac{\frac{\dot{m}}{\rho^2 g \sin\theta}\frac{d\mu}{dx} + \frac{h^3}{2}\frac{1}{\tau_W}\left[1-\left(\frac{\tau_y}{\tau_W}\right)^2\right]\frac{d\tau_y}{dx}}{h^2\left(1-\frac{\tau_y}{\tau_W}\right)} \qquad (3.76)$$

The derivatives $\frac{d\mu}{dx}$ and $\frac{d\tau_y}{dx}$ are calculated by

$$\frac{d\mu}{dx} = \frac{d\mu}{dT}\frac{dT}{dx} = \mu_o \exp(b/T)\left(\frac{b\varepsilon\sigma T^2}{C_p\dot{m}}\right) \qquad (3.77)$$

$$\frac{d\tau_y}{dx} = \frac{d\tau_y}{dT}\frac{dT}{dx} = -\frac{\varepsilon\sigma T^4}{C_p\dot{m}}\frac{d\tau_y}{dT} \qquad (3.78)$$

Eq.(3.76) can be integrated numerically with the aid of Eq.(3.71) to give length versus thickness and length versus τ_y/τ_W for a given mass flow rate and slope.

Results of the calculation for four different cases are shown in Fig. 3.24a and 3.24b.

For viscosity calculation,

$$\mu_o = 4.315 \times 10^{-7} \text{kg/m-sec}$$

$$b = 2.668 \times 10^4 \ ^\circ\text{K}$$

were used (see Fig. 3.23, case c).

For $\tau_y(T)$, $\frac{d\tau_y}{dT}(T)$, yield strengths from Makaopuhi lava lake (Fig. 2.3) were used with the following approximation.

$$\tau_y = 0 \qquad T \geq 1200$$

$$\tau_y = 0.4(1200-T) \times 10^2 \qquad 1175 \leq T \leq 1200$$

$$\tau_y = \{10 + 2.08\ (1175-T)\} \times 10^2 \qquad 1150 \leq T \leq 1175$$

$$\tau_y = \{62\cdot + 0.2667(1150-T)\} \times 10^2 \qquad 1120 \leq T \leq 1150$$

$$\tau_y = 7\cdot \times 10^3 \qquad T \leq 1120$$

where τ_y is in N/m^2

T is in °C

From the graphs presented, some important observations can be made.

Firstly, flows tend to be stopped or diverted (or overflows may occur) due to rapid increase in yield strength, depending on the status of lava supply. Note that rapid increase in thickness is the direct result of rapid increase in yield strength.

Even though the increase in thickness is considerable (2 or 3 times thicker than the initial thickness), this may not be noticeable in the field, since that increase in thickness takes place over kilometers.

Secondly, by comparing Fig. 3.24a and b, the importance of flow rate ($\dot{m}$) can be realized. Note that, in the flow with $\dot{m} = 10^4$ kg/m-sec (Fig. 3.24b), the ratio of τ_y/τ_W reaches 0.9 in about 0.8 km, whereas 0.9 is reached after about 8 km in the flow with $\dot{m} = 10^5$ kg/m-sec (Fig. 3.25a),

when $\varepsilon = 0.6$.

This can be explained in terms of rate of temperature drop per unit length.

From Eq.(3.70), we have approximately

$$-\frac{dT}{dx} \propto \frac{1}{\dot{m}}$$

Hence, the temperature drop would be ten times slower when the flow rate is ten times higher.

So it is likely that lava extruded at slow flow rate tends to generate several flow units (compound flows) if extrusion lasts long enough, while lava extruded at high flow rates tends to flow in a single unit.

In Fig. 3.25a and b, temperature variations are shown along the length traveled (supplemental to Fig. 3.24a and b).

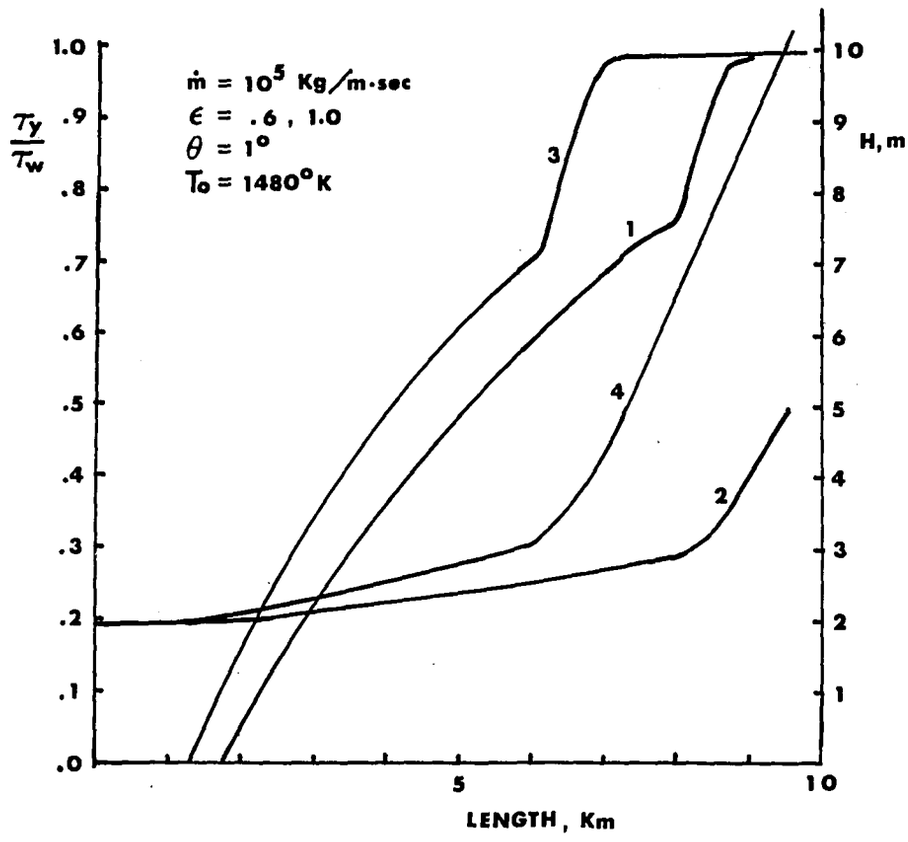

1. τ_y/τ_W ; use left scale
2. Thickness (h); use right scale

} ε = 0.6

3. τ_y/τ_W ; use left scale
4. Thickness; use right scale

} ε = 1.0

* step size ΔX = 0.05 km

Fig. 3.24a Thickness and τ_y / τ_w vs. length

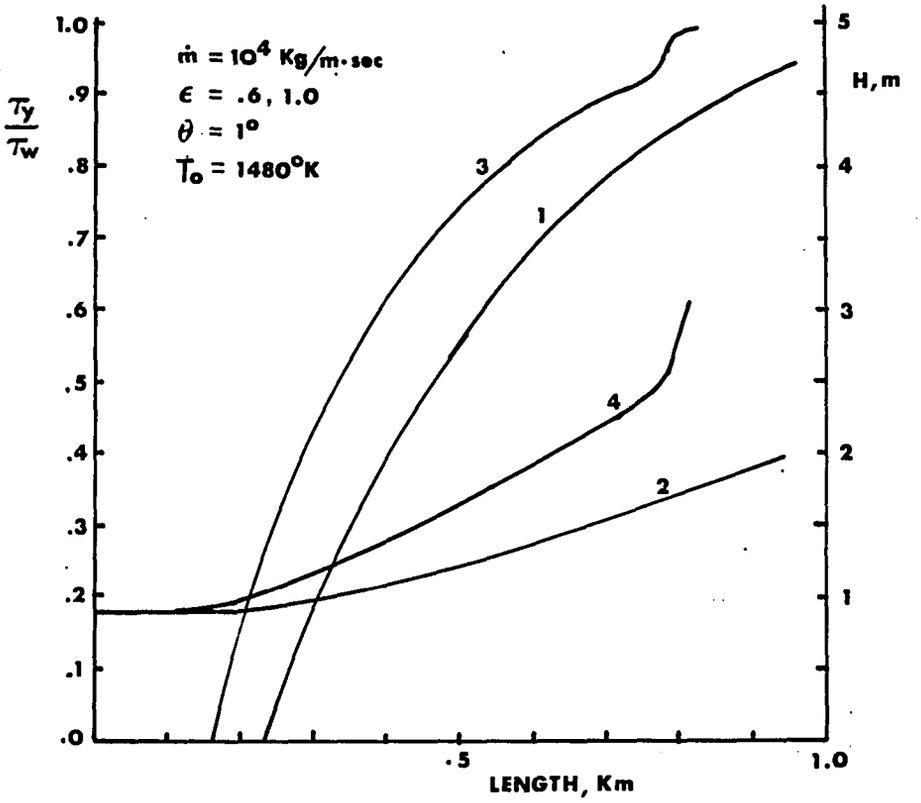

1. τ_y/τ_W ; use left scale
2. Thickness (h); use right scale

} ϵ = 0.6

3. τ_y/τ_W ; use left scale
4. Thickness; use right scale

} ϵ = 1.0

* step size ΔX = 0.01 km

Fig. 3.24b Thickness and τ_y / τ_w vs. length

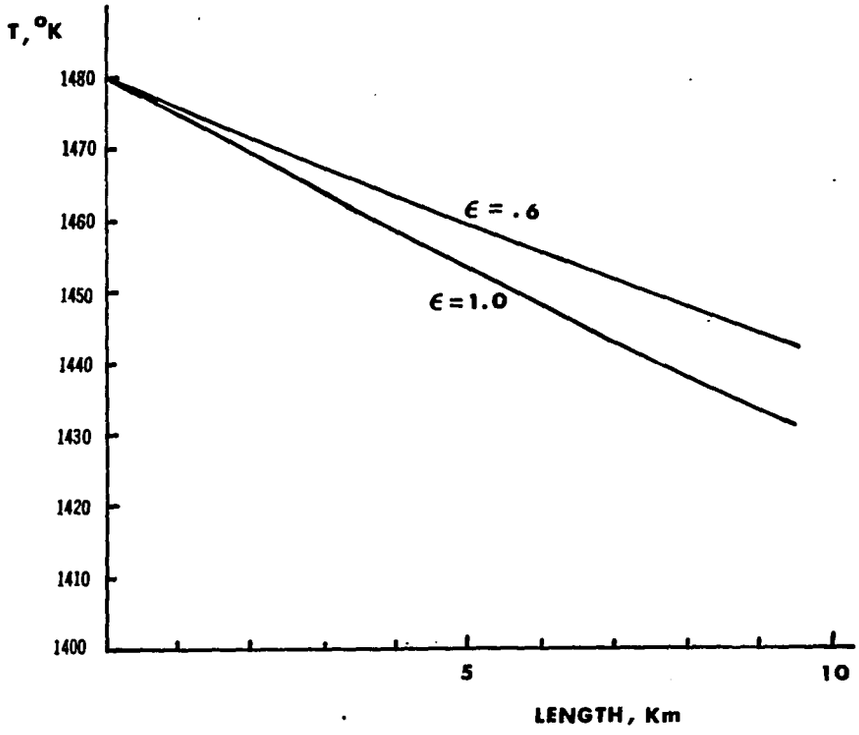

Fig. 3.25a Temperature vs. length for the case of Fig. 3.24a

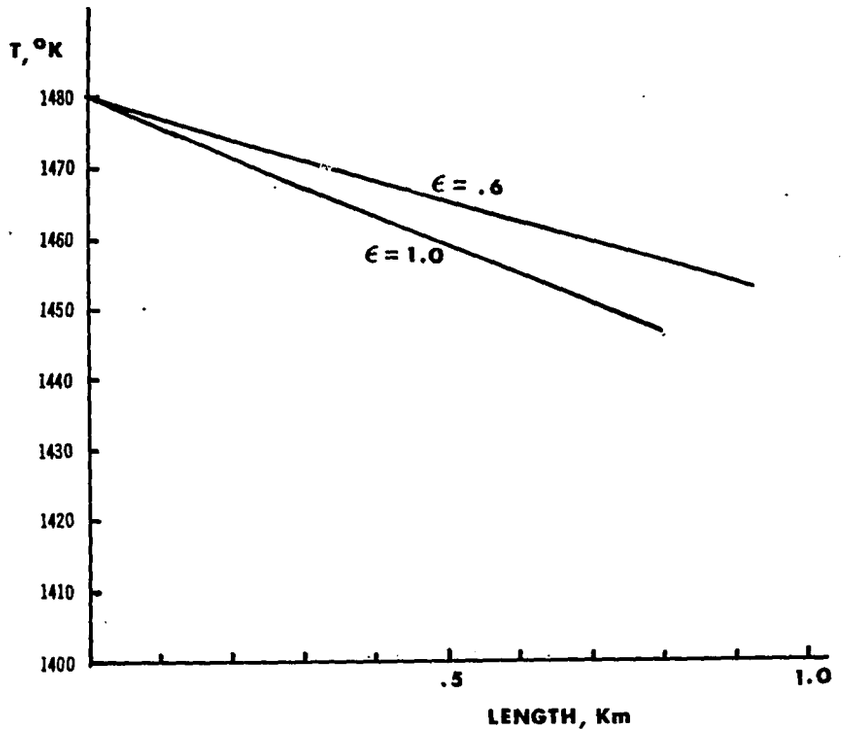

Fig. 3.25b Temperature vs. length for the case of Fig. 3.24b

IV. SIMILITUDE PROBLEMS

The ultimate goal of the physical simulation of lava flow is to understand the mechanism of flow via observations of laboratory flows. See the similarity of appearances between the flows of largely different scale (Fig. 4.1 and 4.2).

In this chapter, underlying principles of simulation and problems of lava flow simulation will be discussed.

A. Dimensional Analysis, π Theorem and Modeling

Very often, the problem to be tackled is so complex that it can hardly be formulated by a satisfactory mathematical model. In these cases, we have to rely heavily on experimental methods, to establish the essential physical features of the problem.

Many phenomena cannot be investigated directly, and therefore we have to perform experiments on similar phenomena which are easier to work out. These efforts are justified on the basis of dimensional analysis.

Dimensional analysis is based on two axioms that are inherent in our methods of measurement and evaluation of quantities. They are (41):

Axiom 1. Absolute numerical equality of quantities may exist only when the quantities are similar qualitatively.

Axiom 2. The ratio of the magnitudes of two like quantities is independent of the units in their measurement, provided that the same units are used for evaluating each.

Starting from these axioms, it can be shown that (42) a secondary quantity η, known to be determined by the values of certain, independent

primary quantities α, β, γ, will take the form

$$\eta = k\, \alpha^{n_1}\, \beta^{n_2}\, \gamma^{n_3} \tag{4.1}$$

where k is a constant.

The exponents n_1, n_2, n_3 can be positive or negative, integral or fractional.

If it is agreed to call α, β, γ, etc. primary quantities, then the exponents n_1, n_2, n_3, ... are, by definition, the dimensions of the secondary quantity η.

Usually mass, length and time (or force, length, time) are used as primary quantities in mechanical systems.

If the form of an equation does not depend on the fundamental units of measurement, the equation is called dimensionally homogeneous.

It can be proven (42) that, again based on the two axioms stated above, a dimensionally homogeneous equation can be reduced to a relationship among a complete set of dimensionless products.

That is,

$$\pi_1 = f(\pi_2, \pi_3, \ldots) \tag{4.2}$$

where π's are the dimensionless products made out of the physical variables in the way of Eq.(4.1).

The number of π terms, expressed rigorously, is equal to the total number of variables minus the maximum number of variables that do not form a dimensionless product (43). That is,

$$s = n-b \tag{4.3}$$

where s is the number of π terms, n is the total number of variables involved, and b is the number of basic dimensions.

Fig. 4.1 Small "spatter cone" vent of mud volcano about 20 centimeters high with extrusion of mud flow at Pocket Basin, Lower Basin, Yellowstone National Park, WY (Ref. 2, plate 191B)

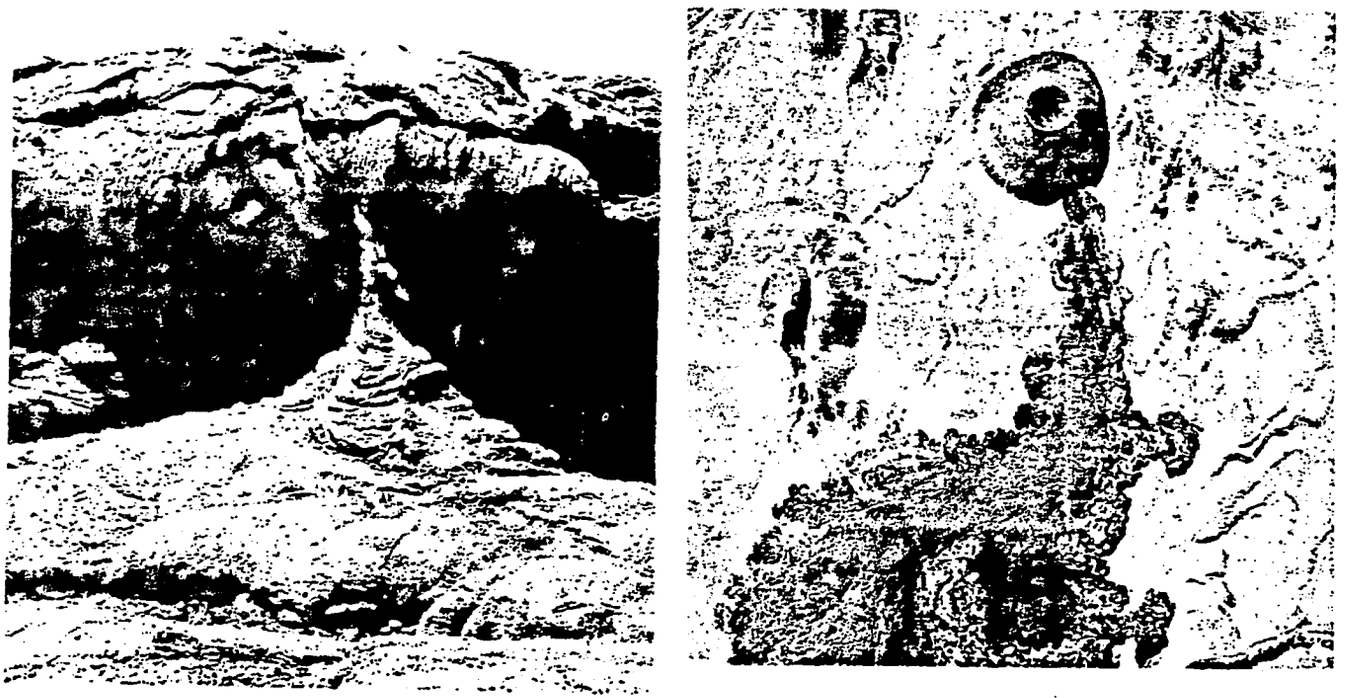

a b

Fig. 4.2a Pahoehoe lava

Fig. 4.2b A cinder cone (approximately 0.5 km in diameter) with basaltic lava spreading from its base. San Francisco Mountains area, Coconino County, AZ (Ref. 1:40,41)

The theorems stated in Eq.(4.2) and (4.3) are attributed to Buckingham.

Systematic determination of π terms can be found in standard textbooks on dimensional analysis (41, 44, 45). However, we will lean heavily on the method of determination by inspection in this study.

For clear presentation of the analysis, an example problem is discussed below. (This example was taken from Sedov (46):)

Suppose that the period of a simple pendulum is not known analytically, so we are trying to determine it by experimental procedures.

Let the period of pendulum T be of the functional form,

$$T = f(m, \ell, g, \phi)$$

where m is the mass of the pendulum, ℓ is the length of the pendulum, ϕ is the amplitude (initial) of oscillation measured in radians, and g is gravitational acceleration.

We will try to form π terms from the variables listed.

Dimensions of each of the variables are,

$T = [T]$

$m = [M]$

$\ell = [L]$

$g = [LT^{-2}]$

ϕ = dimensionless

It can be seen immediately that mass cannot form any dimensionless product with any other variable, so we take it out. Then we have four variables in two basic dimensions (L, T).

Hence, the π terms would be,

$$\pi_1 = T/\sqrt{\ell/g}$$

$$\pi_2 = \phi$$

Therefore,

$$T/\sqrt{\ell/g} = f'(\phi)$$

Now the period of T would not change whether the motion starts from ϕ or $-\phi$. That is, $f'(\phi)$ is an even function. Hence,

$$f'(\phi) = C_o + C_2\phi^2 + C_4\phi^4 + \ldots$$

If ϕ is very small,

$$f'(\phi) \cong C_o.$$

Finally, $$T/\sqrt{\ell/g} = C_o.$$

Without the aid of dimensional analysis, we would have had to go through a long series of experiments (or use Newton's laws of motion) to be able to predict the period of a pendulum (for various values of ℓ, ϕ, and m).

But with the use of dimensional analysis, if the measurement is precise enough, all we need is just one experiment to calculate C_o.

As can be realized from this example, dimensional analysis allows considerable economy of experimental efforts.

Now, let us turn our attention to the problem of modeling.

Quite commonly, direct experiment with the system we want to investigate (prototype) is physically or economically nearly impossible. In these cases, we usually employ a scale model similar to the system, and investigate the behavior of the model.

The similarity of the model to the prototype is established by the π theorem. Suppose that dimensional analysis of the system to be investigated leads us to the form,

$$\pi_1 = f(\pi_2, \pi_3, \ldots, \pi_n).$$

Let the π terms of the prototype be written as π_{1p}, π_{2p}, ..., and those of the model π_{1m}, π_{2m}, ...

The model is called <u>completely similar</u> to the prototype if

$$\begin{aligned} \pi_{1p} &= \pi_{1m} \\ \pi_{2p} &= \pi_{2m} \\ &\vdots \\ \pi_{np} &= \pi_{nm} \end{aligned} \tag{4.4}$$

If the model is completely similar, then the behavior of the model accurately predicts the behavior of the prototype.

However, it is usually not feasible to impose complete similarity in a model test. Therefore, it is necessary for the operator of the experiment to investigate the relative importance of the π terms, so that those π terms which are of secondary importance can be allowed to be distorted.

If the effects of some π terms are known a priori, then it is better that those terms be distorted, since the effect of distortion can be evaluated in this case.

If distortions are accounted for properly, then the behavior of the prototype can be adequately predicted by the behavior of the model.

B. Physical Variables and π terms for Lava Flow

There have been several experimental attempts to simulate lava flows. In this section, physical variables and π terms determined from those variables will be listed, mainly based on previous efforts of Hodgson (47) and Womer et al.(48).

The variables are:

fluid density (ρ)

gravitational acceleration (g)

fluid velocity (v)

characteristic horizontal length (L)

characteristic vertical length (H)

all other horizontal lengths (ℓ_i)

all other vertical lengths (h_i)

viscosity (μ)

yield strength (τ_y)

surface tension (σ)

specific heat (C_p)

thermal conductivity (k)

temperature (T)

temperature difference (ΔT)

heat transfer coefficient (h_t)

heat of fusion (Q_F)

pressure (p)

time (t)

More variables can be added to the above list. However, we will restrict our attention to the variables listed above.

From the variables above, we can form dimensionless numbers (π terms), most of which are familiar in fluid dynamics and heat transfer. These are tabulated in Table 4.1.

Other dimensionless numbers can be formed by combinations of these π numbers.

Table 4.1 Dimensionless numbers formed from the variables listed in the text (Ref. 48)

Vertical Geometric Scaling	h_i / H
Horizontal Geometric Scaling	ℓ_i / L
Reynolds No.	$\rho v H / \mu$
Froude No.	v^2 / gH
Weber No.	$\rho v^2 H / \sigma$
Eckert No.	$v^2 / C_p T$
Prandtl No.	$\mu C_p / k$
Grashof No.	$\rho^2 g \Delta T H^2 / T \mu^2$
Nusselt No.	Hh_t / k
Euler No.	$p / \rho v^2$
Bingham No.	$\tau_y H / \mu U$
Fusion No.	$Q_F / C_p T$
Temperature Ratio	$\Delta T / T$
Dimensionless Time	tv / L, $t^2 g / L$, $t\mu / \rho L^2$, or $tk / \rho C_p H^2$

For example,

Peclet No. = Reynolds No. x Prandtl No.;

Capillary No. = Weber Number / Froude No.

(The importance of the Capillary No. has been realized in § B.4, chapter III, for a small rivulet flow.)

However, the numbers formed by combination of others are not inde-

pendent. Thus, in order to assure the independence of π terms, the derived number should not be included without taking out one of the corresponding numbers which were combined. For example, Weber and Capillary No. should not be included in the same list (unless Froude No. is omitted).

Some of the 14 numbers listed can be disregarded due to physical reasoning.

Radiation and conduction dominate the heat transfer mode for lava flows (11, 19), hence we can omit the Nusselt No. (However, if we intend to use a heat transfer coefficient that includes radiation, that is, (49),

$$h_r = \varepsilon\sigma(T^2 + T_f^2)(T + T_f)$$

where T_f denotes the enclosure temperature, then this should not be discarded.)

For a free surface flow, pressure gradient may not be important, since movement of the flow is mainly due to gravity. Thus, Euler No. can be discarded.

Buoyancy may not be important, unless we focus our attention on the settling of rocks or the rise of volatiles during the flow. So Grashof No. can be taken out.

In lava flows, thermal energy is much greater than kinetic energy, so Eckert No. can also be disregarded.

Except for very small scale features, surface tension may be ignored. It is known that the surface tension will not be important provided $\rho g R^2 \cos\theta / 2\sigma >> 1$ (50:107), where R denotes the radius (or half-width) of the channel.

Even though we can remove these five numbers there still remain 9 numbers to be considered. This large number of π terms requires a great

deal of work and time to give proper and meaningful evaluations regarding the flow morphology.

For reference purposes, typical magnitudes of the π terms in Table 4.1 are given (on certain carbowax runs) in Table 4.2 and 4.3.

From these figures in Table 4.2 and 4.3, it is quite likely that the model will be distorted, even if we do not take into consideration the fact that π terms do vary during the flow process. If that variation is considered, the work becomes much more difficult.

So, in the following section, we attempt to find another approach.

C. Suggestion of Pseudo-similarity

If we perform our experiments based on the set of similarity terms in Table 4.1, other difficulties of operation (and interpretation) may arise in addition to those caused by the large number of π terms.

First, in this case velocity is a dependent variable; this differs from cases of forced flow where velocity is an independent variable. (For example, in incompressible aerodynamics, drag coefficient, C_D, is a function of Reynolds No., i.e. $C_D = f(Re)$.)

Since the velocity varies during the flow emplacement, a way of obtaining typical velocity has to be found.

Second, if some suitable way of defining characteristic length scale is not provided, the length scale may lead to ambiguity of scaling laws.

Thus, in this study, another simple type of similarity law will be derived using the analytical results obtained in Chapter III, and will be used as a possible way of approach to the present problem rather than using the set of Table 4.1.

Table 4.2 Magnitudes of various variables (Ref. 48)

	Lunar Lava	Terrestrial Basic Lava	Carbowax 4000
L	1000 cm	2500 cm	.25 cm
V_{min}	50 cm sec^{-1}	10 cm sec^{-L}	.3 cm sec^{-1}
V_{max}	400 cm sec^{-1}	400 cm sec^{-1}	.3 cm sec^{-1}
ρ	3.0 g cm^{-3}	2.0 g cm^{-3}	1.07 g cm^{-3}
C_p	.2128 cal g^{-1} $^{\circ}c^{-1}$	.20 cal g^{-1} $^{\circ}c^{-1}$	0.55 cal g^{-1} $^{\circ}c^{-1}$
k	1.5×10^{-3} cal $cm^{-1}sec^{-1}$ $^{\circ}c^{-1}$	7.0×10^{-3} cal $cm^{-1}sec^{-1}$ $^{\circ}c^{-1}$	0.8×10^{-3} cal $cm^{-1}sec^{-1}$ $^{\circ}c^{-1}$
Q_F	~100 cal g^{-1}	~200 cal g^{-1}	43 cal g^{-1}
d	300 d cm^{-1}	300 d cm^{-1}	65 d cm^{-1}
μ	50 to 1000 poise	~100 poise	~1 poise
l	1000 m	1000 m	1 cm
H	5000 m	5000 m	5 cm
h	10 m	25 m	0.05 cm
g	167 cm sec^{-2}	980 cm sec^{-2}	980 cm sec^{-2}
T	1473 °K	1473 °K	373 °K
ΔT	1200 °K	1200 °K	100 °K

Table 4.3 Magnitudes of various dimensionless numbers (Ref. 48)

	Lunar Flows	Terrestrial Basic Flows	Carbowax 4000 [a]
Width Ratio (1/L)	0.20	0.20	0.20
Depth Ratio (h/H)	0.002	0.005	0.01
Reynolds Number (VL^*/γ)	5×10^1 to 8×10^3	2.5×10^1 to 1×10^3	7×10^{-2}
Froude Number (V^2/L^*g)	1.5×10^{-2} to 9.9×10^{-1}	4.1×10^{-5} to 6.5×10^{-2}	4×10^{-3}
Weber Number ($\rho V^2 L^*/\sigma$)	2.5×10^4 to 1.6×10^6	1.7×10^3 to 2.7×10^6	4×10^{-4}
Nusselt Number ($h_c L^*/k$)	$6.7 \times 10^5 (h_c)$	$3.6 \times 10^5 (h_c)$	$6 \times 10^3 (h_c)$
Prandtl Number ($\rho\gamma C_p/k$)	2.1×10^4 to 4.3×10^5	5.7×10^4	7×10^2
Eckert Number (V^2/C_pT)	8×10^{-4} to 5.1×10^{-2}	3.2×10^{-5} to 5.4×10^{-2}	3×10^{-7}
Fusion Number (Q_F/C_pT)	0.3	0.7	0.2
Temperature Difference ($\Delta T/T$)	0.8	0.8	0.2
Grashof Number ($g\Delta TL^{*3}/T\gamma^2$)	5.4×10^7 to 1.4×10^5	1.2×10^7	4.1×10^2
Peclet Number ($\rho C_p VL^*/k$)	2.1×10^7 to 1.7×10^8	1.4×10^6 to 5.7×10^7	5.5×10^1
Dimensionless Time (t^{2g}/L^*)	$1.7 \times 10^{-1} (t^2)$	$9.8 \times 10^{-1} (t^2)$	$(t^2) 3.9 \times 10^3$

[a] Carbowax 4000 values calculated assuming 5X vertical exaggeration on test model.

This does not mean that we abandon the set of dimensionless numbers. Rather, those variables will be recast in the viewpoint of analytical solutions developed in Chapter III to be combined effectively, so that laboratory efforts can be minimized and more proper physical interpretations can be given.

Now, let us look at the analytical results obtained earlier, which are listed in Table 4.4.

Table 4.4 Similarity laws for steady, isothermal flow down an inclined plane[a]

Flow type	Similarity law	
Newtonian, Channel Flow	$\frac{Q\mu}{\rho g \sin\theta h^3 W} = f(\lambda)$	Section B.2.a, Chapter III
Bingham Plastic Channel Flow	$\frac{Q\mu}{\rho g \sin\theta h^3 W} = f(\lambda, \frac{\tau_y}{\tau_W})$	Section B.2.b, Chapter III
Newtonian, Small Rivulet	$\frac{Q\mu}{\rho g \sin\theta W^4} = f(\alpha)$	Section B.4.a, Chapter III
Newtonian, Wide (Flat) Rivulet	$\frac{Q\mu}{\rho g \sin\theta W h^3} = \frac{1}{3}$	Section B.4.a, Chapter III

[a] λ = aspect ratio W/h ; α = contact angle.

From the Table 4.4, we see that the similarity law for isothermal Bingham plastic flow is

$$\frac{Q\mu}{\rho g \sin\theta h^3 W} = f(\lambda, \frac{\tau_y}{\tau_W}) \qquad (4.5)$$

This can be viewed, in terms of the dimensionless numbers listed in

Table 4.1 as follows.

Firstly, consider the term $\frac{Q\mu}{\rho g \sin\theta h^3 W}$. Using $Q \sim Uhw$,

$$\frac{Q\mu}{\rho g \sin\theta h^3 W} \sim \frac{\mu U}{\rho g \sin\theta h^2} = \frac{u^2}{gh} \cdot \frac{\mu}{\rho U h} \cdot \frac{1}{\sin\theta} .$$

Thus, this term is, in fact, a combination of Froude No., Reynolds No., and one of the geometric scales, namely the slope, $\sin\theta$.

Secondly, the stress ratio τ_y / τ_w can be viewed as Bingham No. by the following reasons.

Approximately, $u \sim \rho g \sin\theta h^2/\mu$, which is rearranged as,

$$\rho g \sin\theta h \sim \frac{\mu u}{h}$$

Thus,

$$\frac{\tau_y}{\tau_w} = \frac{\tau_y}{\rho g \sin\theta h} \sim \frac{\tau_y h}{\mu U} .$$

Therefore, the similarity law of Eq.(4.5) is indeed a rational combination of dimensionless numbers of Table 4.1; Reynolds No., Froude No., Bingham No., and two geometric scales, i.e., aspect ratio and slope.

The numbers not included in the law, excluding thermal variables, are Weber No. and Euler No. Their omission was justified in the previous section.

However, we need some modification to the law to include non-isothermal effects which are obviously present in actual flow emplacement of lava.

For this purpose, let us consider the flow with single eruption of constant extrusion rate for a certain period of time (t_{ext} = extrusion

time). During the extrusion, the flow front will reach a certain distance (L_e), and after the extrusion ceases, the flow will drain down to travel further, attaining a final length (L_f). We exclude the cases of compound flows which develop several flow units.

The flow situation being considered is shown schematically in Fig. 4.3.

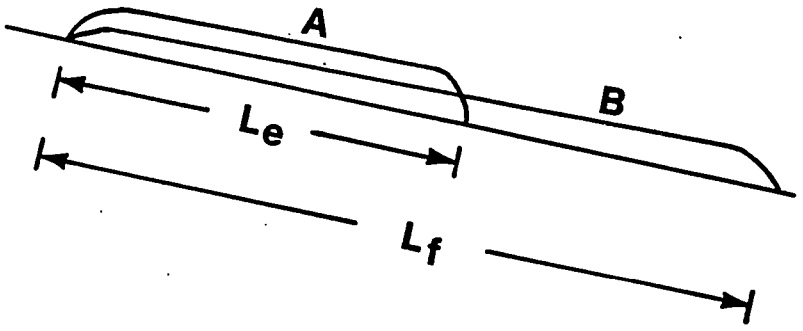

Fig. 4.3 Simplified model for a single flow unit with single eruption

Now, let the area covered by the flow during extrusion be A_e, and that covered finally be A_f.

We define the average flow depths (or thicknesses) as follows.

$$h_e = \text{Extruded volume}/A_e \tag{4.6a}$$

$$h_f = \text{Extruded volume}/A_f \tag{4.6b}$$

If we assume the width of the flow to remain fairly uniform, we have

$$\frac{h_f}{h_e} = \frac{A_e}{A_f} = \frac{L_e}{L_f} \tag{4.7}$$

Since the stopping of an isothermal flow is largely controlled by the presence of yield strength, we may set

$$\frac{h_f}{h_e} = g\left(\frac{\tau_y}{\tau_w}, \lambda\right) .$$

Hence, the similarity law of Eq.(4.5) can be formulated as

$$\frac{Q\mu}{\rho g \sin\theta h_e^3 W} = f_1\left(\lambda, \frac{h_f}{h_e}\right) \tag{4.8a}$$

By introducing the depth ratio $\frac{h_f}{h_e}$, the similarity law can be extended to non-isothermal flow cases, if cross-sectional profiles can be properly averaged. For this purpose, we employ an area averaging scheme for depths, i.e., Eq.(4.6a) and Eq.(4.6b).

Eq.(4.8a) can be written in other forms, such as

$$\frac{Q\mu}{\rho g \sin\theta W^4} = f_2\left(\lambda, \frac{h_f}{h_e}\right) \tag{4.8b}$$

or

$$\frac{Q\mu}{\rho g \sin\theta h_f^4} = f_3\left(\lambda, \frac{h_f}{h_e}\right) \tag{4.8c}$$

The final depth of the flow averaged over its area, h_f, is a measure of some property that will stop the flow. For example, h_f would be a reflection of yield strength for isothermal flow of Bingham material, and would be a measure of surface tension for a Newtonian fluid on a small scale flow unit.

Thus, for non-isothermal flow situations with given volume, extrusion rate, and width

$$\frac{h_f}{h_e} = f(\text{thermal variables including cooling rates}).$$

However, the similarity law suggested in the form of Eq.(4.8a), Eq. (4.8b) and Eq.(4.8c) does not explicitly include thermal properties. Therefore, this will be called a pseudo-similarity law.

One advantage of this law is that it largely utilizes geometric terms, which would be of great advantage in interpreting and simulating the lava flows on other planets, whose geometry we observe primarily on photographs.

Discussions of the results relevant to the law obtained from experiments with two different materials will follow in Chapter V.

V. EXPERIMENTS AND RESULTS

A. Scope of the Present Experiments

Actual observations of lava flows are difficult to make, and the opportunities for making them are quite rare. Accurate measurements of physical properties and quantities of real lava flows are even more difficult and expensive to obtain. It is therefore worthwhile to simulate such flows in the laboratory in a controlled manner.

The use of actual lava in the laboratory flow would be very expensive, if not impossible. Thus, we seek some other material that would behave in a similar manner and yet is easy to work with.

One such material that has been used by previous workers (47, 48) is Carbowax (polyethylene glycol compound). Carbowax 4000 and 1000 (grades refer to degree of polymerization) solidify at room temperature (melting point for 4000 is about 54°C, and that for 1000 is about 37°C). Thus, we expect that the mechanism of flow for carbowax extruded above 54°C would be at least qualitatively similar to that of lava.

Hulme (20) used Kaolin suspensions to test his model (see Chapter III, Sec. B.4.b). A Kaolin suspension doesn't exhibit cooling characteristics like those of lava, but it does have a distinct yield strength.

In this study, both carbowax 4000 and 1000 and Kaolin suspensions were used to study the basic flow down an inclined plane, with constant extrusion rates and fixed size circular vent.

No attempt has been made to simulate any specific geologic event.

The present experiments are primarily focussed on determining the effect of viscosity, slope, and volume flow rate on the flow morphology.

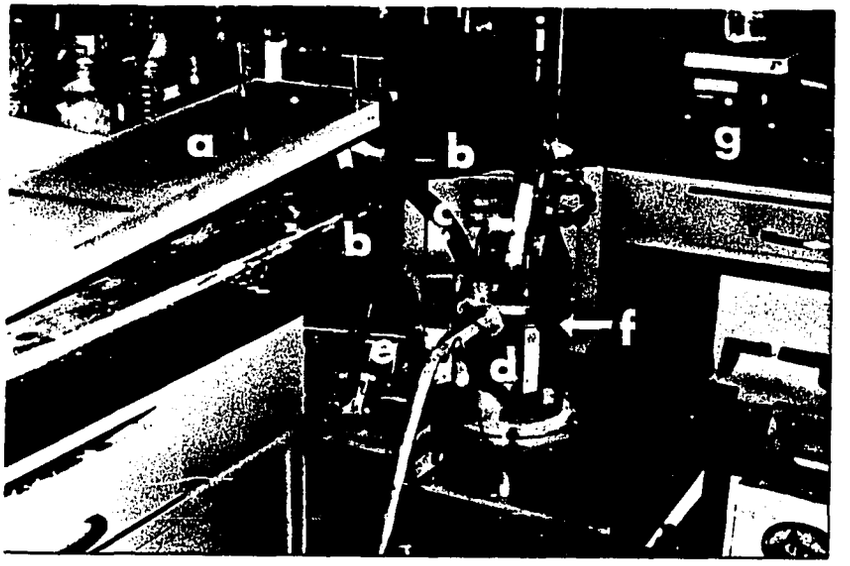

a. Plexiglass plate (9" x 45 ")

b. Recirculation tube (rubber, ½" ID)

c. Steam supply tube (rubber, ½" ID)

d. Piston and Cylinder (2-3/16" ID, 6" long)

e. Recirculating pump and motor

f. Heat bath (cylinder; 5-5/8" ID, 8" long)

g. Corning PC-35 hot plate

Fig. 5.1 Experimental set-up

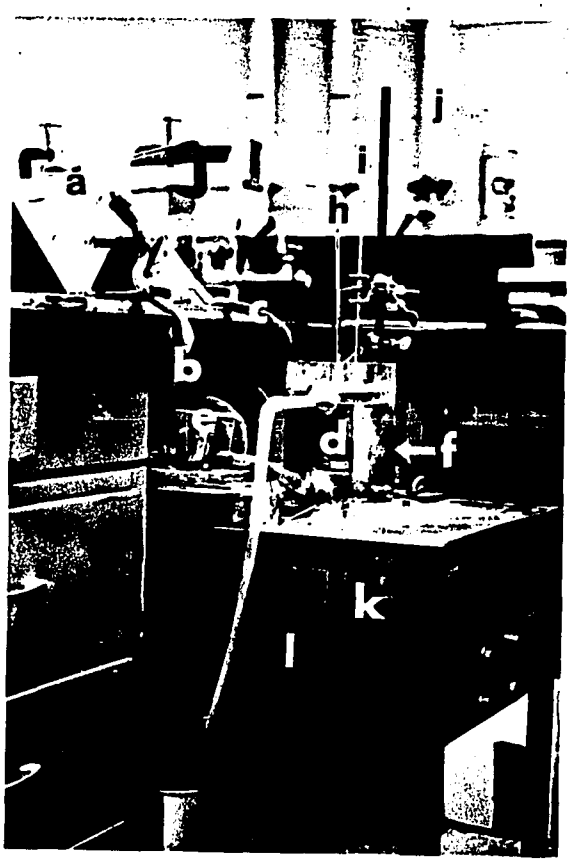

h. Thermometer (Fisher Scientific) for wax temperature

i. Thermometer (Fisher Scientific) for heat bath water temperature

j. Steam supply line

k. Piston axle (threaded)

1. Driving pulley

Fig. 5.1 (Cont.)

Most of the experiments were carried out with an extruder and sloping plate (plexiglass).

B. Experimental Apparatus and Procedure

The extruder (Fig. 5.1) was designed to give different extrusion rates and volumes using a piston-cylinder arrangement. (It was manufactured by E.R.I. Machine Shop, Iowa State University.)

Displacement and speed of displacement were controlled via a driving motor which was connected to the voltage transformer.

To ensure isothermal conditions up to the vent, hot water of known and controlled temperature was circulated from the heat bath (of water) to the conduit. Temperature of water in the heat bath was regulated by adjusting the input of steam around the bath.

Temperatures of Carbowax and the heat bath were both monitored using thermometers from Fisher Scientific.

Time of extrusion and time of flow were monitored with stopwatches.

The same extruder was used for both Carbowax and Kaolin-suspension.

Using the simple arrangements of extruder and sloping plate, the following series of experiments were carried out.

i) Series of Carbowax 4000 and 1000 flows (163 runs) for the following range of variables.

Q: $0.3 \sim 0.6$ cm^3/sec

θ: $3 \sim 12°$ (4000)

θ: $3 \sim 5°$ (1000)

T: $75 \sim 90°$C (4000)

T: $55 \sim 75°$C (1000)

Volumes: 25 cm^3, 50 cm^3.

ii) Series of Kaolin suspension flows (38 runs).

Q: 0.45 ∿ 0.67 cm^3/sec

τ_y: 16.0 ∿ 74 $dyne/cm^2$

μ: 2.6 ∿ 9.3 $dyne\text{-}sec/cm^2$

θ: 5 ∿ 20°

Volume: 25 cm^3

iii) Channelized flows of Carbowax 4000 and 1000 flows (13 runs).

Q: 0.54 ∿ 0.56 cm^3/sec

θ: 2.5 ∿ 3.5°

T: 60 - 80°C

Volume: 25 cm^3

iv) Channelized flows of Kaolin suspension (9 runs).

Q: 0.56 cm^3/sec

τ_y: 38, 82 $dyne/cm^2$

θ: 5 ∿ 20°

Channel width: 1 ∿ 2 cm

μ: 4.2, 12.7 $dyne\text{-}sec/cm^2$

Volume: 25 cm^3

v) Carbowax 4000 flows with heated plate (15 runs)

Q: 1.2 - 3.8 cm^3/sec

θ: 2.5 - 7°

T: 56 - 90°C

Volume: 35 - 100 cm^3

For Kaolin suspension, viscosity and yield strength were measured using a Brookfield synchrolectric L.V.F. type viscometer (Fig. 5.2).

Carbowax was first melted and heated to the desired temperature, then

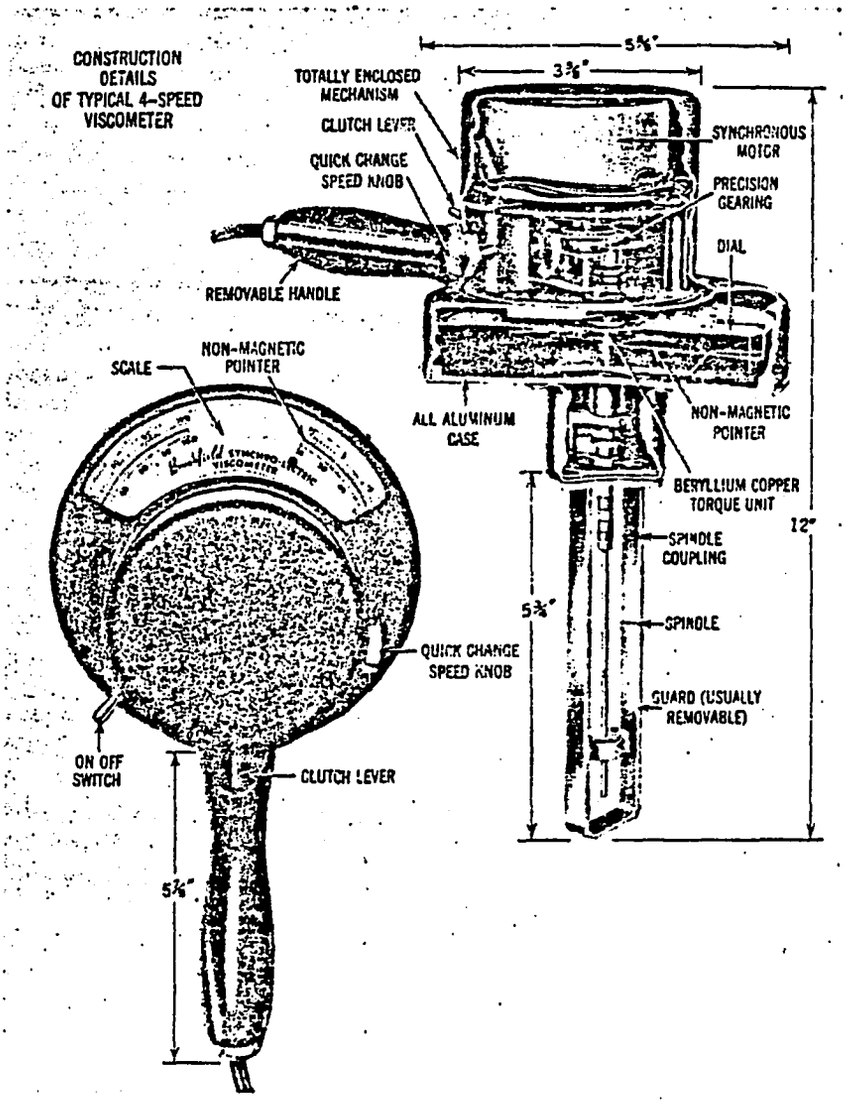

Fig. 5.2 Brookfield Synchro-Letric Viscometer

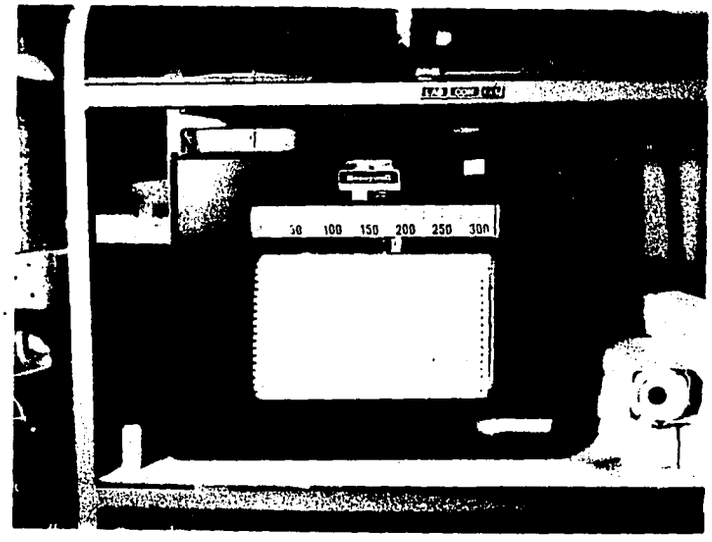

Fig. 5.3 Honeywell 5-Channel Recorder

poured into the cylinder which was preheated by the heat bath, and finally extruded onto the sloping plate of known angle.

For flows on the heated plate, the temperature of the plate and that of the Carbowax 4000 were monitored by C_r-Aℓ thermocouples attached to a 5-channel Honeywell recorder (Fig. 5.3) which was calibrated for these thermocouples.

For most Carbowax 4000 flows (sheet flows or rivulet flows), 2 or 3 runs were made under the same conditions to ensure repeatability.

Collected data appear in Appendix, sections A through E.

C. Experimental Results

Before discussing experimental results, definition of volume flow rate Q will be discussed to prevent possible confusion. Flow rate Q used in Chapter III is defined by

$$Q = u_{av} \cdot \text{cross-sectional area},$$

where u_{av} is the bulk velocity avareaged over the cross-sectional area. However, if we want to use Q defined above in the experiment, Q would be different station-by-station along the flow. To avoid this problem, Q will be used as extrusion rate, which is constant in the present study. If necessary, this will be denoted as Q_E, whereas the flow rate of the former definition will be denoted as Q_U. The difference between these two is shown schematically in Fig. 5.4 for a flow.

1. Results of Carbowax 4000 and 1000 flows (henceforth referred to as C-4000, C-1000)

In this section, results of C-4000 and C-1000 runs (rivulet flows or

sheet flows) will be discussed.

Viscosity and density variations with temperature are shown in Fig. 5.5 and Fig. 5.6.

Thermal conductivity of Carbowax can be calculated from the equation developed by Sheffy and Johnson cited by Thieling (51):

$$k = \frac{(4.66 \times 10^{-3})\ [1 - 0.00126(T - Tm)]}{(Tm^{0.216}\ M^{0.300})}$$

where T is the temperature in question in degrees Kelvin, Tm is the melting point in degrees Kelvin, M is molecular weight. Conductivity is expressed in cal/(cm)(sec)(°k). Molecular weight of C-4000 ranges from 3000 to 3700 and that of C-1000 ranges from 950 to 1050. Average liquid specific heat for C-4000 is 0.55 cal/g°C and that for C-1000 is 0.54 cal/g°C. (52)

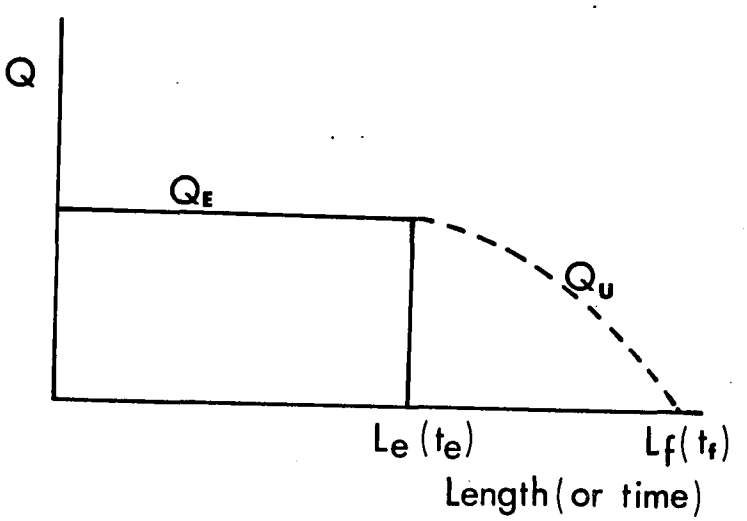

Fig. 5.4 Q_E and Q_u ; Q_E is approximately a step function, whereas Q_u is not

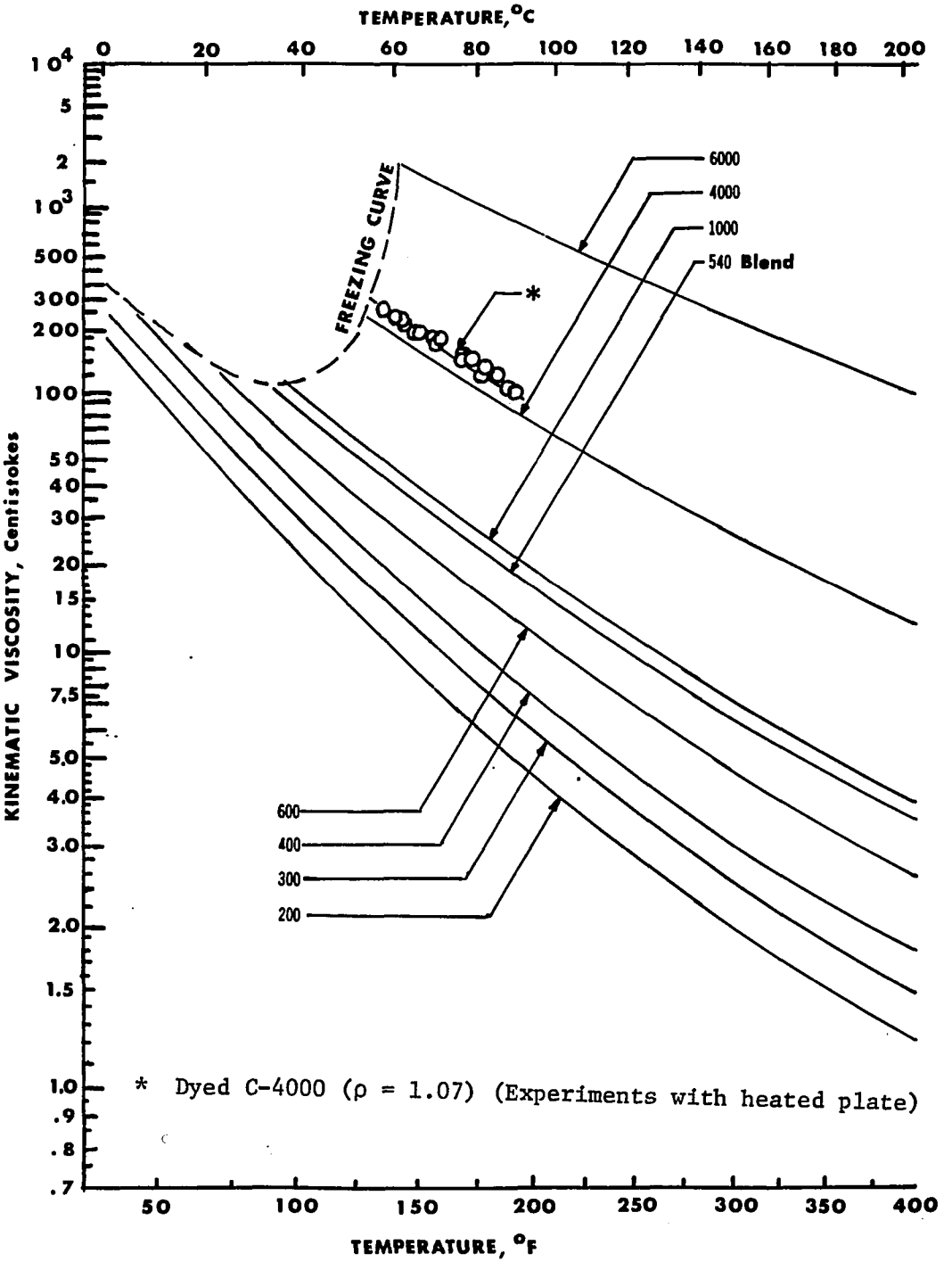

Fig. 5.5 Kinematic viscosity of polyethylene glycols (Ref. 52)

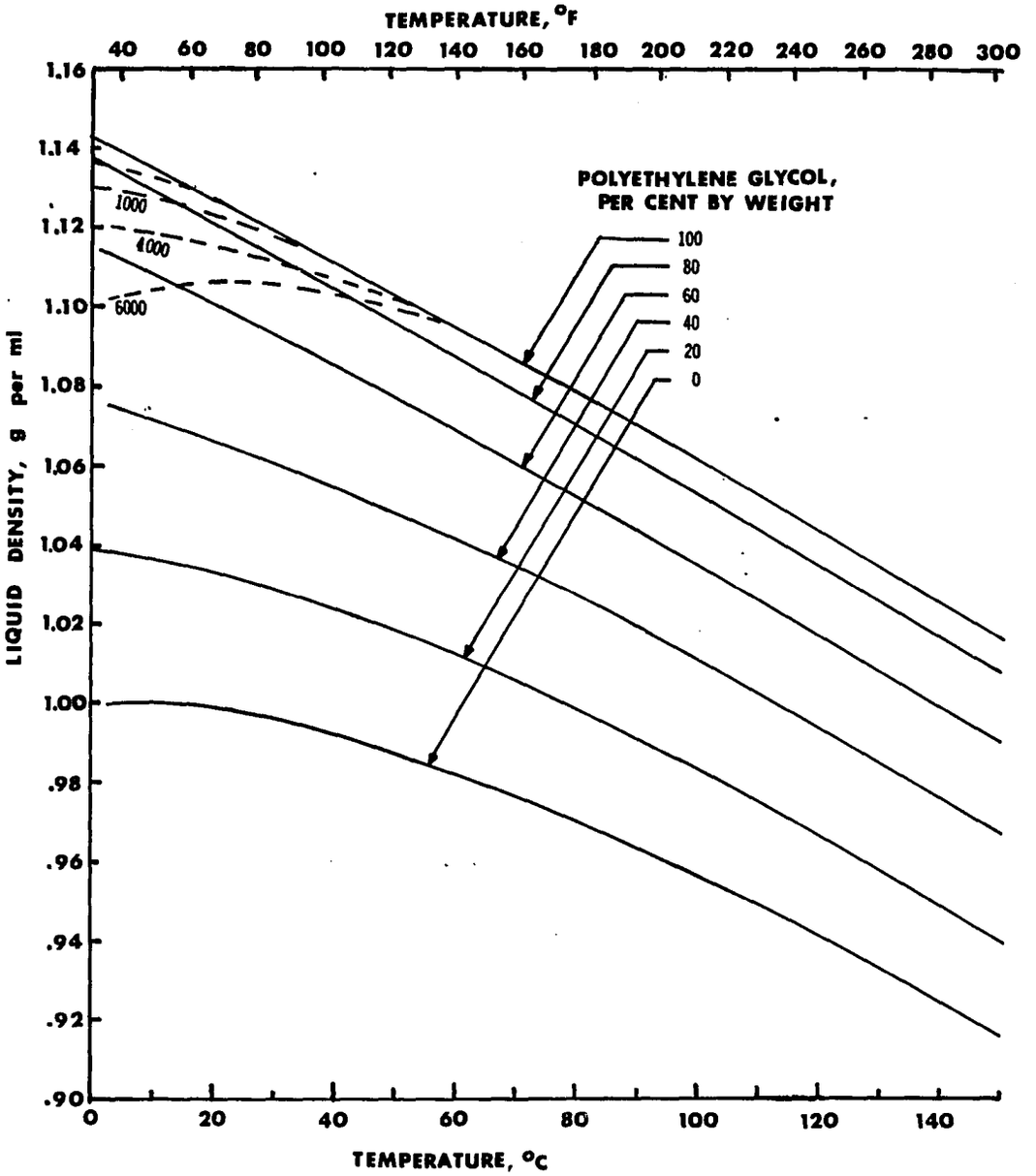

Fig. 5.6 Liquid densities of aqueous solutions of liquid and solid polyethylene glycols

a. Flow profile and emplacement Typical cross-sectional profiles of C-4000 flows are shown in Fig. 5.7. Apparently cooled levees developed near the vent and extended only to a certain distance (about 30 cm in the figure). Increase of flow thickness is evidently an indication of cooling.

The movement of the flow front became slower as the flow proceeded. (For example, about one minute was taken for the flow front to reach 40 cm (from the vent), whereas about three minutes was taken to reach 64 cm.)

C-4000 flows become narrower as drainage occurs, whereas C-1000 flows become slightly wider (or maintain the same width).

This may be due to the effect of cooling. Cooling rates may be approximately the same for both cases, since the external conditions are almost alike and conductivities of both materials are about the same magnitude. Because the fusion temperature of C-1000 is much lower (37°C) than that of C-4000 (54°C), cooling effects for the C-1000 flow would be relatively insignificant compared to those with C-4000 flows as long as the experiment is conducted under room temperature conditions.

Thus in the draining stage, the C-1000 flow will have a greater quantity of liquid that can drain effectively than the C-4000 flow. (Note the viscosity of C-1000 and that of C-4000 differ by an order of magnitude.)

Combined with the effect of surface tension (for normal liquid, surface tension increases as it cools), this will make the difference in width variation. (Of course, this will be true only for experimental conditions similar to the present study.)

Sequential photos of the emplacement of another flow are shown in Fig. 5.8. Note the relatively uniform width along the length.

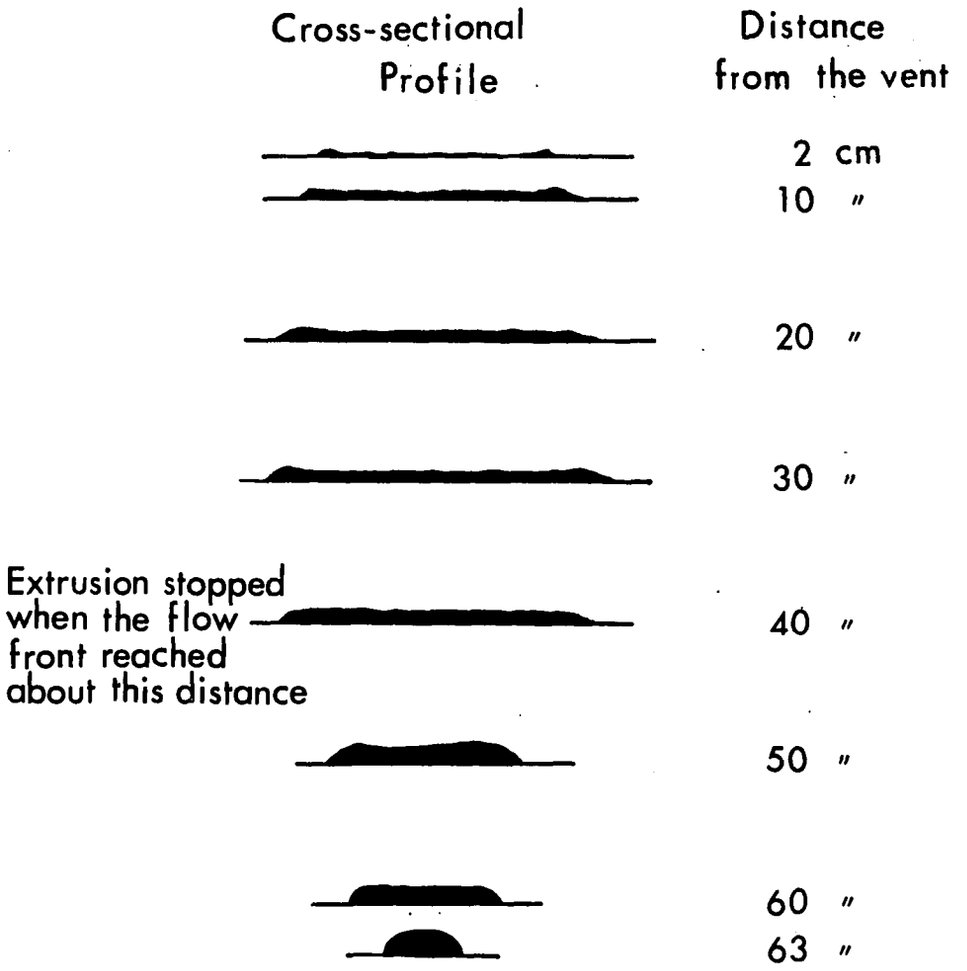

Material: Carbowax 4000

Initial Temperature: 80°C

Slope: 5°

Total Volume: 24.86 cm^3

Volume flow rate: 0.44 cm^3/sec.

Fig. 5.7 Typical cross-sectional profile of Carbowax 4000 flow

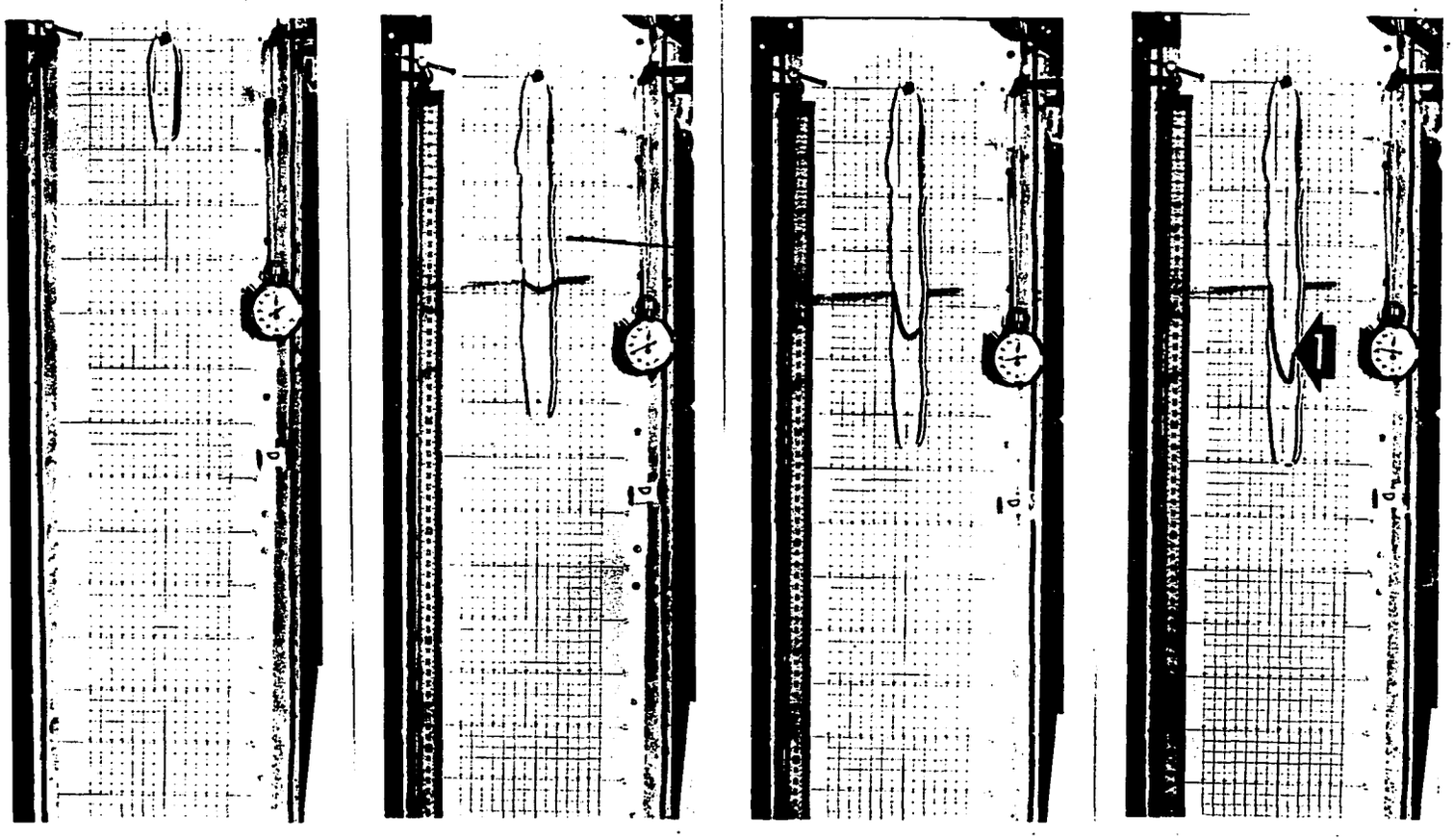

t = 10 sec.
(after starting of extrusion)

t = 40 sec.

t = 43 sec.

t = 47 sec.

Fig. 5.8 Sequential photos of a flow of Carbowax 4000

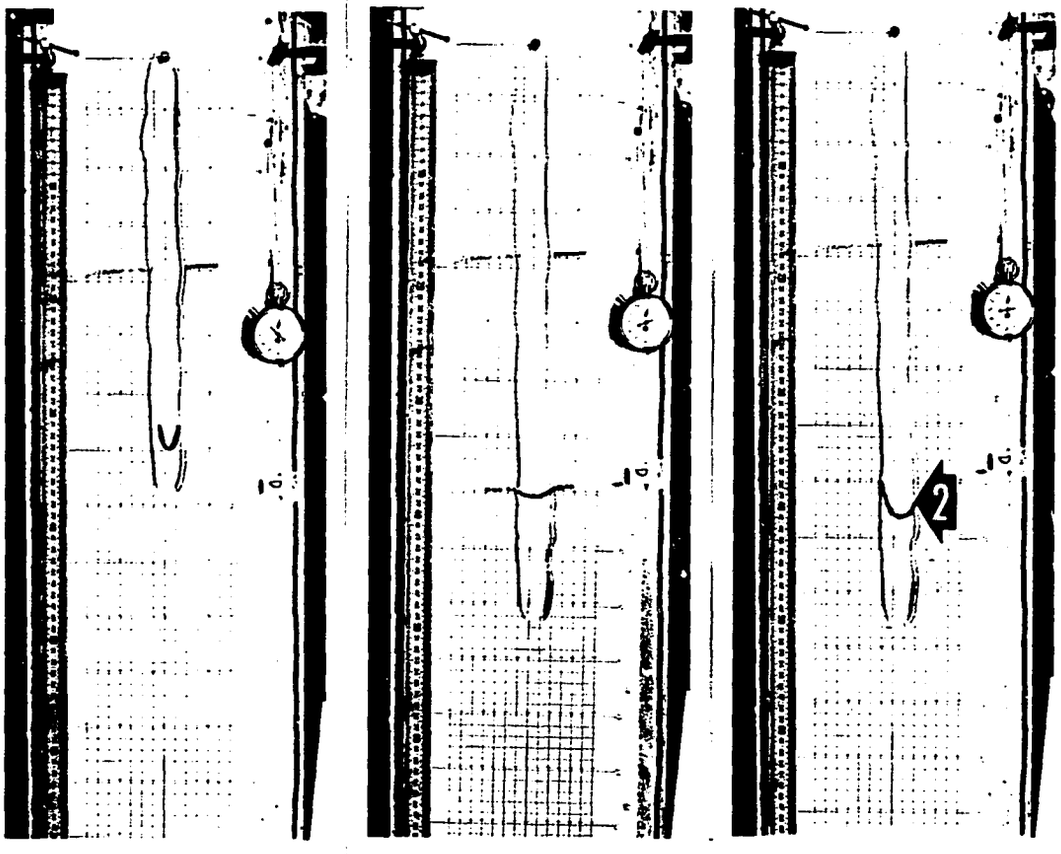

t = 52 sec. t = 71 sec. t = 74 sec.

Experimental Conditions

Vol.: 26.7 cm^3

Q: 0.47 cm^3/sec.

Extrusion Temperature: 80°C

Slope: 7°

t_{ext}: 57 sec.

Fig. 5.8 (Cont.)

In the flow of Fig. 5.7, width varied considerably with distance, whereas in the flow of Fig. 5.8, width varied very little. This difference in width variation mainly comes from the differences in slope.

Sawdust was placed on the flow to help visualize the velocity profile. Note the parabolic shape of the velocity profiles, as well as the two different velocity profiles (marked as Arrow 1 and Arrow 2), which suggest the downstream increase in viscosity.

b. Effect of μ, θ, Q and volume on length One fundamental way of investigating the dependency of one variable on another is to directly compare the measurement of one dependent variable with one independent variable while keeping all other independent variables constant.

Fig. 5.9 shows the effect of viscosity on length of the flow. The slope of the line on the figure is approximately -0.33. This suggests that length varies as

$$L \alpha \nu^{-0.33}$$

Justification for this exponent is as follows: for an isothermal case and for large aspect ratio flows, velocity u_{av} behaves as (Eq.3.13),

$$u_{av} \alpha \frac{\rho g \sin\theta h^2}{\mu}$$

and thickness varies as (Eq.3.12)

$$h \alpha \left(\frac{Q\mu}{\rho g \sin\theta W}\right)^{1/3}$$

Thus,

$$u_{av} \alpha \frac{(\rho g \sin\theta)^{1/3}(Q/W)^{2/3}}{\mu^{1/3}}$$

If values of Q/W have little variation, for fixed slope

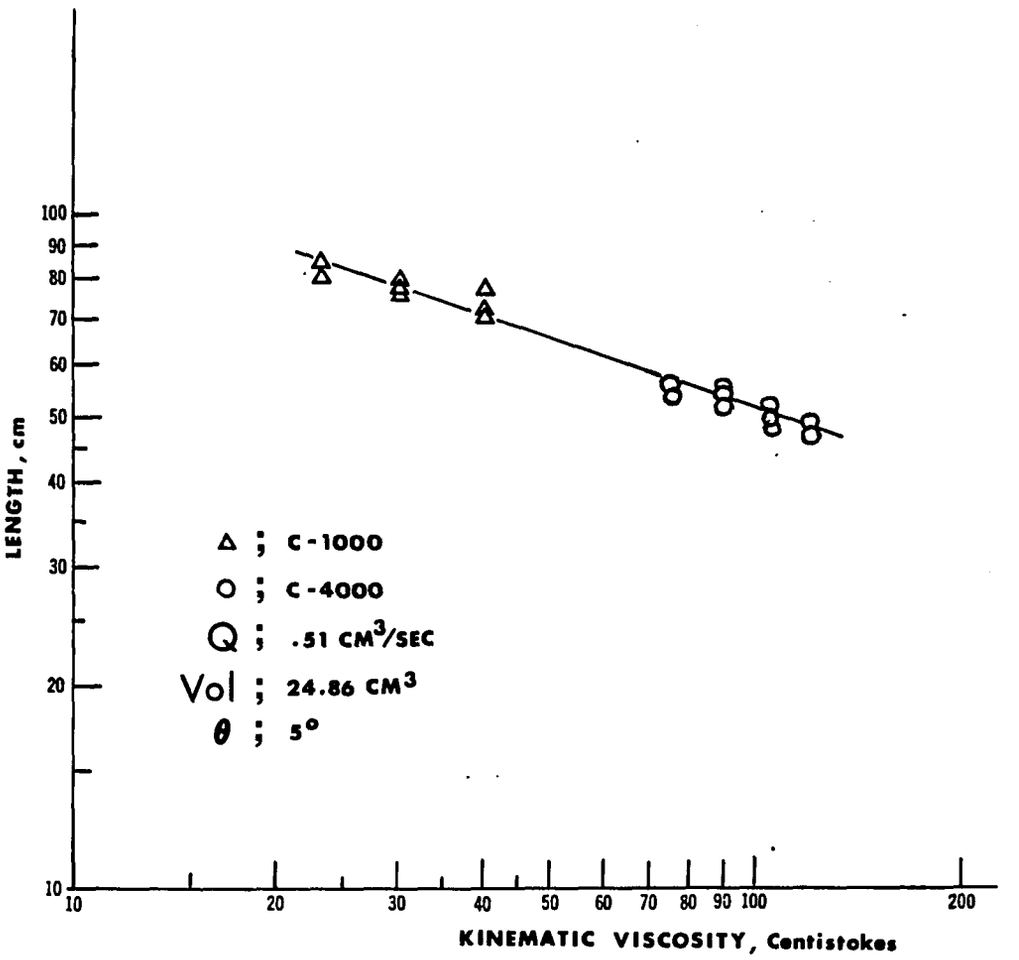

Fig. 5.9 Length versus kinematic viscosity for Carbowax flows

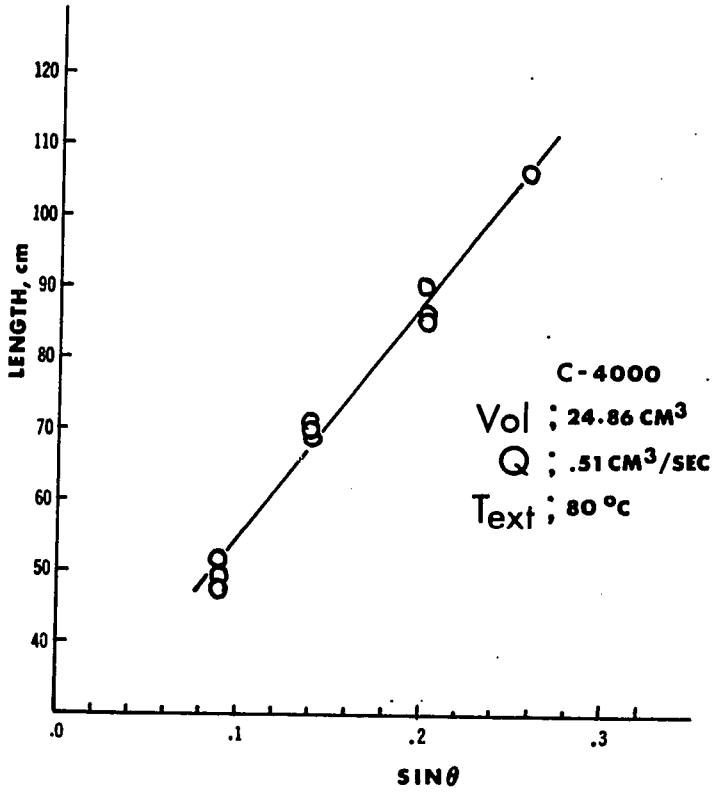

Fig. 5.10 Length vs. slope

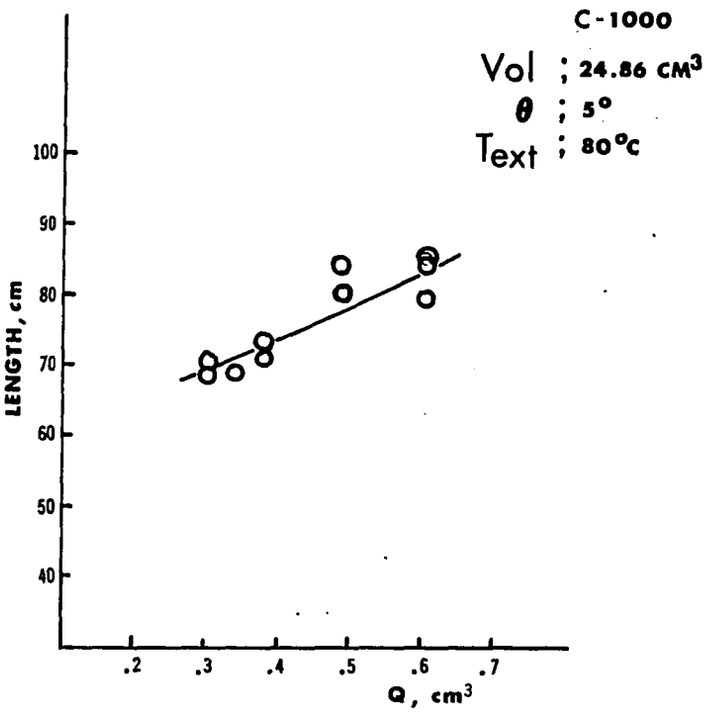

Fig. 5.11 Length vs. volume flow rate

$$u_{av} \propto \frac{1}{\mu^{1/3}}$$

Hence, length of extrusion may vary as

$$L_e \propto \frac{1}{\mu^{1/3}}$$

for fixed volume. (Since Q_E is held constant, extrusion times for these cases are the same.)

Since the cooling effects would be nearly alike for the flow conditions of Fig. 5.9, Eq.(5.1) suggests that the final length, L_f, behaves as

$$L_f \propto L_e \ .$$

The analyses made so far are based on isothermal, steady flow conditions. But this should not be regarded as justifying the use of the analytic equation for the overall flow, since only proportionality characteristic has been used for discussion. Note that Fig. 5.9 can also be interpreted as Temperature vs. length relation, since viscosity varies as temperature (see Fig. 5.5).

Fig. 5.10 shows the length dependency on slope. For fixed conditions, length varies in almost direct proportion to the slope.

Fig. 5.11 shows the effect of extrusion rate on length of the flow. Length increases as volume flow rate, as has been observed by Walker (8) on actual lava flows.

In Table 5.1, some flow data for two groups of C-4000 flows are tabulated. Since the conditions of operation are slightly different for the two different groups A and B except volumes we can see the length depend-

Table 5.1 Length data for some C-4000 flows

	Length(cm)	Vol.(cm^3)	Q_E(cm^3/sec)	Text(°C)	Slope(deg)
	76.9	49.7	0.46	86	5
A	74.7	49.7	0.46	86	5
	79.5	49.7	0.46	86	5
	51.2	24.9	0.51	85	5
B	53.8	24.9	0.51	85	5
	53.5	24.9	0.51	85	5

ency on volume, at least qualitatively.

Though it is not strictly correct to deduce quantitative relations from only two different sets of data, the proportionality obtained from the data above is (for comparison purposes)

$$\frac{L_2}{L_1} = \left(\frac{Vol_2}{Vol_1}\right)^{0.544}$$

Hodgson (46) reported the exponent (from his carbowax data) to be 0.382 ± 0.136.

Malin (9) correlated lengths and volumes for actual lava flows in Hawaii as

$$L \alpha (Vol.)^{\alpha}$$

and reported α to be 0.55 ± 0.03.

The agreement in exponents appears excellent, although it could be coincidental.

From the data of groups A and B, it can be seen that the repeatability of this experiment is reasonable.

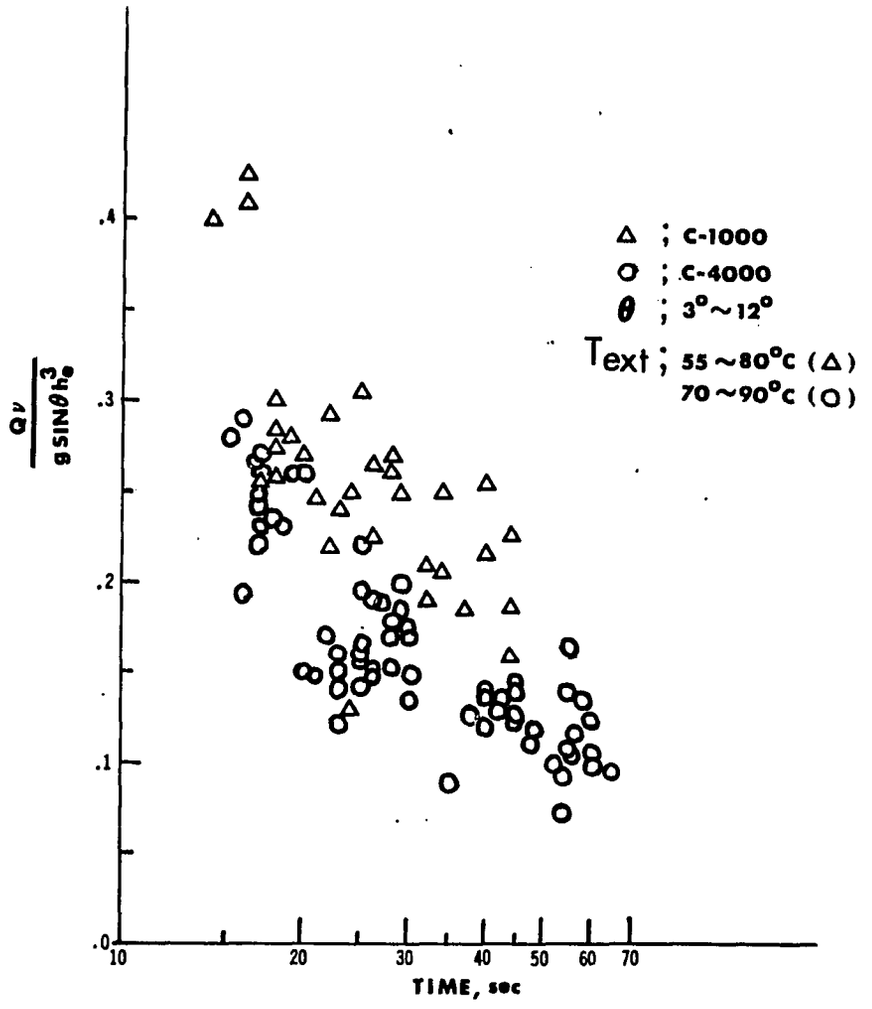

Fig. 5.12 $\frac{Q\nu}{g \sin\theta w h_e^3}$ vs. time taken for the flow front to reach a certain distance (23 cm)

c. Further discussion In Fig. 5.12, values of $\frac{Q\nu}{g \sin\theta W h_e^3}$ are plotted versus time taken by various flows to reach a certain distance ($< L_e$), 23 cm, from the vent.

For the calculation of h_e, the averaging scheme, Eq.(4.5a), was used. Width W was calculated by

$$W = \frac{\text{Area}}{\text{Length}} \quad .$$

For μ, viscosity at extrusion (Extrusion Temp., T_{ext}) was used. As can be seen clearly from the figure, the scatter of data points is wide, which may suggest the effect of cooling and unsteadiness of the flow. From the figure we can note the tendency for the values of $\frac{Q\nu}{g \sin\theta h_e^3 W}$ to decrease with time, that is they get smaller for slower flows.

Since initial viscosities were used for the calculations, for the slow flows, this viscosity must be lower than the actual (averaged) value.

An effective averaging scheme for viscosity or a suitable way of providing the proper distances (so that the measurements can be taken consistently), which may result in a better correlation, has not been found.

The scatter may also suggest the unsteadiness of the flow near the vent.

It is tempting to predict the location of flow front as a function of elapsed time referenced to starting of extrusion. Since the thermal properties are important in the cooling process, which is important in length development as discussed in Section B.7, Chapter III, we employ a time scale based on thermal properties.

That is,

$$t_{ref} = \frac{\rho C_p \ell^2}{k} \quad .$$

For length scale, ℓ, we choose the scale based on extrusion rate Q as

$$\ell_R = \left(\frac{Q \nu}{g \sin \theta W} \right)^{1/3}$$

which is the depth of 2-d flow, reflecting flow dynamics.

In Fig. 5.13, length traversed by the flow front vs. elapsed time is plotted for several different flows of various conditions except volume (volume is fixed).

By the arrangements of variables as in Fig. 5.13, the data collapsed roughly onto a single curve, but the effect of variable T/T_F can be noticed.

Decrease in slope of the curve marked by 'a' reflects some late stage of draining. In the figure, lengths and times were taken up to a somewhat earlier stage of draining (hence $Q \cong Q_E$), and do not include the data of the final stage of draining, where the motion is so sluggish.

For a specific flow, ℓ_R, t_{ref} and sin θ would be the same. Thus, if width varies only slightly, we have

$$L \alpha t^{0.75 \sim 0.8}$$

Inspired by the observation discussed above, least square regression was tried for the dimensionless number set h_f/ℓ_R , Pr, T/T_F , sin θ, t_{ext} / t_{ref} calculated from the data in Appendix, section A.

Pr is the Prandtl number, ℓ_R and t_{ref} are reference length and time scale as defined in the previous discussion.

The result is shown in Fig. 5.14. The temperature ratio, T/T_F, where T is the extrusion temperature, contributes strongly to the thickness ratio

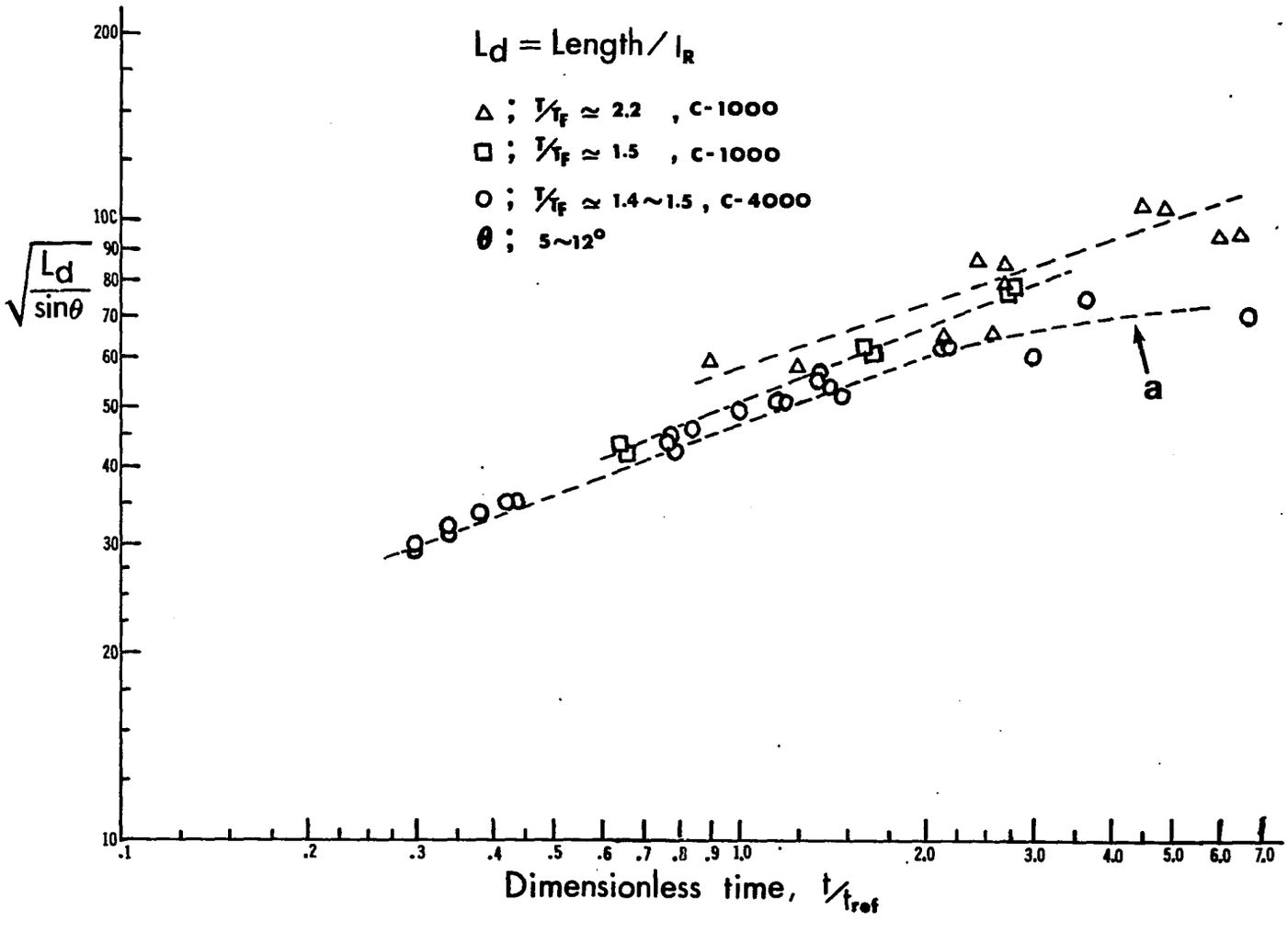

Fig. 5.13 Length vs. dimensionless time

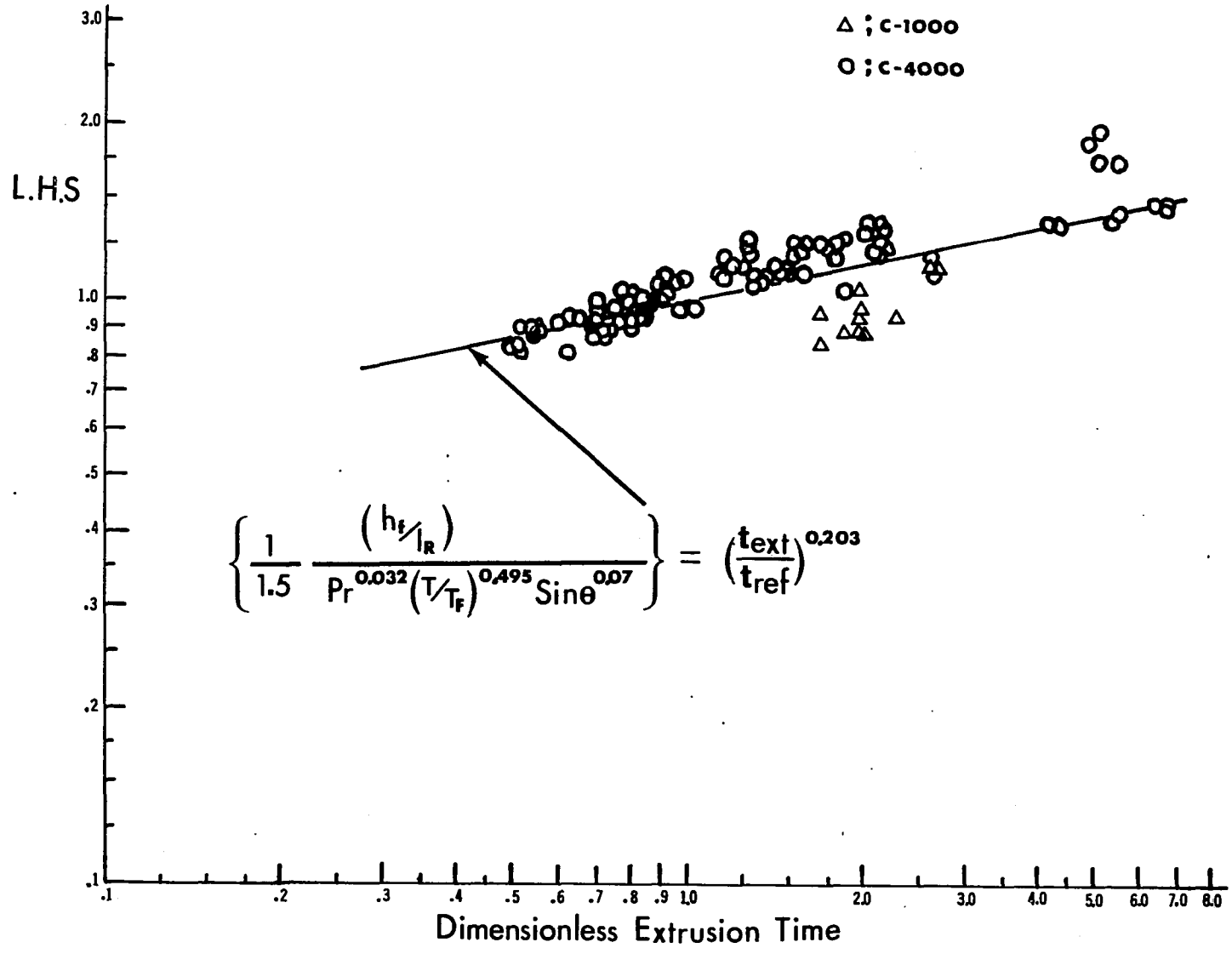

Fig. 5.14 Least square fit between various variables for Carbowax flows

h_f/ℓ_R.

Since ℓ_R can be interpreted as initial flow thickness, the above relation can be interpreted as follows.

If the extrusion temperature, T_{ext}, is slightly higher than fusion temperature, T_F, then the thickness of the final flow and initial flow thickness would be about the same, since $T_F/T \sim 1$. That is, the flow will cease as soon as extrusion ceases.

As T_{ext} increases, h_f/ℓ_R decreases, since the flow would have more (thermal) potential to drain out a further distance.

The weak dependence of the ratio on sin θ suggests that the slope may already be properly accounted for in the reference length scale, ℓ_R.

The weak dependence of the ratio on the Prandtl number may be due to the relatively small range of prandtl number ($4.7 \times 10^3 \sim 7.0 \times 10^3$ for C-4000 flows, and $0.8 \times 10^3 \sim 1.8 \times 10^3$ for C-1000 flows) or the effect may have been reflected already in temperature ratio T/T_F, since both conductivity and viscosity are temperature dependent. However, for the present it is not clear.

Several flows of Carbowax 4000 and 1000 were made on a sloping channel, but the comparison will be given later. The channel flows flowed much longer than sheet flows, hence the slope has to be restricted up to 3.5° even at relatively low extrusion temperatures under the same conditions of sheet flows.

2. Results of C-4000 flows on a sloping heated plate

The C-4000 and C-1000 flows discussed in previous sections did not produce surface textures similar to those of actual lava flows.

The differences probably came from the difference in cooling mechanism, and from scale effects.

In an actual lava flow, the main modes of cooling are radiation and conduction, with radiation slightly dominating conduction (11, 40). Furthermore, the flow is thick enough that the top portion may not feel the presence of the cold bottom during the course of flow.

In the experimental flows of C-4000 and C-1000, the main cooling mechanism is conduction to the bottom. Since the flow is thin, (final flow thickness ranges 0.5 $\sim$ 2mm) conductive heat loss dominates the whole thickness. This is clear if we consider the diffusion time scale, t_D.

$$t_D = \frac{\rho C_p h^2}{k}$$

Time scale for a C-4000 flow of thickness of order of a 'mm' is of the order of a minute, whereas that of a basalt flow of thickness of order of a 'm' is of order of a hundred hours.

Therefore, to obtain the similar surface textures in Carbowax flow, it is necessary to prevent conductive heat loss to the plate. An easy way of achieving this is to heat the plate. Fifteen flows were made using the arrangement shown in Fig. 5.15.

The data obtained and experimental conditions are in § B, Appendix.

One distinct difference is that, for the heated plate, the flow length is much longer than for the cold plate, as can be seen from Fig. 5.15.

However, the difference in length became smaller as the slope of the plate increased (for fixed heated plate temperature).

The expected surface textural differences were obtained and varied according to the temperature of the plate.

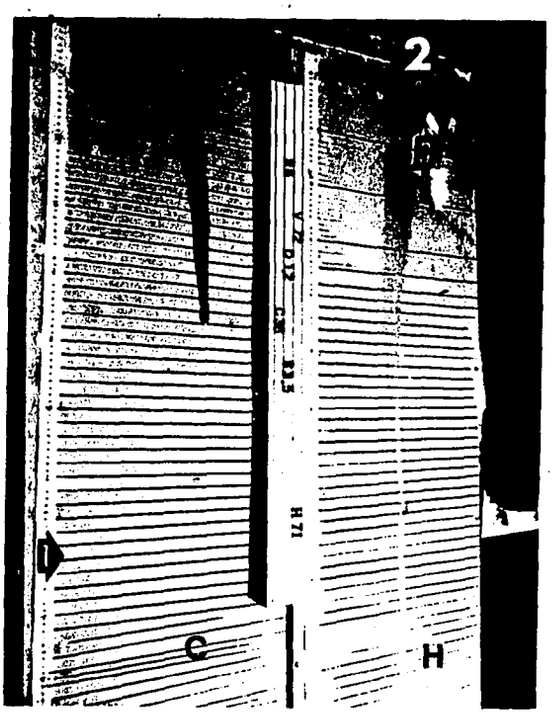

1: transite plate

2: densely wired (22 gauge wire) sheet for heat source

3: C_r - Al thermocouple for plate temperature

Fig. 5.15 Arrangements for heated plate flow and comparison of flow down a cold plate (c) and flow down a heated plate (H)

Typical surface textures of flow on cold plate and that of heated plate are compared in Fig. 5.16. More textural variations are shown in the next few pages.

3. Results of Kaolin-suspension flows

Mixing of small size solid particles (0-50 μm) with a Newtonian fluid approximately yields a Bingham plastic fluid.

For example, the following empirical equations can be used for estimation of yield strength and viscosity (50).

$$\tau_y = 312.5 \frac{\phi^3}{D_p^2} \qquad (5.1)$$

$$\mu = \mu_s \exp\left[\phi\left(\frac{5}{2} + \frac{14}{\sqrt{D_p}}\right)\right]$$

where τ_y is given in N/m^2, D_p in μm.
In the above equation, ϕ is volume fraction of solids, D_p is particle diameter, μ_s is viscosity of the Newtonian fluid in which the particles are suspended.

As has been mentioned earlier, Kaolin suspension was used for some of the experiments. To minimize settling during the experiment, Kaolin colloidal powder (Fisher Scientific) was chosen.

a. Measurement of viscosity and yield strength Instead of using equations (5.1), viscosity and yield strength were measured directly using a Brookfield Synchro-Lectric Viscometer (Fig. 5.2).

It was noted that the viscosity and yield strength for the Kaolin suspensions changed after a long time span (1 or 2 days); hence, measurements were taken before for almost every experiment.

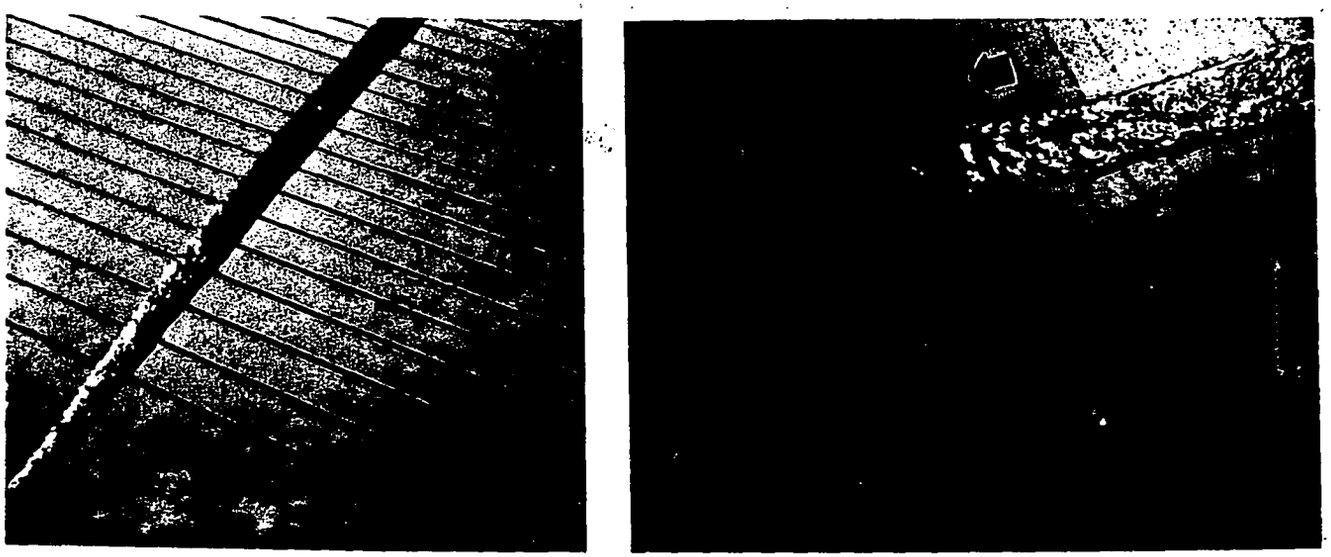

a b

a. Surface texture of a flow on cold (room temp.) plate

b. Surface texture of a flow on heated plate
(Taken from R 13-H; T_{ext} = 81°C, θ = 5°, Q = 1.15 cc/sec., T_{plate} = 44°C, Vol. = 51.6 cc)

Fig. 5.16 Comparison of surface textures

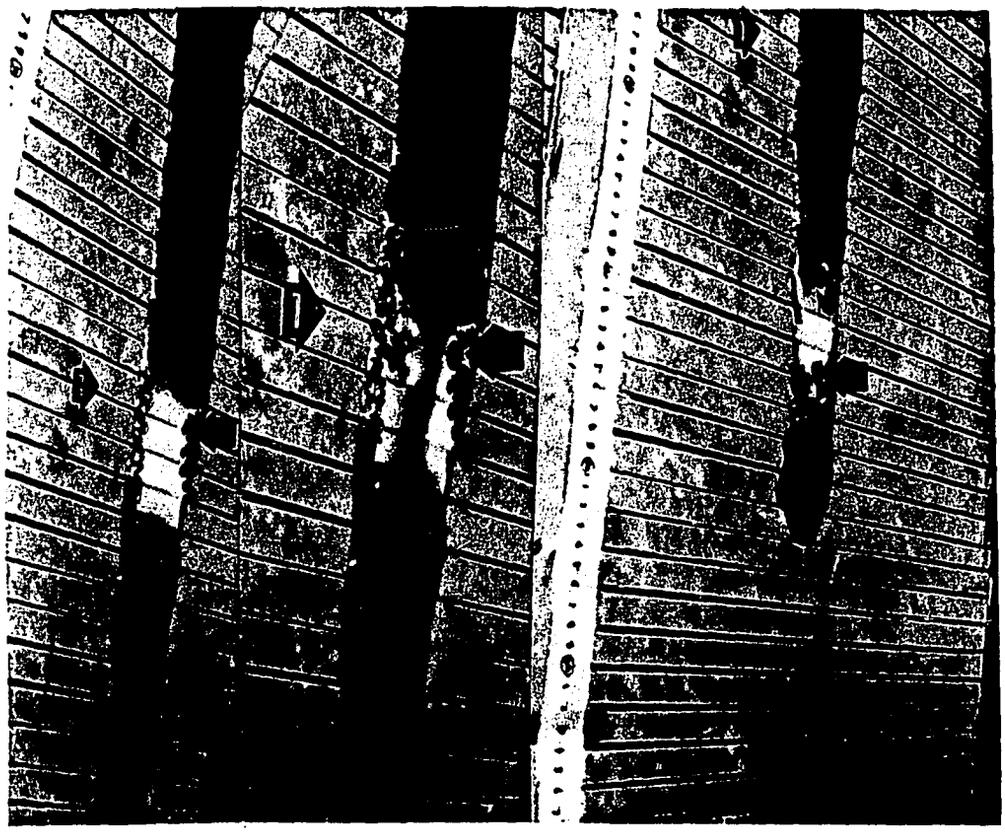

a b c

Thin solidified crusts (marked by dark arrow) develop and grow (a and b). Some portions are torn by the stream and float downstream, piling up, and increasing in thickness (c). Fig. b is a closer view of Fig. a at a later time. Arrow 1 marks the same location of the flow. (Flow conditions: T_{ext} = 88°C, T_{plate} = 41°C, θ = 6°, Q = 1.77 cc/sec., vol. = 62 cc.)

Fig. 5.17 Sequential photos of rough surface formation (R9-H)

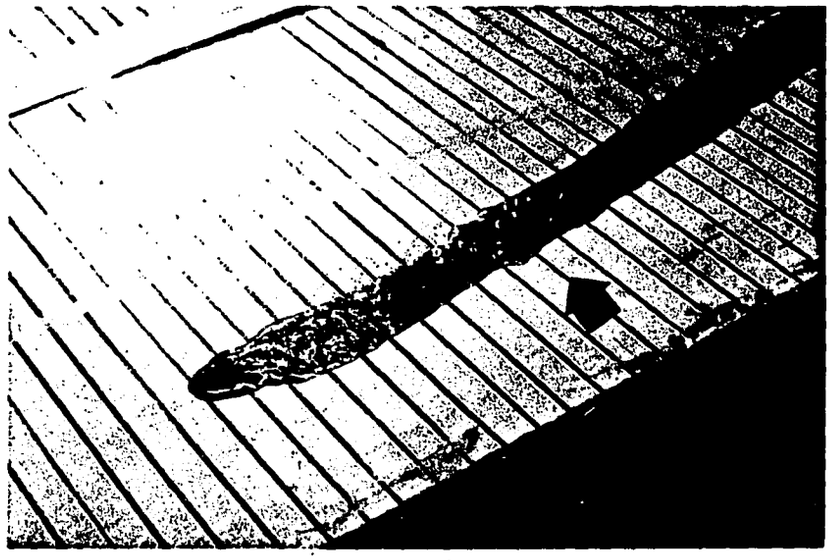

Final solidified form of surface texture is shown in Fig. 5.16b. (Center of Fig. 5.16b corresponds to the location marked by arrow.) Flow conditions are given in Fig. 5.16b. The similarity in surface texture and flow profile between this figure and Fig. 5.17c indicates repeatability of experiment.

Fig. 5.18 Surface texture of late stage of flow (R13-H)

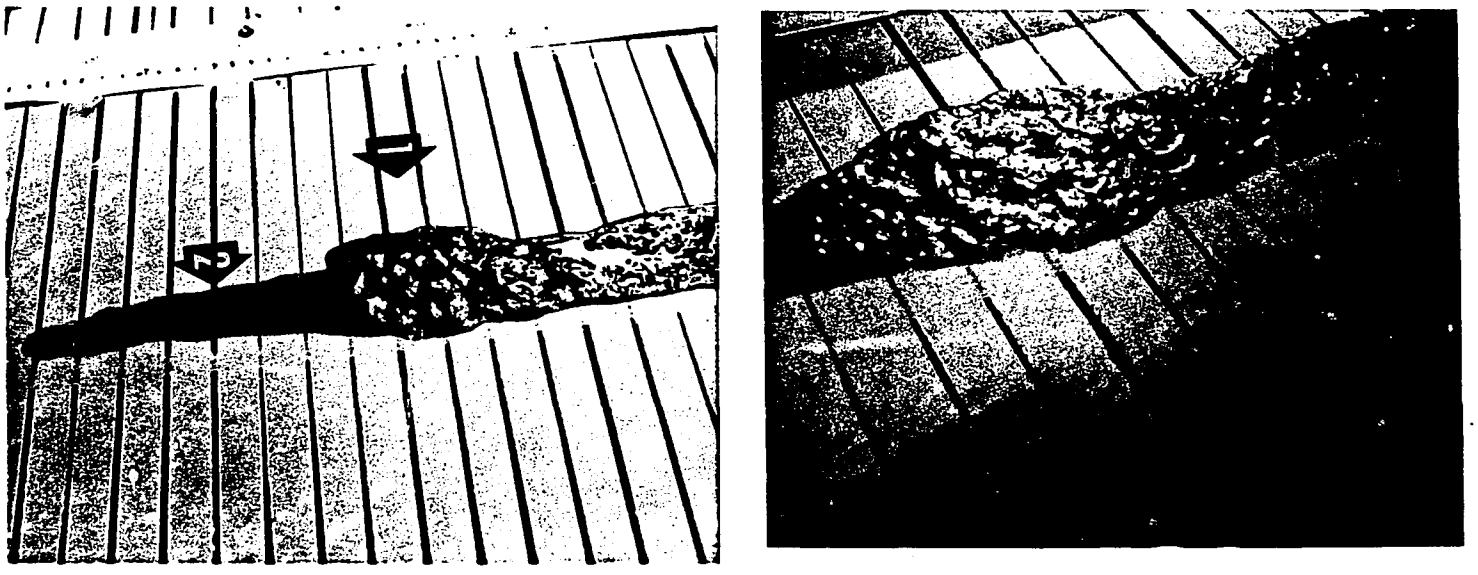

a b

Piled-up crusts act as barriers, thus the flow widens while part of the liquid drains and advances further (Arrow 2) Fig. b is a solidified form of the portion (Arrow 1) in a. (Flow conditions: T_{ext} = 90°C, T_{plate} = 45°C, θ = 4", Q = 3.75 cc/sec., vol. = 93cc.)

Fig. 5.19 Surface texture showing width increase (R10-H)

The very smooth surface texture developed in this flow is due to higher plate temperature. Flow essentially proceeded all the way down, and at very late stage, a crust started to develop (from around the end point of the long arrow). Thus, practically no crusts jumbled together, resulting in a very smooth skin (bright portion in the figure). Note the snout (dark arrow) that drained out from the front of the main body of the flow and had lower relief. (Flow conditions: T_{ext} = 88°C, T_{plate} = 48°C, = 2°, Q = 2.4 cc/sec., vol. = 108 cc.)

Fig. 5.20 Very smooth surface texture (R11-H).

Since the commercially available spindles of L.V.F. type viscometer were not suitable for the measurements of Kaolin suspension, two cylindrical spindles (diameter = 0.5 cm, and 1 cm, length = 7 cm) were made out of Aluminum.

Yield strength and viscosity were measured by the following method (52), using a cylindrical spindle.

The yield value can be directly determined with a cylindrical spindle whose length is several times greater than its diameter.

The spindle is revolved and the motor is stopped after freezing the pointer. Then the clutch is released to free the pointer which is observed while coming to rest.

If the fluid has a yield value, the pointer will not return to zero. In order to avoid overshooting the yield value due to the inertia of the spindle as driven by the uncoiling spring of the viscometer, the pointer need be stopped before it comes to rest. This is done by depressing the clutch several scale units above the point where the yield value was found in a previous reading, and then releasing the clutch to allow the pointer to move only a few scale units before stopping.

The yield strength of the fluid can then be calculated as (53),

$$M = \frac{\text{dial reading}}{\text{full-scale reading}} \times \text{dyne-cm torque for full scale} \qquad (5.2)$$

$$\tau_y = M/(2\pi R(h + h_o)R) \quad \text{in dynes/cm}^2 \qquad (5.3)$$

In the above equations,

M: torque

h: height of the spindle immersed

h_o: the end effect height

R: radius of the spindle.

Since τ_y is known, viscosity can be obtained from the plot of stress vs. rate of strain.

Stress at the surface of a bob (cylindrical spindle) of radius R_b is given by

$$\tau_b = M/2\pi R_b^2 h \tag{5.4}$$

and

$$\tau_y = M/2\pi R_c^2 h \tag{5.5}$$

where R_c is critical radius.

From Eq.(5.4) and (5.5),

$$\frac{R_c}{R_b} = \sqrt{\frac{\tau_b}{\tau_y}} \tag{5.6}$$

Strain rate can be expressed in terms of τ_b / τ_y as (52:65)

$$-\frac{dv}{dr} = \frac{2(\tau_b - \tau_y)}{(\tau_b - \tau_y) - \tau_y \ln (\tau_b/\tau_y)} \tag{5.7}$$

The plot of τ_b vs. $-\frac{dv}{dr}$ will give viscosity.

In this experiment, the end effect height was neglected. The bob was immersed to a depth of around 5 cm. The bob of 0.5 cm diameter was used most of the time, and a 600 ml pyrex beaker was used as a cup. The viscometer spindle guard was removed during the experiment. For all cases, the distance from the bottom of the cup to the end of the bob was greater

than 3 cm.

Measurements were carried out two or three times and yield values were averaged.

Using Eq.(5.7), strain rates were calculated and viscosities were obtained by least square fit to the data (rate of strain vs. stress) with fixed yield strength.

That is,

$$\mu = \frac{\Sigma \dot{\gamma}_i \tau_i - \tau_y \Sigma \dot{\gamma}_i}{\Sigma \dot{\gamma}_i^2} \tag{5.8}$$

where $\dot{\gamma}$ denotes strain rate.

Typical data so obtained are shown in Fig. 5.21.

Experiments were carried out in the same manner as the carbowax cases.

b. Flow emplacement and discussion Typical final flow profiles are shown in Fig. 5.22. The profiles look similar to those of carbowax flows, but the details are different. For example, flow thickness increased considerably down stream in carbowax flows but such an increase is not apparent in Kaolin flows.

In Kaolin flow of high yield strength, if the slope is low, the flow produced a dome, in which thickness decreases down stream from the vent.

The differences between Kaolin and Carbowax flows must have resulted from the very fundamental difference in fluid properties and processes. One is isothermal and the other is not.

Length dependence on yield strength and slope are shown in Fig. 5.23. As expected, the lower the strength the longer the flow (for fixed volume).

For flows of same yield strength, the effect of slope is very apparent as seen in the figure, which can also be realized in Fig. 5.22.

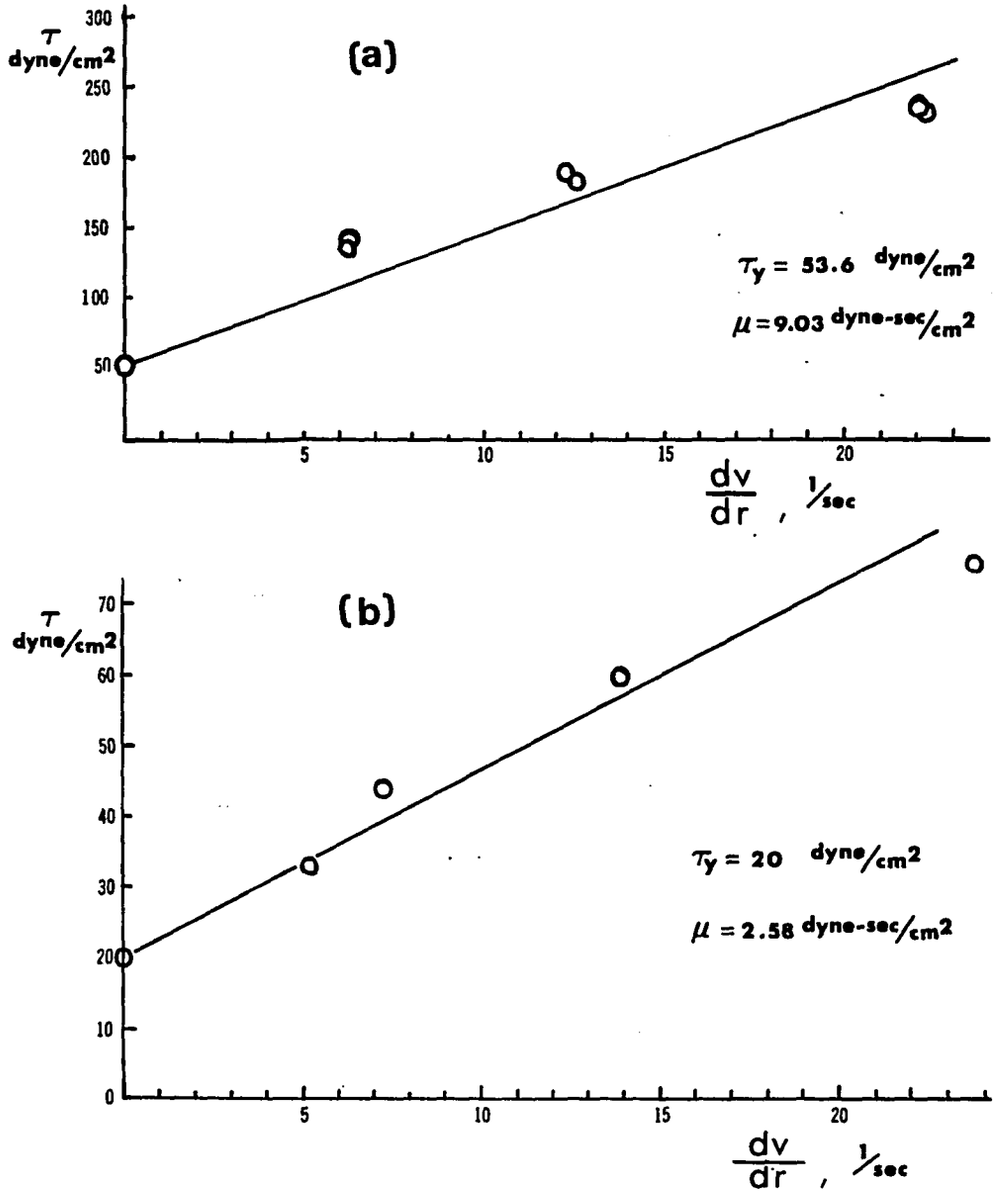

Fig. 5.21a Yield strength and viscosity of Kaolin suspension for K-19 run

Fig. 5.21b Yield strength and viscosity of Kaolin suspension for K-6 run

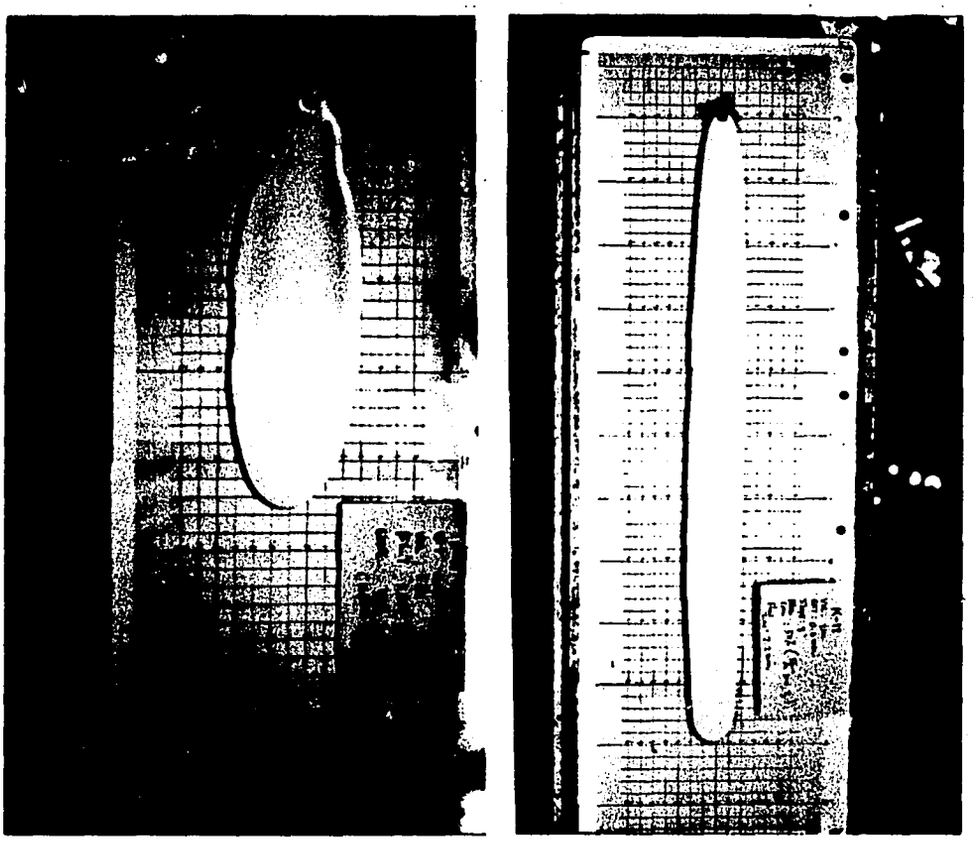

a b

a. Flow K-11 (Flow conditions: $Q = 0.674$ cc/sec., $\theta = 5°$, $\tau_y = 15.6$ dyne/cm^2, $\mu = 3.79$ dyne-sec/cm^2, $\rho = 1.68$ g/cm^3, vol. = 24.28 cc.)

b. Flow K-12 (except slope ($\theta = 8°$), other conditions are same as K-11)

Fig. 5.22 Typical profiles of Kaolin suspension flows

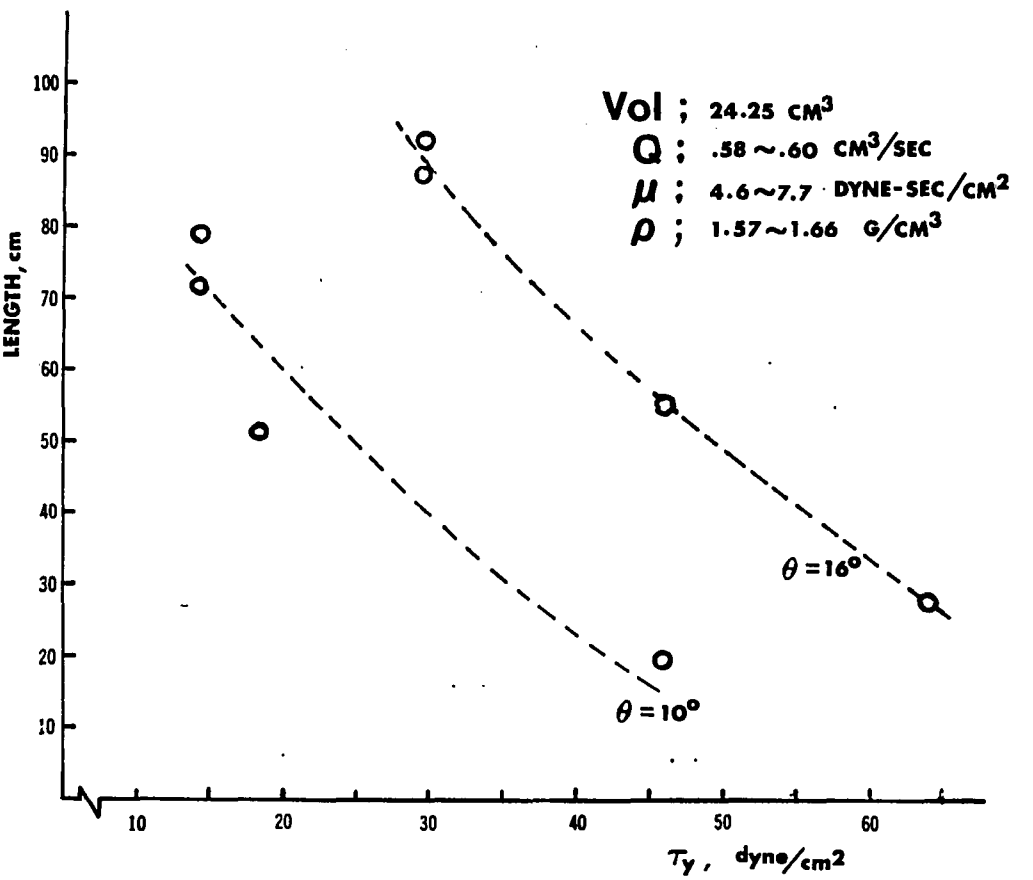

Fig. 5.23 Length vs. yield strength for Kaolin flows

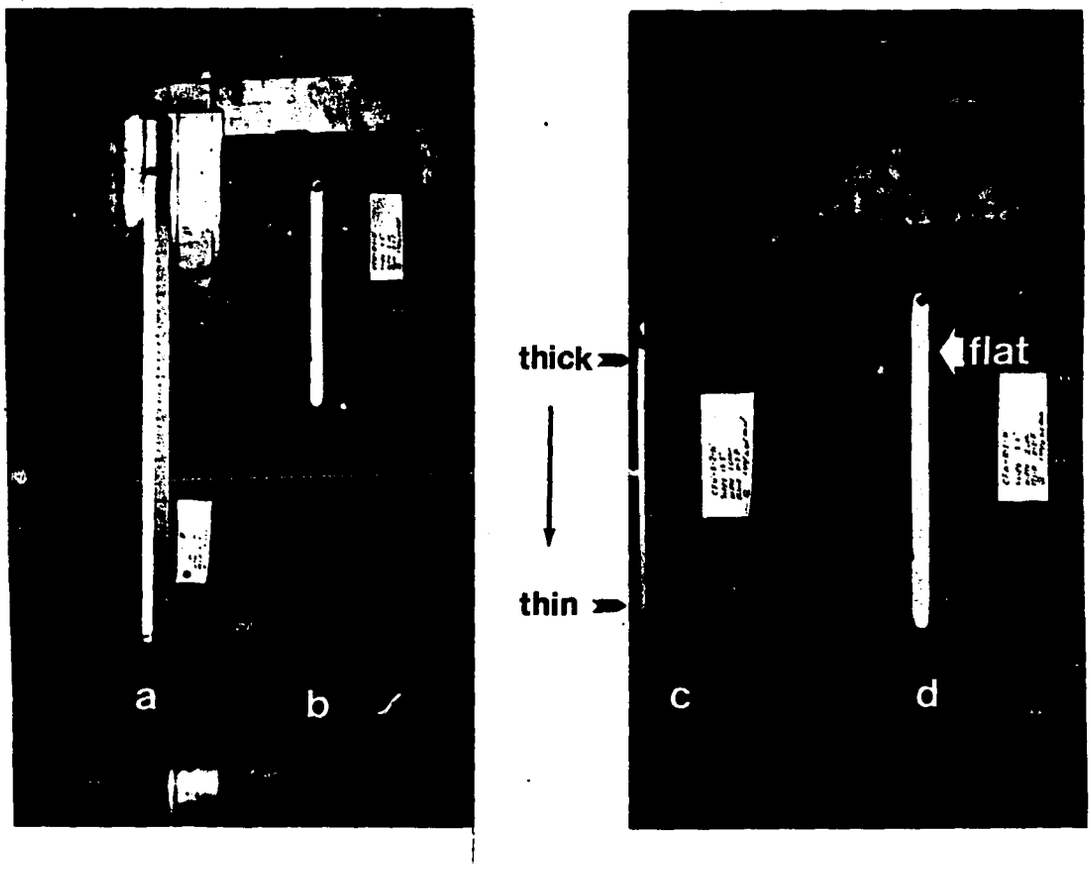

a. Flow C-K3P (Flow conditions: Q = 0.57 cc/sec., ρ = 1.72 g/cc, μ = 12.67 dyne-sec/cm^2, τ_y = 81.88 dyne/cm^2, channel width = 1.5 cm, θ = 20°, § E, Appendix)

b. Flow C-K1W (Flow conditions: θ = 12°, W = 2 cm, other conditions same as above)

c. Flow C-K2W (Flow conditions: W = 1 cm, other conditions same as C-K1W)

d. Flow C-K1W

Fig. 5.24 Rectangular channel flows of Kaolin suspension

The effect of slope was still apparent in channel flows, as can be seen in flow 'a' and 'b' in Fig. 5.24. Flow length of 'b' is about 26 cm and that of 'a' is about 57 cm.

Flow 'c' and 'd' in the same figure compare the length and flow profile of flows of different channel widths on the same slope. The channel width of 'c' is 1 cm and that of 'd' is 2 cm. But the final flow lengths are about the same. (In carbowax cases, lengths were much different, for example: 67 cm for W = 2 cm (C-C5W) and 94.5 cm for W = 1cm (C-C6W).)

This is not going to be the case for all flows of Kaolin. If Kaolin suspensions of much lower yield strength were used, lengths of the flows might be considerably different for different width channels.

Thickness (or depth) of flow 'c' gradually decreases with distance, so that the cross-section (along distance) would look similar to that of a shield, whereas for flow 'd', thickness is almost uniform.

It has been suggested in Chapter III, that the yield strength be estimated by the equation (3.40),

$$\tau_y = \frac{\lambda}{\lambda+2} \rho g \sin\theta h_f \ .$$

Actual data from the laboratory flows are plotted in Fig. 5.25. The final flow thicknesses (h_f) were calculated by

$$h_f = \frac{\text{Vol.}}{\text{Area}}$$

as in Carbowax cases.

For Hulme's data, measured levee depths (ζs) were used for h_f.

From the figure, we can note the trend that the dimensionless yield strength increases as yield strength increases for fixed aspect ratio,

which would not be the case if yield strength is the most important variable in forming the final dimensions of the flow.

In stopping the flow of an isothermal Newtonian Fluid on a smooth sloping surface, surface tension would be the most significant variable. Thus, from the figure, we can conjecture that surface tension should have played a considerable role in stopping the flow in addition to yield strength.

From τ_y and σ, we can form a dimensionless number, $\frac{\tau_y \ell}{\sigma}$, where ℓ is some characteristic length. Let us define the length scale, ℓ_R, as

$$\ell_R = \frac{\sigma}{\tau_y} \tag{5.9}$$

Then the dimensionless number $\frac{\tau_y \ell}{\sigma}$ can be expressed as ℓ / ℓ_R .

As yield strength increases, the length scale ℓ_R decreases. Further, other molecules in water usually lower the surface tension (54).

In this respect, ℓ_R should decrease very fast as τ_y increases in Kaolin suspension. Thus, the ratio ℓ / ℓ_R should increase much faster, the magnitude of which would be a measure of relative importance of surface tension to yield strength.

Since surface tensions were not measured, the magnitude of ℓ / ℓ_R could not be estimated. (Surface tension of water is 73 dyne/cm.)

For higher yield strength flows, the results seem to agree fairly well with Eq.(3.40).

Based on the discussions, C-4000 flow cross-sections of Fig. 5.6 can also be interpreted as a flow of gradually increasing yield strength characteristics. However, no attempts have been made to calculate 'effective' yield strengths along the flow emplacement.

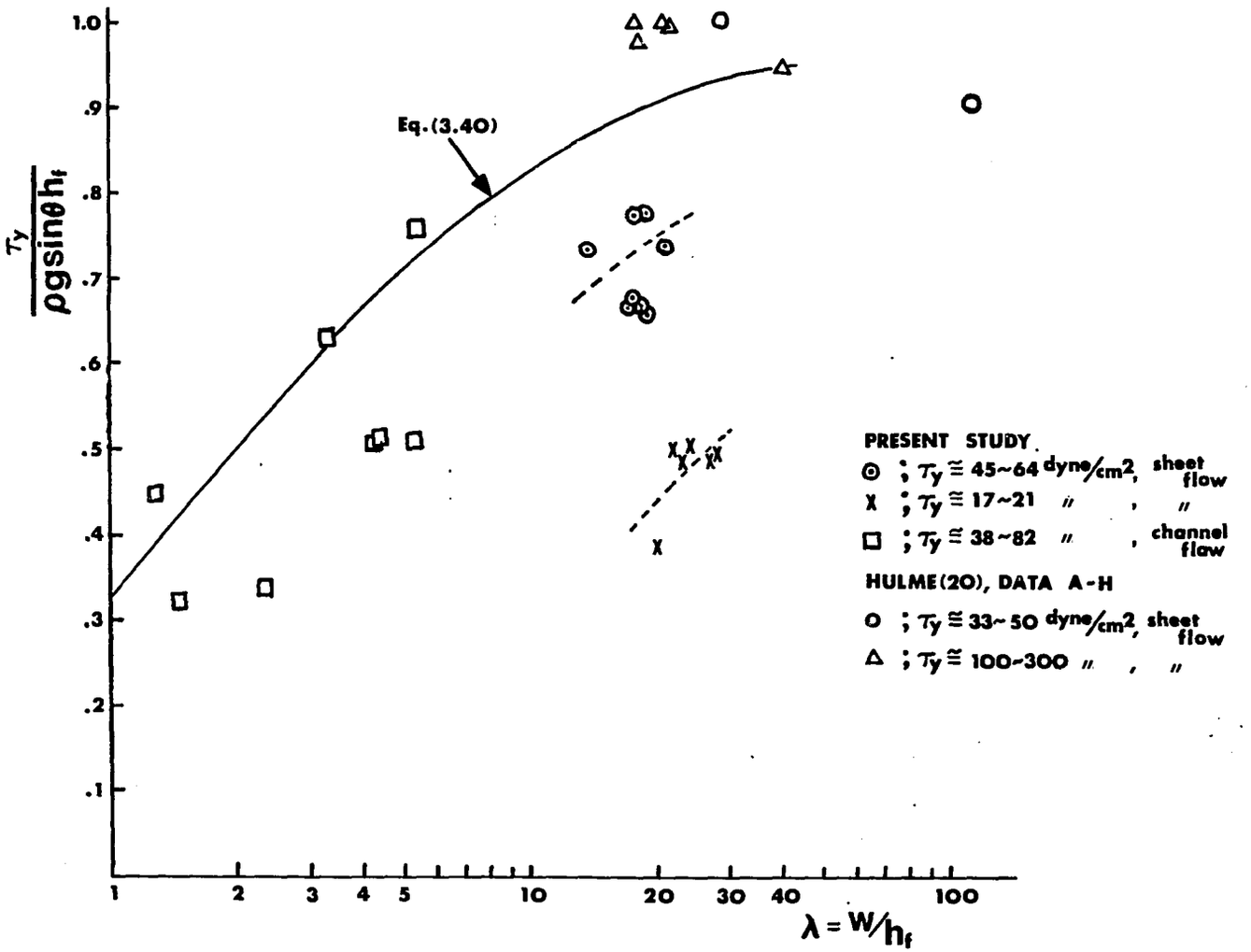

Fig. 5.25 Dimensionless yield strength vs. aspect ratio

Comparison of approximate theory of § B.2.b, Chapter III and experimental data are shown in Fig. 5.26.

For the present study, variables h_e and W were calculated from

$$h_e = \frac{\text{Vol.}}{A_{ext}} ,$$

$$W = \frac{A_f}{L_f}$$

For laboratory channel flow, W is given by the channel width. For both cases, Q_E (extrusion) was used for Q.

For Hulme's data h_e was calculated according to his equation (20: Eq.30) from measured levee height, ζ_s. Q was calculated from the variable F, which was calculated from the velocity measurement, which was measured some distance from the vent to ensure steadiness.

As can be seen from the figure, data points of the present study (rivulet flows) lie above the theoretical curves. This may be due to errors involved in calculation of h_e and W. Channel flow data and Hulme's data fit favorably to the curves. In channel flow data, W is given by the configuration, and in Hulme's data, Q and geometric lengths have been measured at certain cross-sections.

The lava data points fit to 2-dimensional curve ($\lambda = \infty$), even in the case of low aspect ratio flows.

It seems likely that some flow properties determined from full-scale observations might have been erroneously based on 2-dimensional theory.

4. Comparison of Carbowax and Kaolin Data

In this section, Carbowax and Kaolin flow data are compared on the basis of the suggested pseudo similarity of § C, Chapter IV.

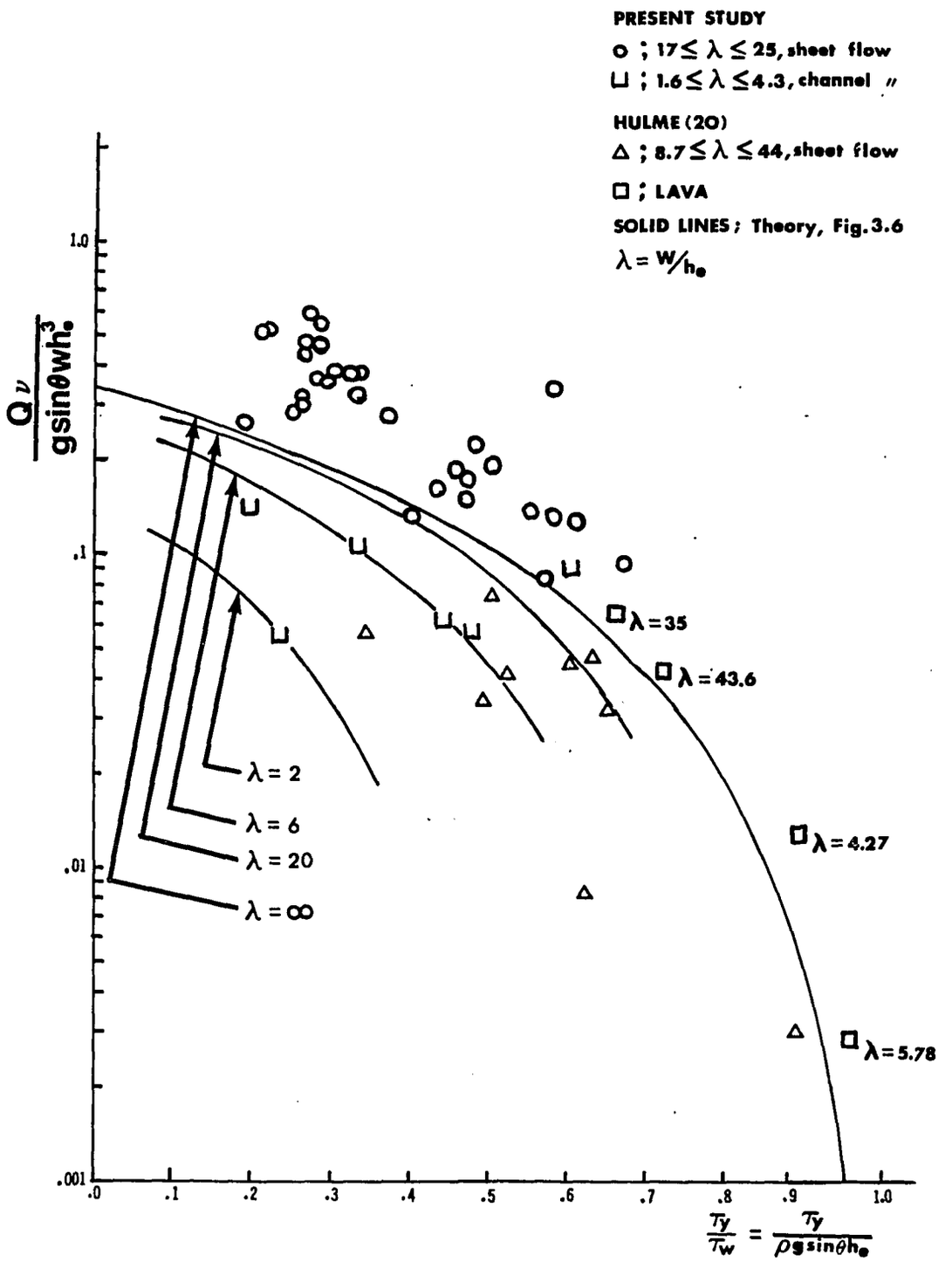

Fig. 5.26 Comparison of theory (§ B.2.b, Chapter III) and experimental data for Bingham plastic fluid flow

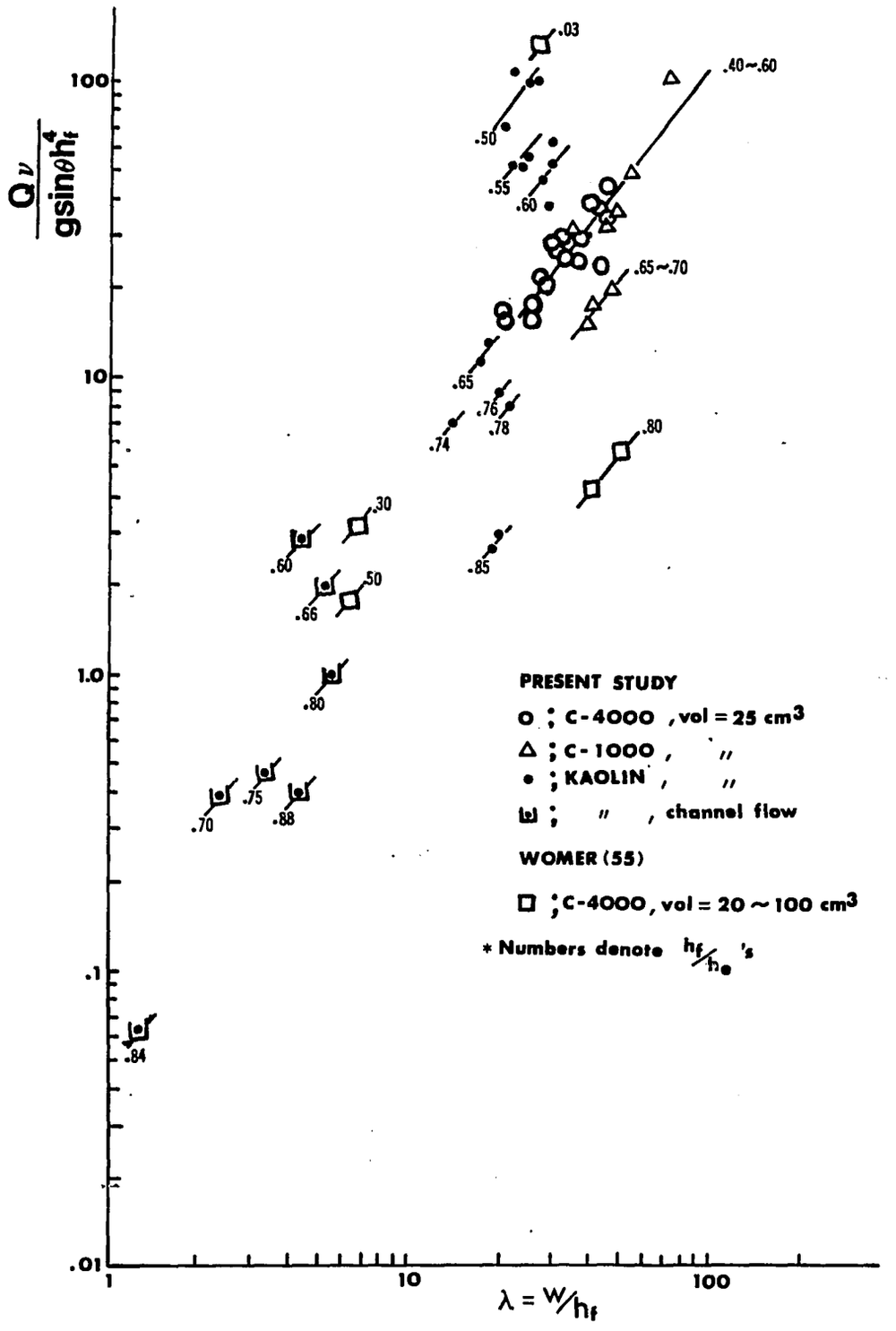

Fig. 5.27a $\frac{Q\nu}{g \sin\theta h_f^4}$ vs. $\frac{W}{h_f}$ for various $\frac{h_f}{h_e}$

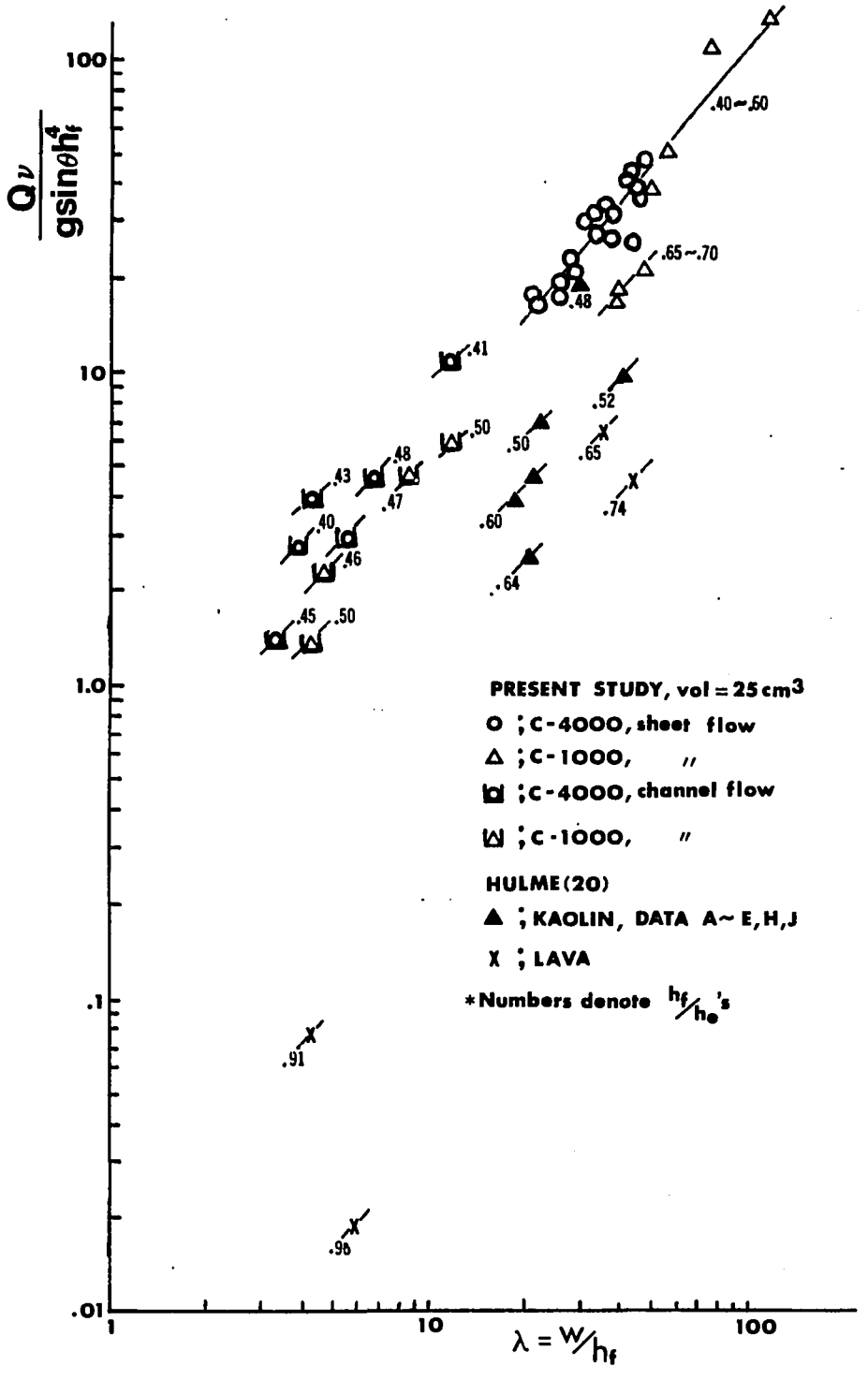

Fig. 5.27b $\frac{Q\nu}{g \sin\theta h_f^4}$ vs. $\frac{W}{h_f}$ for various $\frac{h_f}{h_e}$

Fig. 5.27c $\dfrac{Q\nu}{g \sin\theta\, h_f^4}$ vs. $\dfrac{h_f}{h_e}$ for various λ's

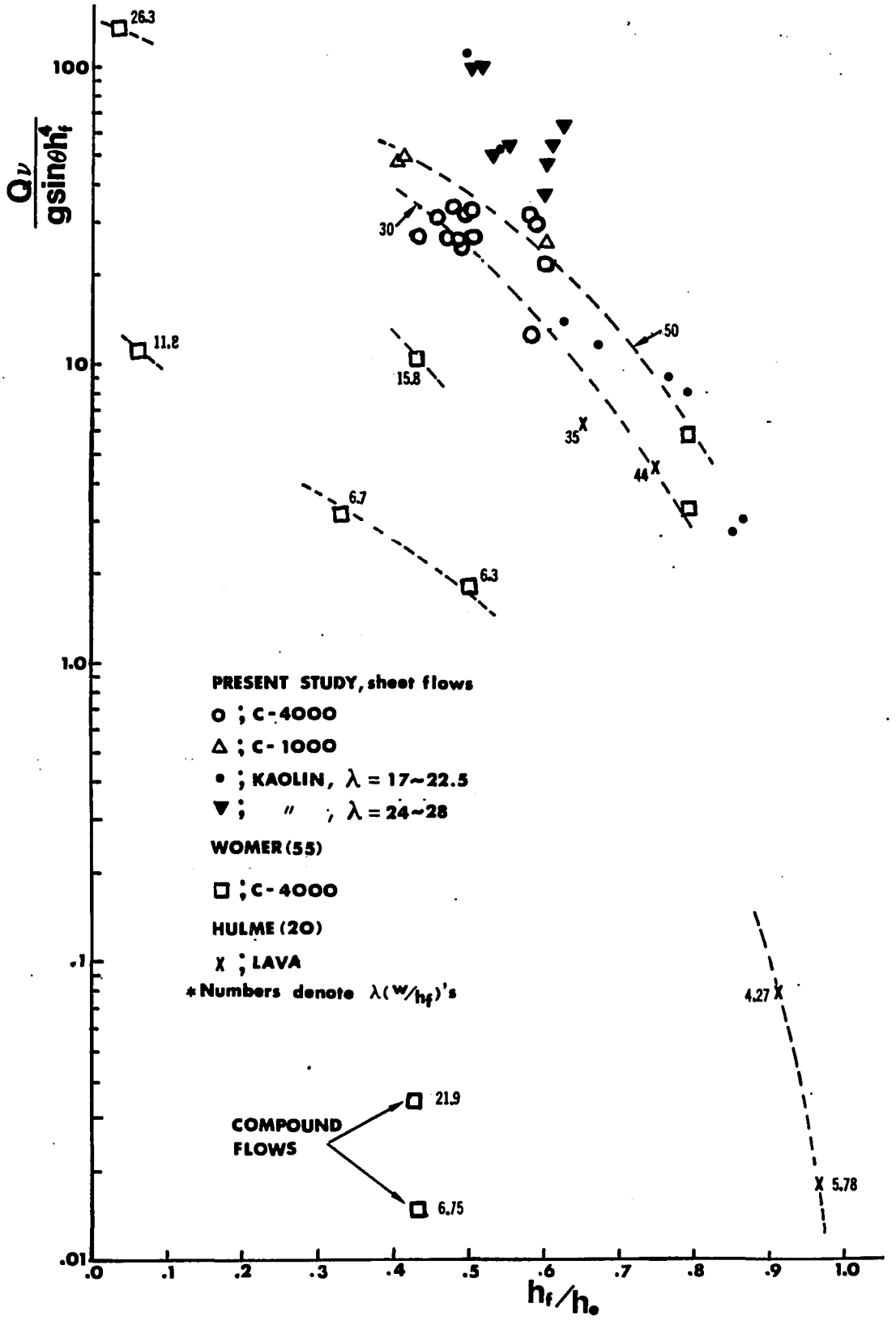
$\frac{Q\nu}{g\sin\theta h_f^4}$
100
10
1.0
.1
.01
.0
.1
.2
.3
.4
.5
.6
.7
.8
.9
1.0
h_f/h_o
26.3
11.8
30
15.8
50
35
44
6.7
6.3
4.27
5.78
21.9
6.75
COMPOUND FLOWS
PRESENT STUDY, sheet flows
○ ; C-4000
△ ; C-1000
• ; KAOLIN, λ = 17~22.5
▼ ; " ; λ = 24~28
WOMER (55)
□ ; C-4000
HULME (20)
X ; LAVA
* Numbers denote λ(w/hf)'s

As has been mentioned in the previous section, Carbowax flows and Kaolin flows are fundamentally different in their thermal and mechanical nature. Due to differences, flow dynamics are different as well.

However, if a pseudo-similarity law is used, these two flows can be broadly compared. We take the similarity form of Eq.(4.8c) for the basis of comparison.

The results are shown in Fig. 5.27a, b, and c. Fig. 5.27 a and b are plotted separately for convenience. Fig. 5.27 c is basically the same plot as Fig. 5.27 a and b except that the abscissa variable is h_f/h_e instead of λ.

From these figures, the following observations can be made.

i) Aspect ratio (W/h_f) increases with almost direct proportionality as $\frac{Q\nu}{g \sin\theta h_f^4}$ (henceforth referred to as Dimensionless extrusion rate) increases for fixed h_f/h_e.

ii) h_f/h_e decreases as Dimensionless extrusion rate increases for any given aspect ratio. (See Fig. 5.27c)

iii) Noting the slopes on log-log plot for the two different materials (Fig. 5.26c), we see that for Kaolin suspensions, the slope is much steeper than for Carbowax case. This may be due to cooling characteristics. That is, non-isothermal process (cooling) moderated the slope. If variables such as Q, ν, h_e were measured locally (i.e., station by station) and plotted, the slope should be steeper. For example, consider the flow cross-section of C-4000 (Fig. 5.7). Q would be equal to rate of extrusion near the vent, and h_e would be

much greater than h_f (final flow depth near vent) and hence h_f/h_e would be very small, and $\frac{Q\nu}{g \sin\theta h_f^4}$ would be very very high. Now consider the cross-section far from the vent (distance greater than L_e). In this case, the actual volume flow rate would be smaller than extrusion rate (drained by gravity without supply), and h_f would be much higher than that near the vent. Hence, h_f/h_e would increase very much whereas $\frac{Q\nu}{g \sin\theta h_f^4}$ would be much smaller. Thus, the results will produce very steep slopes.

iv) As can be seen from Fig. 5.6a and b, sheet flow can be viewed as a type of channel flow, which can also be realized from the previous section (Fig. 5.25 and 5.26).

v) The discrepancies in the data from the present study and from Hulme's may be due to evaluation of Q. For the present case, $Q = Q_E$, and for Hulme's case $Q = Q_u$ (See Fig. 5.4), as has been discussed previously.

vi) For compound flows, (see Fig. 5.6c), the trend discussed in i) and ii) may not apply. These cases may have to be studied separately from single unit flows. Qualitatively, compound flows would be produced by fairly large volume flows with low extrusion rate (thus, low Dimensionless extrusion rate, low h_f/h_e).

The tendencies written in i) and ii) can be anticipated from the 2-dimensional equation of Bingham material (Eq.(3.22)), which is

$$\frac{Q\mu}{\rho g \sin\theta W h_e^3} = \frac{1}{3}\left[1 - \frac{3}{2}\left(\frac{\tau_y}{\tau_W}\right) + \frac{1}{2}\left(\frac{\tau_y}{\tau_W}\right)^3\right]$$

It is reasonable to set $\frac{\tau_y}{\tau_W} = f(\lambda, h_f/h_e)$

Then the above expression can be written as

$$\frac{Q\nu}{g \sin\theta h_f^4} = \left\{\frac{h_e}{h_f}\right\}^3 \cdot \left\{\frac{W}{h_f}\right\} \cdot \frac{1}{3} f(\lambda, h_f/h_e) ,$$

which expresses the observations of i) and ii). Thus, we see that the relatively simple equation can be extended by introducing the average thickness h_f over area.

However, one point that should not be overlooked is the differences between the Carbowax and Kaolin suspension. Let us assume that we want to simulate Kaolin suspension flows by Carbowax 4000. Let the geometric scale factor be 1. Suppose we used same volume, and same extrusion rate, and same kinematic viscosity (initial viscosity for C-4000) as those of Kaolin suspension. For given h_f/h_e, $(0.4 < h_f/h_e < 0.7)$, carbowax will produce about twice as large aspect ratio as Kaolin. (Strictly speaking, this is only true when the aspect ratio of Kaolin suspension is around 20.) Thus, for the same final thickness (h_f), and for the same volume, the length of C-4000 flow will be only half as long as the Kaolin flows.

The above analysis looks a bit trivial, but it does introduce the important idea of 'distortion' (geometric).

VI. CONCLUSIONS AND SUGGESTIONS

A. General Discussion

As has been mentioned quite often, ultimately the goals of a similitude study are to understand every important aspect of the phenomena being investigated, and to predict the behavior as closely as possible using scaled model experiments.

As has been discussed in Chapter IV, achievement of complete similarity is nearly impossible. Furthermore, the variables do not include property dependencies on temperature, such as b in

$$\mu = \mu_o \exp (b/T),$$

and yield strength variation versus temperature, which may be very important. It was hoped, in this study, that the length h_f would reflect combined effects of all significant variables.

However, it is probably overly optimistic to conclude that pseudo-similarity will allow us to closely relate Carbowax results to lava flows.

It is quite possible that the results plotted in Fig. 5.27a, b, and c would look different if some other material were used which solidified as it cooled.

If a certain set of materials of known properties are chosen, for which a wide range of values for each significant dimensionless parameter can be obtained, then we can carry out experiments, and results of these can be compared and combined to give quantitative information on the similarity law. From this information, we can derive fairly accurate similarity principles and predictive equations for lava flow.

However, for the reasons stated above, at the present time, the infor-

mation given in Fig. 5.27 must remain as the basis for qualitative understanding of lava flow.

B. Scaling Problems

1. Extrusion rate (Q_E) scaling

Let us assume that the Carbowax flows properly simulate lava flows. Then what would be the scaling relations? For lava flow on a fairly uniform slope, the discussions provided in Chapter V for Carbowax flow would be fairly accurate, and even be able to provide quantitative evaluations. Let us consider a more complex geological modeling problem, where average slope may be defined.

The similarity law is Eq.(4.8c)

$$\frac{Q\nu}{g \sin\theta\, h_f^4} = f_1\left(\frac{h_f}{h_e}, \frac{W}{h_f}\right)$$

or

$$\frac{W}{h_f} = f_2\left(\frac{Q\nu}{g \sin\theta\, h_f^4}, \frac{h_f}{h_e}\right)$$

Hence, we require

$$\left(\frac{W}{h_f}\right)_m = \left(\frac{W}{h_f}\right)_p \tag{6.1}$$

$$\left(\frac{Q\nu}{g \sin\theta\, h_f^4}\right)_m = \left(\frac{Q\nu}{g \sin\theta\, h_f^4}\right)_p \tag{6.2}$$

$$\left(\frac{h_f}{h_e}\right)_m = \left(\frac{h_f}{h_e}\right)_p \tag{6.3}$$

Now let us set the scale factor to be n. Though we can choose any scale factor at will, if we maintain the view that the final depth is a measure of the averaged yield strength τ_y, then scale factor n should be chosen as

$$n = \frac{(\tau_{y/\rho\, g \sin\theta})_p}{(\tau_{y/\rho\, g \sin\theta})_m}$$

Then,
$$(h_f)_p = n(h_f)_m$$

$$(W)_p = n \cdot (W)_m$$

and

$$Q_p = \frac{\nu m}{\nu p} \cdot \frac{(g \sin\theta)_p}{(g \sin\theta)_m} \cdot n^4 \cdot Q_m$$

$$(\text{Vol.})_p = n^3 \cdot (\text{Vol.})_m$$

2. Velocity scaling

In the discussions in previous chapters, Q has been used in two ways, that is Q_E and Q_u. If it is used as Q_E, extrusion rate, we imply that geometric variables are dependent variables on Q_E. If it is used as Q_u, we imply that the cross-sectional geometry determines the flow rate.

Hence, velocity scale will be provided on the basis of the latter view point.

Since $Q_u = u_{av} \cdot$ cross-sectional area, we have

$$\frac{(u_{av})_p}{(u_{av})_m} = \frac{(g \sin\theta)_p}{(g \sin\theta)_m} \frac{(h_f^4)_p}{(h_f^4)_m} \cdot \frac{(\text{Cross-sectional Area})_m}{(\text{Cross-sectional Area})_p} \cdot \frac{\nu m}{\nu p}$$

$$= \frac{\nu m}{\nu p} \cdot \frac{(g \sin\theta)_p}{(g \sin\theta)_m} \cdot n^2$$

Note that the Froude law (Hodgson (47)) results in

$$\frac{u_p}{u_m} = n^2 \qquad \text{if } g_p = g_m,\ \sin\theta_p = \sin\theta_m$$

Thus, the suggested similarity law of the present study adds viscous correction to the Froude law.

C. Application of the Channel Flow Theory

The channel flow theory of Kozicki et al., introduced in § B.2.b, Chapter III, may be applicable to the field study as a better approximation than the simple two-dimensional flow theory.

Suppose that the geometry of lava flow such as flow thickness, levee height and width is available.

Then, the yield strength may be estimated by (§ B.3, Chapter III)

$$\tau_y = \frac{\lambda}{\lambda+2}\,\rho\, g \sin\theta\, h_f\ , \quad \lambda = \frac{W}{h_f}\ .$$

Also, the bulk velocity equation (Eq.(3.27)),

$$\frac{2U}{r_H} = \frac{\tau_o}{\mu}\left[\frac{1}{a+b} - \frac{1}{b}\left(\frac{\tau_y}{\tau_o}\right) + \frac{a}{b(a+b)}\left(\frac{\tau_y}{\tau_o}\right)^{b/a+1}\right]$$

may be used for various purposes, depending on which variables need to be estimated and which variables are known.

The two equations written above are more favorable than the two-dimensional equations which have been used often previously, for example, by Moore et al.(21).

D. Conclusions and Suggestions for Further Study

i) In addition to the discussions of previous sections B and C, the

analysis provided throughout the text (mainly Chapter III and V) will be beneficial to interpretation and understanding of lava flow rheology, and should be also applicable to mud flows.

ii) It has been confirmed that the observed surface textures of lava (basaltic) are the result of cooling from the top, through the experiments using the heated plate.

iii) For a given extrusion rate and width, it has been supposed that the depth ratio, $\frac{h_f}{h_e}$, will depend on thermal variables, that is,

$$\frac{h_f}{h_e} = f \text{ (temperature ratio, Pr, Nu, etc.)}.$$

Hence, if the cooling mechanisms are very similar, $\frac{h_f}{h_e}$ will be mostly influenced by the temperature ratio (ratio of extrusion temperature to fusion temperature) as has been observed from the Carbowax experiments, where we obtained

$$\frac{h_f}{h_e} \alpha \sqrt{\frac{T}{T_F}} \quad .$$

Thus, it is desirable to review the existing lava data in terms of the pseudo-similarity, since the cooling mechanisms would be quite similar for almost all lava flows (subaerial).

To get a more precise look at the effects of thermal variables to the pseudo-similarity law, it would be necessary to run experiments using some other materials.

iv) It is suggested that numerical analysis for the flow situation in § B.7, Chapter III, which incorporates more strict and realistic conditions be carried out. For example, a solution procedure like Marker and Cell

Method (56) may be useful, although the associated stefan problem (23) may pose some difficulties.

v) Kaolin suspensions were used in this study to confirm the theories of flow for isothermal Bingham material. However, during the experiment it was realized that the lava domes (rhyolite or dacite) may best be simulated by Kaolin suspension. A lava dome may be considered a flow extruded with very high yield strength and viscosity so that the variations of these with temperature may be very little, and hence the effect of the variation may not be as significant as variations of slope, extrusion rate, etc.

VII. BIBLIOGRAPHY

1. Leet, L. D., Judson, S. and Kauffman, M.E. Physical Geology. Englewood Cliffs, N.J.: Prentice Hall, 1978.

2. Green, J., and Short, N. M. Volcanic Landforms and Surface Features. New York: Springer-Verlag, 1971.

3. Williams, H., and McBirney, A. R. Volcanology. San Francisco, Ca: Freeman, Cooper and Company, 1979.

4. Ollier, C. Volcanoes. Cambridge, Mass.: MIT Press, 1969.

5. Sakuma, S. and Nagata, T. "Physical volcanology". In Handbuch der Physik, Vol. XLVIII, Geophysics II, pp. 982-1011. S. Flügge, ed. Berlin: Springer-Verlag, 1957.

6. Shaw, H. R., Wright, T. L., Peck, D. L., and Okamura, R. "The viscosity of basaltic magma: An analysis of field measurement in Makaopuhi Lava Lake, Hawaii". American Journal of Science, 266 (1968), 225-264.

7. Wehausen, J. V. and Laitone, E. V. "Surface waves". In Handbuch der Physik, Vol. IX, Fluid Dynamics III, pp. 446-758. S. Flügge, ed. Berlin: Springer-Verlag, 1960.

8. Walker, G. P. L. "Length of lava flows". Phil. Trans. R. Soc., London, A, 274 (1973), 107-118.

9. Malin, M. "Lengths of Hawaiian lava flows". Geology, 8 (1980), 306-308.

10. Minakami, T. "On the temperature and viscosity of the fresh lava extruded in the 1951 O-shima eruption". Bull. Earthq. Res. Inst., 29 (1951), 487-498.

11. Harrison, C. G. A. and Rooth, C. "The dynamics of flowing lavas". In Volcanoes and Tectonosphere. Hitoshi Aoki and Suzuma Iizuka, eds. Tokyo: Tokai University Press, 1976.

12. Greeley, R. "Observations of actively forming lava tubes and associated structures, Hawaii". Modern Geology, 2 (1971), 207-223.

13. Peterson, D. W. and Swanson, D. A. "Observed formation of lava tubes". Studies in Speleology, 2, Pt. 6 (1974), 209-223.

14. Fink, J. H. and Fletcher, R. C. "Ropy pahoehoe: Surface folding of a viscous fluid". J. Volcan. Geother. Res., 4 (1978), 151-170.

15. Macdonald, G. A. Volcanoes. Englewood Cliffs, N.J.: Prentice Hall, 1972.

16. Carr, M.H. and Greeley, R. "Volcanic features of Hawaii". NASA Sp-403, 1980.

17. Prager, W. Introduction to the Mechanics of Continua. New York: Dover, 1961.

18. Batchelor, B. K. An Introduction to Fluid Dynamics. London: Cambridge University Press, 1967.

19. Hohenemser, K. and Prager, W. "Über die Ansätze der Mechanik istroper Kontinua". Zeitschrift f. angew. Math. u. Mech., 12 (1932), 216-226.

20. Hulme, G. "The interpretation of lava flow morphology". Geophys. J. Roy. Astro. Soc., 39 (1974), 361-383.

21. Moore, H. J. and Schaber, G. G. "An estimate of the yield strength of the Imbrium flows". Proc. Lunar Sci. Conf., 6 (1975), 101-118.

22. Berker, R. "Integration des équations du mouvement d'un fluide visqueux incompressible". In Handbuch der Physik, Vol. VIII/2, Fluid Dynamics II, pp. 1-384. S. Flügge, ed. Berlin: Springer-Verlag, 1963.

23. Rubenstein, L. I. The Stefan Problem. Providence, R.I.: American Mathematical Society, 1971.

24. Kozicki, W. and Tiu, C. "Non-Newtonian flow through open channels". The Canadian J. of Chem. Engr., 45 (1967), 127-134.

25. Mooney, M. "Explicit formulas for slip and fluidity". J. Rheology, 2 (1931), 210-222.

26. Rabinowitch, B. "Über die Viskosität und Elastizität von Solen". Zeitschrift f. Physik. Chem., A145 (1929), 1-26.

27. Johnson, A. M. and Hampton, M. A. "Subaerial and subaqueous flow of slurries". Final Report. U.S. Geol. Survey. Banner Library, Stanford Univ., Stanford Calif., 1969.

28. Cea, J. and Glowinski, R. "Methodes Numeriques pour l'Ecoulement Laminaire d'un Fluide Rigide Viscoplastique Incompressible". Inter. J. of Computer Math., Section B, 3 (1972), 225-255.

29. Moore, H. J., Arthur, D. W. G. and Schaber, G. G. "Yield strengths of flows on the Earth, Mars, and Moon". Proc. Lunar Planet. Sci. Conf., 9 (1978), 3351-3378.

30. Towell, G. D. and Rothfeld, L. B. "Hydrodynamics of Rivulet Flow". A. I. Ch.E. Journal, 12 (1966), 972-980.

31. Lord Rayleigh. "On the theory of capillary tube". Proc. Roy. Soc. London, Series A, 92 (1916), 184-195.

32. Sparks, R. S. J., Pinkerton, H. and Hulme, G. "Classification and formation of lava levees on Mount Etna, Sicily". Geology, 4 (1976), 269-271.

33. Iversen, J. D., Unpublished note, Department of Aerospace Engineering, ISU, 1978.

34. Mei, C. C. "Non-linear gravity waves in a thin sheet of viscous fluid". J. Math. Phys., 45 (1966), 266-288.

35. Lovering, T. S. "Heat conduction in dissimilar rocks and the use of thermal models". Bull. Geol. Soc. Amer., 47 (1936), 87-100.

36. Jaeger, J. C. "Cooling and solidification of igneous rocks". Basalts, Vol. 2. H. H. Hess and Arie Poldervaart, eds. New York: Interscience Publishers, 1968.

37. Larkin, B. K. "Some stable explicit difference approximations to the diffusion equation". Math. of Comp., 18 (]964),]96-202.

38. Danes, Z. F. "Dynamics of lava flows". J. Geophys. Res., 77 (1972), 1430-1432.

39. Murase, T. and McBirney, A. R. "Viscosity of lunar lavas". Science, 167 (1970), 1491-1493.

40. Shaw, H. R. and Swanson, D. A. "Eruption and flow rates of flood basalts". Proceedings of the Second Columbia River Basalt Symposium. E. H. Gilmour and E. Stradling, eds. Cherney, Wash.: Eastern Washington State College, 1969.

41. Murphy, G. Similitude in Engineering. New York: The Ronald Press, 1950.

42. Wilson, E. B. Jr. An Introduction to Scientific Research. New York: McGraw-Hill, 1952.

43. Van Driest, E. R. "On dimensional analysis and the presentation of data in fluid flow problems". J. Applied Mech., 13 (1946), A34.

44. Bridgman, P. W. Dimensional Analysis. New Haven, Conn.: Yale Univ. Press, 1922.

45. Langhaar, H. L. Dimensional Analysis and Theory of Models. Huntington, N.Y.: Robert E. Krieger Co., 1980.

46. Sedov, L. I. Similarity and Dimensional Methods in Mechanics. New York: Academic Press, 1959.

47. Hodgson, G. W. "An experimental investigation of simulated lava flows using carbowax materials". M.S. thesis, Air Force Institute of Technol., Wright-Patterson A. F. B., Ohio, 1969.

48. Womer, M. ., Greeley, R., Iversen, J. D., and Kremer, J. "Scale model simulation of lava flows". Reports of Planetary Geology Program, 1979-1980. NASA TM 81776, 1980.

49. Gebhart, B. Heat Transfer. New York: McGraw-Hill, 1971 .

50. Bird, R. B., Armstrong, R. C. and Hassager, O. Dynamics of Polymeric Liquids. Vol. 1. New York: John Wiley, 1977.

51. Thieling, L. F. Union Carbide Corp., New York, Private Communication, November 5, 1979.

52. Union Carbide Corp. "Carbowax polyethylen glycols". Union Carbide Corp., New York, 1978.

53. Van Wazer, J. R., Lyons, J. W., Kim, K. Y. and Colwell, R. E. Viscosity and Flow Measurement. New York: Interscience Publishers, 1963.

54. Trefethen, L. "Surface tension in fluid mechanics". In Illustrated Experiments in Fluid Mechanics. National Committee for Fluid Mechanics Films, eds. Cambridge, Mass.: MIT Press, 1972.

55. Womer, M. "LSF 4000 Data Sheets". Data file. Planetary Geology Program, Ariz. State Univ., Tempe, Az., 1978.

56. Welch, J. E., Harlow, F. H., Shannon, J. P. and Daly, B. J. "The MAC method, a computing technique for solving viscous, incompressible, transient fluid flow problems involving free surfaces". Los Alamos Scientific Laboratory Report LA-3425, 1965.

VIII. ACKNOWLEDGEMENTS

The author expresses his deep thanks to his major advisor, Dr. James D. Iversen for his consistent guidance, support, and generosity that allowed freedom of research during the pursuit of the present work.

Sincere thanks should also go to Dr. L. N. Wilson and Dr. J. C. Tannehill of Aerospace Engineering, Dr. R. H. Pletcher of Mechanical Engineering, and Dr. B. E. Nordlie of Geology for serving as members of the advisory committee.

Portions of this research and final write-up were carried out during the author's stay in the Planetary Geology Program at the Department of Geology, Arizona State University from January 26, 1981, to June 4, 1981, while participating in the exploratory experiments on sulfur flows which were both interesting and enjoyable to watch.

Dr. R. Greeley of the Geology Department, A. S. U. made the stay possible, and allowed free access to the "Space Photo Lab" facilities.

Dr. Jonathan Fink of A. S. U., pleasantly agreed to share his office with the author, provided invaluable discussions and assistance on the research and write-up.

Sincere gratitude should go to Dr. R. Greeley and Dr. Jonathan Fink.

Thanks also go to Mr. Gary Beardmore and Mr. Steve Myers who provided technical assistance in the experiments with heated plates.

Dr. B. Booth of Imperial College of London, (now in Birbeck College), provided helpful discussions with the author during his stay at Iowa State University during Spring Quarter of 1980.

His interest in the present work is also acknowledged.

Financial assistance has been provided by NASA Ames Research Center and the Engineering Research Institute of I. S. U., for which the author is deeply grateful.

Thanks are due to the typist for this thesis, Miss Cathie Mathes.

Finally, the author's deepest thanks go to his parents and family, who provided steady encouragement and patience throughout the years.

To them, this small volume is dedicated.

IX. APPENDIX A

A. Raw Data For C-4000 and 1000 Flows

Run No.	Index[1]	Q	θ	Ext. Time	Ext. Temp.	Vol.	Length	Area
		$cm^3/sec.$	deg.	sec.	°C	cm^3	cm	cm^2
1.	4	0.460	5	108	85	49.7	82.5	345.5
2.	"	"	"	"	88	"	77.0	341.0
3.	"	"	"	"	86	"	74.2	377.5
4.	"	"	"	"	71	"	76.3	306.7
5.	"	"	"	"	72	"	83.6	318.4
6.	"	"	"	"	66	"	73.5	305.3
7.	"	0.530	12	48	85	25.5	96.8	226.3
8.	"	"	"	"	86	"	92.1	239.5
9.	"	"	"	"	86	"	104.4	232.9
10.	"	"	"	"	85	"	100.7	239.9
11.	"	"	"	"	"	"	103.3	229.2
12.	"	"	"	"	"	"	94.1	237.6
13.	"	0.460	3	108	"	49.7	57.7	303.6
14.	"	"	"	"	86	"	58.2	316.3
15.	"	"	"	"	73	"	54.7	277.3
16.	"	"	"	"	75	"	51.3	258.5
17.	"	"	"	"	75	"	53.4	264.7
18.	"	"	"	"	73	"	51.7	271.8
19.	"	"	"	"	75	"	59.5	287.3
20.	"	"	"	"	"	"	60.8	263.5
21.	"	"	"	"	72	"	58.1	280.9
22.	"	"	"	110.4	91	50.9	70.8	340.3
23.	"	"	3.5	"	84	"	67.3	317.8
24.	"	"	"	"	80	"	63.3	316.6
25.	1	"	3	108	72	49.7	55.5	307.8
26.	"	"	"	"	"	"	57.0	340.4
27.	"	"	"	"	83	"	75.7	380.2

[1] 1 denotes C-1000 and 4 denotes C-4000.

Run No.	Index	Q	θ	Ext. Time	Ext. Temp.	Vol.	Length	Area
		$cm^3/sec.$	deg.	sec.	°C	cm^3	cm	cm^2
28.	1	0.460	5	108	68	49.7	77.7	305.1
29.	"	"	"	"	63	"	83.3	422.4
30.	4	"	3	"	89	"	66.6	325.8
31.	"	"	5	"	86	"	71.7	375.8
32.	"	"	"	"	"	"	74.5	387.4
33.	"	"	"	"	"	"	70.7	364.6
34.	"	"	"	"	"	"	76.9	391.7
35.	"	"	"	"	"	"	74.7	350.8
36.	"	"	"	"	"	"	79.5	389.0
37.	"	"	"	"	76	"	67.8	317.5
38.	"	"	"	"	86	"	87.0	341.5
39.	"	0.530	3	48	70	25.5	34.5	185.2
40.	"	"	"	"	85	"	37.0	204.6
41.	"	"	"	"	70	"	32.6	187.4
42.	"	"	"	"	"	"	32.8	191.7
43.	"	"	"	"	75	"	35.2	179.6
44.	"	"	"	"	"	"	33.0	188.8
45.	"	"	"	"	"	"	34.3	192.0
46.	"	"	"	"	80	"	36.6	195.6
47.	"	"	"	"	"	"	35.1	193.2
48.	"	"	"	"	"	"	37.9	178.4
49.	"	"	"	"	85	"	37.9	201.6
50.	"	"	"	"	"	"	41.0	203.0
51.	"	0.505	"	"	90	24.3	36.0	196.1
52.	"	0.518	"	"	"	24.9	38.7	217.6
53.	"	"	"	"	"	"	39.0	217.2
54.	"	0.511	"	97.2	"	49.7	59.0	370.0
55.	"	"	"	"	"	"	60.8	372.5
56.	"	"	"	"	"	"	63.3	368.3

Run No.	Index	Q	θ	Ext. Time	Ext. Temp.	Vol.	Length	Area
		$cm^3/sec.$	deg.	sec.	°C	cm^3	cm	cm^2
57.	4	0.511	3	97.2	90	49.7	52.3	361.4
58.	"	"	"	"	"	"	57.0	351.7
59.	"	0.512	5	48.6	75	24.9	47.1	213.8
60.	"	"	"	"	"	"	49.3	219.4
61.	"	"	"	"	"	"	47.4	223.8
62.	"	"	"	"	70	"	49.2	214.3
63.	"	"	"	"	"	"	48.5	214.6
64.	"	"	"	"	80	"	50.4	226.9
65.	"	"	"	"	"	"	52.2	221.0
66.	"	"	"	"	"	"	47.5	222.4
67.	"	"	"	"	85	"	51.2	230.8
68.	"	"	"	"	"	"	53.8	234.3
69.	"	"	"	"	"	"	53.5	234.6
70.	"	"	"	"	90	"	53.5	212.4
71.	"	"	"	"	"	"	56.0	227.6
72.	"	"	8	"	75	"	67.8	222.7
73.	"	"	"	"	"	"	66.1	231.1
74.	"	"	"	"	"	"	76.0	227.4
75.	"	"	"	"	70	"	67.5	224.2
76.	"	"	"	"	"	"	77.4	217.4
77.	"	"	"	"	80	"	70.0	234.3
78.	"	"	"	"	70	"	64.4	192.3
79.	"	"	"	"	80	"	71.3	235.9
80.	"	"	"	"	"	"	68.9	236.8
81.	"	"	"	"	88	"	76.2	237.6
82.	"	"	"	"	90	"	82.0	239.5
83.	"	"	"	"	"	"	76.4	240.1
84.	"	"	"	"	85	"	76.3	228.7
85.	"	"	"	"	"	"	78.1	229.1

Run No.	Index	Q	θ	Ext. Time	Ext. Temp.	Vol.	Length	Area
		$cm^3/sec.$	deg.	sec.	°C	cm^3	cm	cm^2
86.	4	0.512	8	48.6	85	24.9	76.3	225.6
87.	"	"	12	"	80	"	90.1	255.3
88.	"	0.408	"	48.9	"	"	85.9	262.0
89.	"	0.512	"	48.6	"	"	85.6	242.4
90.	"	0.508	"	48.9	90	"	90.3	257.0
91.	"	0.508	"	"	"	"	93.2	241.6
92.	"	0.512	"	48.6	"	"	89.8	251.1
93.	"	"	"	"	70	"	93.0	210.5
94.	"	"	"	"	"	"	83.8	205.3
95.	"	"	"	"	75	"	93.2	216.0
96.	"	"	"	"	"	"	90.8	199.3
97.	"	"	"	"	70	"	80.7	188.5
98.	"	0.508	15	48.9	"	"	90.7	217.9
99.	"	"	"	"	"	"	95.9	211.8
100.	"	"	"	"	"	"	90.9	216.1
101.	"	"	"	"	80	"	106.0	242.9
102.	"	0.609	12	40.8	"	"	90.7	248.9
103.	"	"	"	"	"	"	85.4	238.4
104.	"	"	"	"	"	"	90.3	237.2
105.	"	0.446	"	55.8	"	"	88.1	219.9
106.	"	"	"	"	"	"	83.0	211.5
107.	"	"	"	"	"	"	87.6	218.9
108.	"	0.345	"	72	"	"	86.3	231.3
109.	"	"	"	"	"	"	87.0	228.3
110.	"	"	"	"	"	"	92.5	231.9
111.	"	0.296	"	84	"	"	85.6	190.5
112.	"	"	"	"	"	"	78.2	203.2
113.	"	"	"	"	"	"	74.7	203.5
114.	"	"	5	"	"	"	51.9	190.6

Run No.	Index	Q	θ	Ext. Time	Ext. Temp.	Vol.	Length	Area
		$cm^3/sec.$	deg.	sec.	°C	cm^3	cm	cm^2
115.	4	0.296	5	84	80	24.9	46.8	191.8
116.	"	0.345	"	72	"	"	50.2	209.8
117.	"	"	"	"	"	"	50.1	196.1
118.	"	"	"	"	"	"	51.4	204.4
119.	"	0.609	"	40.8	"	"	47.4	205.9
120.	"	"	"	"	"	"	48.2	216.4
121.	"	"	"	"	"	"	47.4	210.2
122.	"	0.446	"	55.8	"	"	51.1	195.7
123.	"	"	"	"	"	"	46.2	200.7
124.	"	"	"	"	"	"	47.3	206.2
125.	-	-	-	-	-	-	-	-
126.	1	0.300	5	82.8	80	24.9	68.5	288.5
127.	"	"	"	"	"	"	70.5	279.2
128.	"	0.345	"	72	"	"	68.4	298.0
129.	"	0.377	"	66	"	"	70.7	281.6
130.	"	"	"	"	"	"	73.7	273.5
131.	"	0.487	"	51	"	"	84.5	304.7
132.	"	"	"	"	"	"	80.2	282.6
133.	"	0.609	"	40.8	"	"	84.1	306.3
134.	"	"	"	"	"	"	78.8	314.2
135.	"	"	"	"	"	"	83.8	304.3
136.	"	0.418	8	48.0	55	"	88.1	300.2
137.	"	0.412	"	48.6	"	"	88.0	278.9
138.	"	"	"	"	"	"	83.6	268.3
139.	"	"	"	"	65	"	108.1	321.5
140.	"	"	5	"	"	"	79.5	303.4
141.	"	"	"	"	"	"	71.2	296.6
142.	"	"	"	"	"	"	71.5	281.3
143.	"	"	"	"	75	"	76.4	298.5

Run No.	Index	Q	θ	Ext. Time	Ext. Temp.	Vol.	Length	Area
		$cm^3/sec.$	deg.	sec.	°C	cm^3	cm	cm^2
144.	1	0.512	5	48.6	75	24.9	75.4	291.6
145.	"	"	"	"	"	"	79.1	298.3
146.	"	"	"	"	85	"	80.4	312.2
147.	"	"	"	"	"	"	84.6	321.3
148.	"	"	"	"	"	"	85.3	313.0
149.	"	"	3	"	55	"	48.4	292.6
150.	"	"	"	"	"	"	47.2	281.6
151.	"	"	"	"	"	"	44.4	291.5
152.	"	"	"	"	65	"	51.1	292.3
153.	"	"	"	"	"	"	47.2	297.0
154.	"	"	"	"	"	"	47.3	304.6
155.	"	"	"	"	75	"	48.5	302.3
156.	"	"	"	"	"	"	52.7	297.3
157.	"	"	"	"	"	"	48.6	295.9
158.	"	"	"	"	85	"	52.0	294.9
159.	"	"	"	"	"	"	54.3	304.9
160.	"	"	"	"	"	"	60.1	293.5
161.	"	"	5	"	55	"	65.1	282.7
162.	"	"	"	"	"	"	59.2	248.9
163.	"	"	"	"	"	"	59.1	276.2

B. Raw Data for C-4000 (dyed) Flows on Heated Plate

Run No.	Q	Temp.	θ	Vol.	A_e	A_f	Length	Plate Temp.
	$cm^3/sec.$	°C	deg.	cm^3	cm^2	cm^2	cm	°C
4.	1.2	56	2.5	72.0	135.0	315.0	34	46
5.	"	"	2.0	"	172.0	216.0	44	50
6.	"	62	3.5	"	145.0	357.0	71.8	47
7.	1.98	80	"	79.2	269.5	784.3	134	48
8.	1.50	78	4.5	60.0	165.2	475.9	81	48
9.	1.77	88	6.0	62.0	156.1	344.2	85	41
10.	3.75	90	4.0	93.8	327.3	872.8	106	45
11.	2.40	88	2.0	108.0	498.0	1451.0	117	47
12.	1.60	87	5.0	51.2	241.3	506.2	82	41
13.	1.15	81	5.0	51.6	317.0	616.9	98	44
14.	"	85	7.0	34.5	269.1	527.8	-	38
15.	"	89	2.0	115.0	523.2	878.7	59	40

C. Raw Data for Kaolin Suspension Flows

Run No.	Vol.	Ext. Time	θ	A_e	A_f	L_f	ρ	μ	τ_y
	cm^3	sec.	deg.	cm^2	cm^2	cm	g/cm^3	$\frac{dyne\text{-}sec.}{cm^2}$	$\frac{dyne}{cm^2}$
K-6	24.3	54	12	-	282.0	95.0	1.68	2.58	20.00
K-7	"	"	8	-	180.9	48.5	"	"	"
K-8	"	"	"	-	197.2	49.4	"	"	"
K-9	"	"	5	-	155.1	29.0	"	"	"
K-10	"	36	8	-	218.0	60.8	"	"	"
K-11	"	"	5	-	131.5	22.5	"	3.79	15.60
K-12	"	"	8	-	194.0	49.5	"	"	"
K-13	"	"	12	-	264.7	103.2	"	3.87	"
K-14	"	"	10	-	-	87.0	"	-	-
K-15	-	-	-	-	-	-	-	-	-
K-16	24.3	42	8	-	66.5	10.0	1.72	9.26	74.10
K-17	"	"	20	-	146.0	49.8	"	"	"
K-18	"	"	10	-	-	-	-	-	-
K-19	"	"	15	-	115.5	29.8	1.72	9.03	53.60
K-20	-	-	-	-	-	-	-	-	-
K-21	24.3	40.2	15	123.0	247.4	92.4	1.663	7.18	21.82
K-22	"	"	12	122.0	201.6	59.4	"	6.32	20.36
K-23	"	"	10	110.7	184.6	51.3	"	6.45	18.24

Run No.	Vol.	Ext. Time	θ	A_e	A_f	L_f	ρ	μ	τ_y
	cm^3	sec.	deg.	cm^2	cm^2	cm	g/cm^3	$\frac{dyne-sec}{cm^2}$	$\frac{dyne}{cm^2}$
K-24	24.3	40.2	13.5	98.2	208.7	89.1	1.663	5.98	17.29
K-25-1	"	42	16	116.92	215.6	92.3	1.634	6.29	29.53
K-25-2	"	"	"	119.3	215.6	87	"	"	"
K-26-1	"	"	14	123.3	222.3	84	1.644	5.26	21.59
K-26-2	"	"	"	114.8	217.1	81.2	"	"	"
K-27-1	"	"	12	124.2	247.7	103.5	"	5.39	13.95
K-27-2	"	"	"	126.1	246.3	100.5	"	"	"
K-28-1	"	"	10	125.1	234.1	79.3	"	4.63	14.18
K-28-2	"	"	"	135.8	217.7	72.0	"	"	"
K-29-1	"	"	8	106.0	178.2	46.5	"	4.98	12.73
K-29-2	"	"	"	112.3	190.1	48.8	"	"	"
K-30	"	"	16	92.7	118.4	27.2	1.566	7.68	63.94
K-31	"	"	12	84.3	97.7	20.7	"	6.25	61.24
K-32	"	"	20	100.0	161.6	74.8	"	"	"
K-33	"	41	14	100.1	131.6	36.5	"	6.48	44.82
K-34	"	"	12	93.0	125.8	32.6	"	5.23	45.85
K-35	"	"	10	80.3	94.6	19.9	"	"	"
K-36	"	"	16	101.8	152.8	55.3	"	"	"

D. Raw Data for Carbowax Channel Flows

Run No.	Index	Vol.	Ext. Time	L_e	L_f	Width	Ext. Temp	θ
		cm^3	sec.	cm	cm	cm	°C	deg.
C-C1W	4	24.3	45.0	29.0	71.0	2.0	82	3.5
C-C2W	"	"	"	44.0	103.5	1.0	76	3.0
C-C3P	"	"	"	36.0	74.5	1.5	"	3.5
C-C4P	"	"	"	47.0	100.3	1.0	77	4.7
C-C5W	"	"	42.9	28.0	67.0	2.0	75	3.0
C-C6W	"	"	"	37.0	94.5	1.0	77	3.0
C-C7P	"	"	"	32.0	66.5	1.5	80	"
C-C8P	"	"	"	36.0	80.0	1.0	78	"
C-C9P	1	"	"	42.0	90.5	1.5	62	"
C-C10P	"	"	"	51.0	101.2	1.0	70	2.5
C-C11W	"	"	"	54.0	112.5	1.0	65	2.5
C-C12W	"	"	"	36.0	71.0	2.0	60	3.0
C-C13P	4	"	41.0	36.0	76.0	0.85	72	3.5

E. Raw Data for Kaolin Suspension Channel Flows

Run No.	Vol.	Ext. Time	L_e	L_f	Width	θ	ρ	μ	τ_y
	cm^3	sec.	cm	cm	cm	deg.	g/cm^3	$\frac{dyne\text{-}sec}{cm^2}$	$\frac{dyne}{cm^2}$
C-K1W	24.3	42.9	23.0	26.2	2.0	12	1.72	12.67	81.88
C-K2W	"	"	22.5	-	1.0	"	"	"	"
C-K3P	"	"	38.0	57.5	1.5	20	"	"	"
C-K4P	"	"	40.0	57.3	1.0	"	"	"	"
C-K5P	"	41.0	27.0	36.0	1.5	5	1.56	4.22	37.51
C-K6W	"	"	26.0	31.0	1.0	4	"	"	"
C-K7W	"	"	26.0	32.8	2.0	5	"	"	"
C-K8P	"	"	64.0	106.2	1.0	12	"	"	"
C-K9P	"	"	36.0	55.0	0.8	8	"	"	"